UNIVERSITY OF CALIFORNIA
RIVERSIDE

Using a Near-Explicit Model, GECKO-A, to Improve the Mechanistic Understanding of Monoterpene Chemistry as Relevant to Secondary Organic Aerosol (SOA) Formation

A Dissertation submitted in partial satisfaction
of the requirements for the degree of

Doctor of Philosophy

in

Chemical and Environmental Engineering

by

Isaac Kwadjo Afreh

December 2020

Dissertation Committee:
Dr. Kelley C. Barsanti, Chairperson
Dr. David R. Cocker III
Dr. Jingsong Zhang

The Dissertation of Isaac Kwadjo Afreh is approved:

_____

_____

_____

Committee Chairperson

University of California, Riverside

Acknowledgements

Several people have impacted my graduate school journey, and I have to acknowledging their contributions that have brought me to this point successfully.

First, I would like to thank my advisor, Dr. Kelley Barsanti. There are not enough words to express my gratitude for the guidance, mentorship, leadership, and patience these past five years. Dr. Barsanti has not only influenced my ability to communicate, but also given me so many opportunities that have made direct positive impacts on my life. My ability to think critically has improved greatly under her exemplary guidance. I will always be grateful!

I would like to thank my collaborators, Dr. Bernard Aumont, Dr. Marie Camredon, and Dr. Richard Valorso, for teaching me how to use GECKO-A, and for their support, reviews, and input that helped shape my research and helped develop my analytical skills. Also, special thanks to Dr. William Carter for his support and for allowing me to assist with updating the rates constants of organic compounds in SAPRC-18 chemical mechanism.

I would also like to thank my dissertation committee members, Dr. David Cocker and Dr. Jingsong Zhang for their time and helpful feedback.

I am thankful to my research group colleagues, Dr. Paul Van Rooy, Christos Stamatis, Jia Jang, Guadalupe Lara, Afsara Tasnia, and Samiha Binte Shahid, for being wonderful colleagues and friends! It was fun working in close quarters with them. Thank you to Dr. Lindsay Hatch, Dr. Avi Lav, Dr. Xinze Peng, Dr. Emmanuel Fofie, William

Lichtenberg, and Chen Le for their assistance and advice. My sincere gratitude to Qi Li and Jia Jiang for their collaboration on the camphene chamber studies.

Special thanks also go to my funding sources, Esther F. Hays Graduate Fellowship Award, the National Oceanic and Atmospheric Administration (NOAA) grant AC4 NA16OAR4310103 and the National Science Foundation grant AGS-1753364 for providing the funds needed for my research including international travel.

Lastly, I would like to thank my friends and my family, particularly my wife, Kate, my son, Michael, my parents, Emmanuel and Ernestina Afreh, and my uncle, Ransford Boateng, for all their support, sacrifices, and encouragement throughout my education. In conclusion, I would like to thank my Heavenly Father and my Church family – I would not be at this point in my life without them.

Chapter 2 of this dissertation, in full, is a reprint of the material as has been submitted to Atmospheric Chemistry and Physics (ACP) with contributing authors: Bernard Aumont, Marie Camredon, and Kelley Barsanti entitled "Using GECKO-A to derive mechanistic understanding of SOA formation from the ubiquitous but understudied camphene," Atmos. Chem. Phys. Discuss., https://doi.org/10.5194/acp-2020-829, in review, 2020.

ABSTRACT OF THE DISSERTATION

Using a Near-Explicit Model, GECKO-A, to Improve the Mechanistic Understanding of Monoterpene Chemistry as Relevant to Secondary Organic Aerosol (SOA) Formation

by

Isaac Kwadjo Afreh

Doctor of Philosophy, Graduate Program in Chemical and Environmental Engineering
University of California, Riverside, December 2020
Dr. Kelley C. Barsanti, Chairperson

Monoterpenes, which are emitted from biogenic and pyrogenic sources, represent a significant mass fraction of volatile organic compounds (VOCs) emitted to the earth's atmosphere. Monoterpenes exhibit wide diversity in molecular structure and ranges of atmospheric lifetimes, and can impact climate and air quality through the formation of secondary organic aerosol (SOA). To accurately predict the effects of SOA on climate and air quality, better representation of monoterpene chemistry in chemical mechanisms and improved SOA parameterizations are needed. For air quality modeling, the gas-phase chemistry of and SOA formation from monoterpenes are often represented by one or two model surrogates, despite the complexity in monoterpene chemistry and SOA formation potential. While the simplified approach for representing monoterpenes in models enhances computational efficiency, it results in uncertainties in model predictions.

As presented in this thesis, detailed studies of gas-phase chemistry and SOA formation from monoterpenes were performed using a near-explicit chemical mechanism

and box model, GECKO-A. This includes the first mechanistic study of SOA formation from camphene, a ubiquitous but understudied monoterpene. The mechanistic study of SOA formation prompted a chamber study of this interesting compound, and comparison between the model predictions and measurement data were performed. Finally, using GECKO-A and published chamber data, gas-phase chemistry and SOA formation from 13 monoterpenes was studied in an effort to suggest a simplified modeling strategy that better represented the complexity of monoterpene chemistry in air quality models.

The mechanistic study demonstrated that: (1) in the early stages of oxidation, camphene formed very low volatility products, lower than commonly studied monoterpenes α-pinene and limonene; and (2) the final simulated SOA yield for camphene (46 %) was relatively high, approximately twice that of α-pinene (25 %). The model-measurement comparison for camphene supported that camphene forms significant SOA. The SOA yield trends were similar between the model simulations and the chamber studies when nitrogenic oxides were present. The systematic study of the 13 monoterpenes indicated that monocyclic monoterpenes with internal double bonds generally formed more SOA than bicyclic monoterpenes with the exception of camphene. Cluster analysis (k-means) was explored to optimize the number of monoterpene surrogates.

Table of Contents

Chapter 1: Introduction 1
1.1 Introduction 1
References 7
Chapter 2: Using GECKO-A to derive mechanistic understanding of SOA formation from the ubiquitous but understudied camphene 11
1 Introduction 11
2.1 Method 15
2.1.1 GECKO-A Model description 15
2.2 GECKO-A generated oxidation mechanisms 17
2.2.1 OH reaction scheme 17
2.2.2 O_3 reaction scheme 20
2.2.3 NO_3 reaction scheme 21
2.3 Simulation conditions 21
2.3 Results 24
2.3.1 Chamber reactivity simulations 24
2.3.2 Controlled reactivity simulations 34
2.4 Conclusions 44
References 46
Appendix A 56
Chapter 3: Model-Measurement Comparison of Secondary Organic Aerosol Formation from the Photooxidation of Camphene 80
3.1 Introduction 80
3.2 Method 82
3.2.1 Chamber studies and results 82
3.2.2 Model description and simulation conditions 83
3.3 Results and discussion 85
3.3.1 Model-measurement SOA yield comparison 85
3.3.2 Gas-phase reactivity comparison 86
3.3.3 Simulated carbon budget 88
3.3.4 Particle-phase product distribution 91
3.4 Conclusions 95

References 96
Appendix B 99
Chapter 4: Developing air quality model surrogates for monoterpenes using GECKO-A 100
4.1 Introduction 100
4.2 Method 102
4.2.1 GECKO-A model description 102
4.2.2 Simulation conditions 103
4.3 Results 104
4.3.1 Comparison between model results and chamber data 104
4.3.2 Comparison among GECKO-A simulation runs 108
4.3.3 Considering monoterpene representation in models 115
4.4 Conclusions 120
References 121
Appendix C 124
Chapter 5: Conclusion & Future Work 130

List of Tables

Table 2.1: Initial conditions for α-pinene and limonene chamber reactivity simulations. 23

Table 2.2: Initial conditions for camphene, α-pinene, and limonene controlled reactivity simulations. The levels of O_3 and NO_x were fixed during these simulations. 23

Table 2.3: Calculated average mass-weighted O/C ratio and OH exposure at the end of the α-pinene and limonene photooxidation and ozonolysis simulations. 27

Table 2.4: SOA yield and mass predicted using 2-product and VBS parameters for top five monoterpenes by emission factor (EF) from black spruce, Douglas fir, and lodgepole pine. 43

Table A1: SOA data compiled from published chamber studies for photooxidation and ozonolysis of α-pinene and limonene. 56

Table A2: Normalized emission factor (EF) for model surrogates representing top five monoterpenes (by EF) from black spruce, Douglas fir, and lodgepole pine (Hatch et al., 2015, 2017). In Assignment 1, α-pinene is used to represent all monoterpenes except limonene. In Assignment 2, camphene is represented as 50 % α-pinene and 50 % limonene. EFs of assignments 1 and 2 for lodgepole pine are the same, because camphene is not one of the top five monoterpenes by EF. 61

Table A3: Two-product SOA yield parameters for α-pinene and limonene based on Griffin et al. (1999).....61

Table A4: Volatility basis set (VBS) parameters (low NO_x, dry) based on Pathak et al. (2007b) (for α-pinene) and Zhang et al. (2006) (for limonene). 61

Table 3. 1: Initial conditions and chamber SOA data for camphene photooxidation experiments. 83

Table 3.2: Initial conditions of GECKO-A simulations. 84

Table 4.1: Initial conditions for GECKO-A chamber reactivity simulations. 104

Table 4.2: Monoterpenes categorized into groups based on molecular structure, reactivity of precursor with oxidants, SOA yield, and mass of LVOCs using photooxidation simulation results. 119

Table 4.3: Summary of proposed monoterpene groups. 119

Table C1: Initial conditions for GECKO-A controlled reactivity simulations. 124

Table C2: Initial conditions and SOA results from this work compared with photooxidation chamber data from Lee et al. (2006) and Griffin et al. (1999). 124

Table C3: Monoterpenes categorized into 6 groups based on the k-means clustering method for controlled reactivity simulations under relatively low NOx condition (10 ppb NO). 125

Table C4: Monoterpenes categorized into 6 groups based on the k-means clustering method for controlled reactivity simulations under relatively high NOx condition (50 ppb NO). 126

List of Figures

Figure 2.1: Initial oxidation pathways of α-pinene oxidation with OH as represented in GECKO-A. 19

Figure 2.2: Initial oxidation pathways of limonene oxidation with OH as represented in GECKO-A. 19

Figure 2.3: Initial oxidation pathways of camphene oxidation with OH as represented in GECKO-A. 20

Figure 2.4: GECKO-A SOA yields are represented by blue (α-pinene) and red (limonene) markers; chamber SOA yields are represented by grey markers. The initial hydrocarbon mixing ratios are differentiated by shape; squares represent the simulation using the lower hydrocarbon (LHC) mixing ratio and diamonds the simulation using the higher hydrocarbon (HHC) mixing ratio. 27

Figure 2.5: Simulated top 10 gas and top 10 particle-phases products from α-pinene photooxidation (P_LHC). 30

Figure 2.6: Top 10 gas phase and top 10 particle-phase products from α-pinene dark ozonolysis (DO_LHC) simulations. 31

Figure 2.7: Simulated SOA yield (a and b) and carbon budget (c to f) as a function of time for α-pinene and limonene during photooxidation (a, c, e) and dark ozonolysis (b, d, f). The SOA yield curve for α-pinene is represented by a blue line; limonene is represented by a red line. For the carbon budget plots, the mixing ratios of the precursor (black line), particle-phase organics (magenta line), gas-phase organics (green line), and $CO+CO_2$ (blue line) are expressed as carbon atom ratios (ppbC/initial precursor in ppbC). The results shown are for the low hydrocarbon mixing ratio (50 ppb) simulations. 34

Figure 2.8: Mixing ratios of HO_2, OH, and NO_3 as function of time for limonene (red line), camphene (black line), and α-pinene (blue line) during the controlled reactivity simulations with 0.1 ppb of HC_o and 10 μg m^{-3} of organic seed. By design, the profiles of the mixing ratios for each precursor overlap except for at the very beginning of the NO_3 profile. 35

Figure 2.9: (a) Simulated SOA mass as a function of atmospheric aging time (reaction with OH) and (b) simulated SOA yield as a function of reacted hydrocarbon concentration (ΔHC) during controlled reactivity simulation at 0.1 ppb HC_o with 10 μg m^{-3} seed for limonene (red line), camphene (black line), and α-pinene (blue line). 37

Figure 2.10: Number of functional groups associated with gas- and particle-phase species as a function of carbon number. Results are shown for camphene, α-pinene, and limonene

after 72 hours of oxidation under controlled reactivity condition. The markers are sized by the ratio of their mixing ratio (in ppbC) to the initial mixing ratio of the precursor (in ppbC). The colors of the markers are scaled by volatility (represented by saturation concentration, C*). 39

Figure 2.11: Mass percentage of four volatility categories in the particle phase at the end of the controlled reactivity simulations for α-pinene, camphene, and limonene. 41

Figure 2. 12: (a) Simulated SOA yield as a function of atmospheric aging time for camphene (black line), 50 % α-pinene + 50 % limonene (magenta line), and 50 % α-pinene + 50 % limonene where the rate constants of α-pinene and limonene were replaced with the rate constants of camphene (green line); and (b) mass percentage of four volatility categories in the particle phase at the end of the controlled reactivity simulations for camphene, 50 % α-pinene + 50 % limonene, and limonene, and 50 % α-pinene + 50 % limonene where the rate constants of α-pinene and limonene were replaced with the rate constants of camphene.....44

Figure A1: Initial oxidation pathways of α-pinene with O_3 as represented in GECKO-A. 62

Figure A2: Initial oxidation pathways of limonene with O_3 as represented in GECKO-A. 62

Figure A3: Initial oxidation pathways of camphene with O_3 as represented in GECKO-A. 63

Figure A4: Initial oxidation pathways of α-pinene with NO_3 as represented in GECKO-A. 63

Figure A5: Initial oxidation pathways of limonene with NO_3 as represented in GECKO-A. 64

Figure A6: Initial oxidation pathways of camphene with NO_3 as represented in GECKO-A. 64

Figure A7: Percentage of precursor consumed by OH (black), O_3 (red), and NO_3 (blue) as a function of fraction of precursor reacted for α-pinene and limonene under photooxidation and ozonolysis (for lower initial precursor mixing ratio of 50 ppb). 65

Figure A8: The mixing ratios of HO_2, OH, O_3, NO, NO_2, and NO_3 as a function of time for α-pinene (blue line) and limonene (red line) (with the low initial hydrocarbon (LHC) mixing ratio of 50 ppb) during photooxidation (P) and dark ozonolysis (DO) simulations. 66

Figure A9: Number of functional groups associated with gas- and particle-phase species as a function of carbon number. Results are shown for camphene, α-pinene, and limonene after 12 hours of oxidation under photooxidation (P) and dark ozonolysis (DO) with lower hydrocarbon (LHC) mixing ratio of 50 ppb. The markers are sized by the ratio of their mixing ratio (in ppbC) to the initial mixing ratio of the precursor (in ppbC). The colors of the markers are scaled by volatility (represented by saturation concentration, C*). 67

Figure A10: Top 10 gas-phase products from limonene photooxidation low hydrocarbon (P_LHC) simulation. 68

Figure A11: Top 10 particle-phase products from limonene photooxidation low hydrocarbon (P_LHC) simulation. 68

Figure A12: Top 10 gas-phase products from limonene dark ozonolysis low hydrocarbon (DO_LHC) simulation. 69

Figure A13: Top 10 particle-phase products from limonene dark ozonolysis low hydrocarbon (DO_LHC) simulation.....69

Figure A14: Simulated SOA yield as a function of time (a and b) and carbon budget (c to f) for α-pinene and limonene during photooxidation (a, c, e) and dark ozonolysis (b, d, f). The SOA yield curve for α-pinene is represented by a blue line; limonene is represented by a red line. For the carbon budget plots, the mixing ratios of the precursor (black line), particle-phase organics (magenta line), gas-phase organics (green line), and $CO+CO_2$ (blue line) are expressed as carbon atom ratios (in ppbC)/initial precursor (in ppbC). The results shown are for the high hydrocarbon mixing ratio (150 ppb) simulations. 70

Figure A15: Percentage of precursor consumed by OH (black), O_3 (red), and NO_3 (blue) as a function of fraction of precursor reacted for α-pinene and limonene under photooxidation and ozonolysis (for higher initial precursor concentration of 150 ppb). ..71

Figure A16: Mixing ratios of HO_2, OH, O_3, NO, NO_2, and NO_3 as function of time for limonene (red line), camphene (black line), and α-pinene (blue line) during the photooxidation and ozonolysis (with higher initial hydrocarbon mixing ratio of 150 ppb). 72

Figure A17: Number of functional groups associated with gas- and particle-phase species as a function of carbon number. Results are shown for camphene, α-pinene, and limonene after 12 hours of oxidation under photooxidation (P) and dark ozonolysis (DO) with higher hydrocarbon (LHC) mixing ratio of 150 ppb. The markers are sized by the ratio of theirmixing ratio (in ppbC) to the initial mixing ratio of the precursor (in ppbC). The colors of the markers are scaled by volatility (represented by saturation concentration, C*). 73

Figure A18: Top 10 gas-phase products from α-pinene photooxidation high hydrocarbon (P_HHC) simulations.....74

Figure A19: Top 10 particle-phase products from α-pinene photooxidation high hydrocarbon (P_HHC) simulations. 74

Figure A20: Top 10 gas-phase products from α-pinene dark ozonolysis high hydrocarbon (DO_HHC) simulations. 75

Figure A21: Top 10 particle-phase products from α-pinene dark ozonolysis high hydrocarbon (DO_HHC) simulations.....75

Figure A22: Top 10 gas-phase products from limonene photooxidation high hydrocarbon (P_HHC). 76

Figure A23: Top 10 particle-phase products from limonene photooxidation high hydrocarbon (P_HHC).....76

Figure A24: Top 10 gas-phase products from limonene dark ozonolysis high hydrocarbon (DO_HHC).....77

Figure A25: Top 10 particle-phase products from limonene dark ozonolysis high hydrocarbon (DO_HHC). 77

Figure A26: Percentage of precursor reacted by OH (black), O_3 (red), and NO_3 (blue) as a function of fraction of precursor reacted for α-pinene, camphene, and limonene during controlled reactivity (CR) simulations.....78

Figure A27: Top 10 gas-phase products from camphene controlled reactivity simulation. 78

Figure A28: Top 10 particle-phase products from camphene controlled reactivity simulation.....79

Figure A29: (a) Simulated SOA yield as a function of atmospheric aging time for camphene (black line), 50 % α-pinene + 50 % limonene (magenta line), α-pinene with camphene rate constants (blue line), limonene with camphene rate constants (red line), and 50 % α-pinene + 50 % limonene where the rate constants of α-pinene and limonene were replaced with the rate constants of camphene (green line); and (b) mass percentage of four volatility categories in the particle phase at the end of the controlled reactivity simulations for camphene, 50 % α-pinene + 50 % limonene, α-pinene with camphene rate constants, limonene with camphene rate constants, and 50 % α-pinene + 50 % limonene where the rate constants of α-pinene and limonene were replaced with the rate constants of camphene. 79

Figure 3.1: SOA yields of camphene as a function of SOA mass derived from environmental chamber experimental results (a) and GECKO-A simulations results (b).86

Figure 3. 2: model-chamber comparison of mixing ratios of camphene, O_3, and OH as function of time for camphene oxidation with NOx and without NOx.....88

Figure 3.3: Carbon budget as a function of time for camphene photooxidation simulations with NOx.....90

Figure 3.4: Carbon budget as a function of time for camphene photooxidation simulations without NOx.....90

Figure 3.5: Number of functional groups associated with gas- and particle-phase species as a function of carbon number for simulations with NOx. Results are shown for camphene after 8 hours of photooxidation. The markers are sized by the ratio of their mixing ratio (in ppbC) to the initial mixing ratio of the precursor (in ppbC). The colors of the markers are scaled by volatility (represented by saturation concentration, C*).....92

Figure 3.6: Number of functional groups associated with gas- and particle-phase species as a function of carbon number for simulations without NOx. Results are shown for camphene after 8 hours of photooxidation. The markers are sized by the ratio of their mixing ratio (in ppbC) to the initial mixing ratio of the precursor (in ppbC). The colors of the markers are scaled by volatility (represented by saturation concentration, C*).....93

Figure 3.7: Top 5 particle-phase products from 10 ppb camphene photooxidation simulation with NOx. 93

Figure 3.8: Top 5 particle-phase products from 150 ppb camphene photooxidation simulation with NOx. 94

Figure 3.9: Top 5 particle-phase products from 10 ppb camphene photooxidation simulation without NOx.....94

Figure 3.10: Top 5 particle-phase products from 150 ppb camphene photooxidation simulation without NOx.....94

Figure B1: Percentage of precursor consumed by OH (black), O_3 (red), and NO_3 (blue) as a function of fraction of precursor reacted for camphene in the presence of initial NOx.99

Figure B2: Percentage of precursor consumed by OH (black), O3 (red), and NO3 (blue) as a function of fraction of precursor reacted for camphene without NOx. 99

Figure 4.1: Comparison of GECKO-A SOA yields with chamber SOA yields. GECKO-A SOA yields (diamonds), chamber SOA yields from Lee et al. (2006) are represented by circles, and Griffin et al SOA yields are represented by squares. 106

Figure 4.2: Number of functional groups associated with gas- and particle-phase species as a function of carbon number for limonene, α-terpinene, β-myrcene, terpinolene, β-pinene, α-pinene, and 3-carene after 8 hours of photooxidation simulation.....110

Figure 4.3: Number of functional groups associated with gas- and particle-phase species as a function of carbon number for camphene, β-phellandrene, α-phellandrene, γ-terpinene, α-pinene, z-ocimene, and 3-carene after 8 hours of photooxidation simulation. 111

Figure 4.4: Simulated SOA yield as a function of time for 13 monoterpenes. Inserted in the legend are the respective SOA yield values for the monoterpenes. 112

Figure 4.5: Simulated SOA yield as a function of time for compounds in each monoterpene group. Inserted in the legend are the respective SOA yield values for the monoterpenes. 118

Figure C1: Percentage of precursor consumed by OH (black), O3 (red), and NO3 (blue) as a function of fraction of precursor reacted for limonene, camphene, β-phellandrene, α-phellandrene, α-terpinene, γ-terpinene, β-myrcene, terpinolene, β-pinene, α-pinene, z-ocimene, sabinene, and 3-carene. 127

Figure C2: Carbon budget as a function of time during photooxidation simulation for limonene, camphene, β- phellandrene, α-phellandrene, α-terpinene, γ-terpinene, β-myrcene, terpinolene, β-pinene, α-pinene, z-ocimene, sabinene, and 3-carene.....128

Figure C3: Structures of the monoterpenes studied (Atkinson and Arey, 2003). 129

Figure C4: Mass percentage of four volatility categories in the particle phase at the end of the photooxidation simulation. 129

Chapter 1: Introduction

1.1 Introduction

Global emissions of biogenic volatile organic compounds (BVOCs) are on the order of 500 Tg carbon yr^{-1} (Guenther et al., 1995). Monoterpenes ($C_{10}H_{16}$) account for approximately one-fifth of the total estimated BVOC emissions (Guenther et al., 1995). Monoterpenes also represent a significant mass fraction of VOCs emitted from pyrogenic sources, particularly from coniferous fuels (e.g., Akagi et al., 2013; Gilman et al., 2015; Hatch et al., 2015). These atmospherically relevant monoterpenes exhibit large diversity in molecular structure and reaction rate constants (Atkinson & Arey, 2003a, 2003b). Once emitted to the atmosphere, monoterpenes can impact climate and air quality through the production of secondary organic aerosol (SOA), which forms a large fraction of atmospheric particulate matter (PM) (e.g., Jimenez et al., 2009; Kanakidou et al., 2004).

PM in the atmosphere is known to have effects on visibility, radiative climate forcing, cloud droplet formation, and public health (Crutzen & Andreae, 1990; Heilman et al., 2014; Jacobson et al., 2000; Kanakidou et al., 2004). PM affects visibility when particles with sizes similar to wavelengths of visible light, absorb and scatter light transmitted through the atmosphere (Jacobson et al., 2000). Furthermore, PM can directly affect climate either by reflecting incoming solar radiation back into space leading to atmospheric cooling or by absorbing solar radiation thereby causing atmospheric warming (Crutzen & Andreae, 1990; Kanakidou et al., 2004; Pöschl, 2005). In addition, PM can indirectly affect climate by influencing cloud formation (Crutzen & Andreae, 1990;

Kanakidou et al., 2004; Pöschl, 2005). Besides climatic effects, PM can also severely impact human health (Bernstein et al., 2004). Based on epidemiology studies, human exposures to PM can increase airway inflammation, initiate asthma, and exacerbate allergies (Bernstein et al., 2004; Pöschl, 2005). Additionally, health studies suggest that long-term exposures to PM can lead to death from lung and heart diseases (Bernstein et al., 2004; Valavanidis et al., 2008).

Formation of secondary PM, or SOA, involves the oxidation of VOCs by atmospheric oxidants - hydroxyl radicals (OH), ozone (O_3) and/or nitrate radicals (NO_3) - to form oxygenated products (Jacobson et al., 2000; Ziemann, 2011). Oxygenated products, which result from addition of functional groups to the VOCs, generally have higher polarity and lower volatility than the parent hydrocarbon, and therefore have a greater propensity to condense into the particle phase (Ziemann, 2011). Hence, the extent of SOA formation is dependent on the reactivity of the hydrocarbon and the volatility of oxidation products formed (Atkinson & Arey, 2003b; Ziemann, 2011). The potential of a hydrocarbon to form SOA can be quantified by its SOA yield, defined as the fraction of particle-phase mass concentration relative to the amount of hydrocarbon reacted (Odum et al., 1996).

To represent SOA formation in chemical transport models, a chemical mechanism is used to represent the reactivity of VOCs and subsequent oxidation product formation. Examples of widely used chemical mechanisms in atmospheric models include SAPRC-07, MOZART-4 (Model for Ozone and Related chemical Tracers, version 4), RACM (Regional Atmospheric Chemistry Mechanism), and CB-05 (Carbon Bond 05) (Carter, 2010b; Edney et al., 2010; Emmons et al., 2010; Stockwell et al., 1997; Yarwood et al.,

2005). To enhance computational efficiency, most gas-phase mechanisms adopt simplification strategies whereby individual VOCs are lumped into surrogate species, largely based similarities in key properties including reactivity with OH and molecular structure (Stockwell et al., 1990). Each lumped or surrogate species in the chemical mechanism then follows a prescribed reaction scheme to form products (Carter, 2010a). The lumping techniques used in the reduced chemical mechanisms are necessary because of the: (1) numerous organic compounds and complex chemical reactions that need to be represented for the atmosphere; and (2) enormous amounts of computer resources required to run the detailed (explicit) reaction mechanisms (Goliff et al., 2012; Stockwell et al., 1990; Zaveri & Peters, 1999).

Chemical mechanisms used in air quality models tend to have improved predictive capability for ozone since ozone was of great importance in tropospheric chemistry at the inception of these models (Horowitz et al., 2003). While such mechanisms are routinely used for modeling SOA, their lumping approaches have not been optimized to best represent the reactivity and properties of VOCs that serve as precursors to SOA. For example, monoterpenes are often represented by one or two model surrogates in gas-phase chemical mechanisms and SOA parameterizations used in chemical transport modeling (Carlton et al., 2010; Carter, 2010b), even though monoterpenes are known to have diverse chemical structures, different reaction rate constants with atmospheric oxidants (by orders of magnitude), and varied propensity for SOA formation (Atkinson & Arey, 2003a; Griffin et al., 1999; Horowitz et al., 2003; Valorso et al., 2011).

SOA parameters used in models are generally derived using a two-product model or volatility-basis set (VBS) approach. The two-product model is based on gas/particle partitioning theory, where two semi-volatile products are assumed to represent the oxidation products of each VOC and can partition to an absorbing organic material phase (Odum et al., 1996; Pankow, 1994). Each product is assigned two parameters: a mass-based stoichiometric yield (α) and an equilibrium absorption coefficient (K_{om}). For the VBS approach, the semi-volatile products are grouped based on the effective saturation concentration (C^*) of the products (Donahue et al., 2006). The C^* values are usually decadally spaced into "bins", and the stoichiometric coefficients (α) (equal to the number of bins) are then derived for each VOC (e.g., Pathak et al., 2007).

This thesis presents research on mechanistic studies of SOA formation from monoterpenes and efforts to optimize the number of monoterpene surrogates for air quality modeling. The Generator of Explicit Chemistry and Kinetics of Organics in the Atmosphere (GECKO-A), an explicit chemical mechanism generator and SOA model, was used to generate nearly-explicit gas-phase mechanisms of monoterpene oxidation and to simulate SOA formation from individual monoterpenes under a varying NOx conditions and precursor concentrations (Aumont et al., 2005; Camredon et al., 2007). Detailed GECKO-A results discussed in this thesis included product formation, carbon budgets, distribution of gas- and particle-phase species in carbon oxidation state – volatility space, and mass-based contributions of compounds to SOA as a function of number of carbons and functional groups. Also presented are comparisons of the model results with chamber data to assess model performance.

The first mechanistic study of SOA formation from camphene is presented in Chapter Two. Camphene was compared with two well-studied monoterpenes, α-pinene and limonene. GECKO-A simulations were run under chamber-relevant conditions to capture trends in simulated SOA yield and to allow comparison with published chamber data. Model simulations were also run under idealized atmospheric conditions to allow a more direct comparison of camphene with α-pinene and limonene. Parameters considered in the comparison included gas-phase oxidation pathways, gas-phase reactivity profiles, time-evolution of SOA mass and yields, and physicochemical property distributions of gas- and particle-phase products.

A model-measurement comparison of camphene SOA formation is presented in Chapter Three. Since the model simulations described in Chapter two suggested very high SOA yields were possible, simulations and chamber experiments were run with similar initial conditions to allow comparison, and that they were guided by the prior results. The simulation results were used to explain SOA trends observed in the chamber data. Further, the effects of initial hydrocarbon concentration and NOx condition on the gas-phase reactivity and the product distribution of camphene SOA were studied.

The mechanistic study of SOA formation from 13 monoterpenes commonly measured in the ambient atmosphere, and approaches for developing accurate but manageable parameterizations for air quality models, are presented in Chapter Four. The ability of GECKO-A to reproduce chamber observations for six of the 13 monoterpenes was evaluated by comparing modeled SOA mass concentrations and yields with measured SOA mass concentrations and yields from two studies that evaluated multiple

monoterpenes (minimizing effects of chamber-chamber variability on the results): Lee et al. (2006) and Griffin et al. (1999). Effects of molecular structure on gas-phase reactivity and SOA formation from monoterpenes were studied. Simplified modeling strategies that better represent the complexity of monoterpene chemistry in air quality models are proposed.

References

Aumont, B., Szopa, S., & Madronich, S. (2005). Modelling the evolution of organic carbon during its gas-phase tropospheric oxidation: development of an explicit model based on a self generating approach. *Atmospheric Chemistry and Physics Discussions*, *5*(1), 703–754. https://doi.org/10.5194/acpd-5-703-2005

Akagi, S. K., Yokelson, R. J., Burling, I. R., Meinardi, S., Simpson, I., Blake, D. R., McMeeking, G. R., Sullivan, A., Lee, T., Kreidenweis, S., Urbanski, S., Reardon, J., Griffith, D. W. T., Johnson, T. J., & Weise, D. R. (2013). Measurements of reactive trace gases and variable O3 formation rates in some South Carolina biomass burning plumes. Atmospheric Chemistry and Physics, 13(3), 1141–1165. https://doi.org/10.5194/acp-13-1141-2013

Atkinson, R., & Arey, J. (2003a). Atmospheric Degradation of Volatile Organic Compounds. Chemical Reviews, 103(12), 4605–4638. https://doi.org/10.1021/cr0206420

Atkinson, R., & Arey, J. (2003b). Gas-phase tropospheric chemistry of biogenic volatile organic compounds: a review. Atmospheric Environment, 37(2), 197–219. https://doi.org/10.1016/S1352-2310(03)00391-1

Bernstein, J. A., Alexis, N., Barnes, C., Bernstein, I. L., Nel, A., Peden, D., Diaz-Sanchez, D., Tarlo, S. M., Williams, P. B., & Bernstein, J. A. (2004). Health effects of air pollution. Journal of Allergy and Clinical Immunology, 114(5), 1116–1123. https://doi.org/10.1016/j.jaci.2004.08.030

Camredon, M., Aumont, B., Lee-Taylor, J., & Madronich, S. (2007). The SOA/VOC/NOx system: An explicit model of secondary organic aerosol formation. *Atmospheric Chemistry and Physics*, *7*(21), 5599–5610. https://doi.org/10.5194/acp-7-5599-2007

Carlton, A. G., Bhave, P. v., Napelenok, S. L., Edney, E. O., Sarwar, G., Pinder, R. W., Pouliot, G. A., & Houyoux, M. (2010). Model Representation of Secondary Organic Aerosol in CMAQv4.7. Environmental Science & Technology, 44(22), 8553–8560. https://doi.org/10.1021/es100636q

Carter, W. P. L. (2010a). Development of a condensed SAPRC-07 chemical mechanism. Atmospheric Environment, 44(40), 5336–5345. https://doi.org/10.1016/j.atmosenv.2010.01.024

Carter, W. P. L. (2010b). Development of the SAPRC-07 chemical mechanism. Atmospheric Environment, 44(40), 5324–5335. https://doi.org/10.1016/j.atmosenv.2010.01.026

Crutzen, P. J., & Andreae, M. (1990). Biomass Burning in the Tropics: Impact on Atmospheric Chemistry and Biogeochemical Cycles Estimates of Worldwide Biomass Burning. Science, 250(4988), 1669–1678. https://doi.org/10.1126/science.250.4988.1669

Donahue, N. M., Robinson, A. L., Stanier, C. O., & Pandis, S. N. (2006). Coupled partitioning, dilution, and chemical aging of semivolatile organics. Environmental Science and Technology, 40(8), 2635–2643. https://doi.org/10.1021/es052297c

Edney, E. O., Sarwar, G., Pinder, R. W., Pouliot, G. A., Houyoux, M., Agency, U. S. E. P., & Carolina, N. (2010). Model Representation of Secondary Organic Aerosol in CMAQv4.7. 44(22), 8553–8560.

Emmons, L. K., Walters, S., Hess, P. G., Lamarque, J., Pfister, G. G., Fillmore, D., & Granier, C. (2010). Development Description and evaluation of the Model for Ozone and Related chemical Tracers, version 4 (MOZART-4). 43–67.

Gilman, J. B., Lerner, B. M., Kuster, W. C., Goldan, P. D., Warneke, C., Veres, P. R., Roberts, J. M., de Gouw, J. A., Burling, I. R., & Yokelson, R. J. (2015). Biomass burning emissions and potential air quality impacts of volatile organic compounds and other trace gases from fuels common in the US. Atmospheric Chemistry and Physics, 15(24), 13915–13938. https://doi.org/10.5194/acp-15-13915-2015

Goliff, W. S., Stockwell, W. R., & Lawson, C. v. (2012). The regional atmospheric chemistry mechanism, version 2. AEA, 68, 174–185. https://doi.org/10.1016/j.atmosenv.2012.11.038

Griffin, R. J., Cocker, D. R., Flagan, R. C., & Seinfeld, J. H. (1999). Organic aerosol formation from the oxidation of biogenic hydrocarbons. Journal of Geophysical Research Atmospheres, 104(D3), 3555–3567. https://doi.org/10.1029/1998JD100049

Guenther, A., Hewitt, C. N., Erickson, D., Fall, R., Geron, C., Graedel, T., Harley, P., Klinger, L., Lerdau, M., Mckay, W. A., Pierce, T., Scholes, B., Steinbrecher, R., Tallamraju, R., Taylor, J., & Zimmerman, P. (1995). A global model of natural volatile organic compound emission. Journal of Geophysical Research, 100(D5), 8873–8892. https://doi.org/10.1029/94JD02950

Hatch, L. E., Luo, W., Pankow, J. F., Yokelson, R. J., Stockwell, C. E., & Barsanti, K. C. (2015). Identification and quantification of gaseous organic compounds emitted from biomass burning using two-dimensional gas chromatography-time-of-flight mass spectrometry. Atmospheric Chemistry and Physics, 15(4), 1865–1899. https://doi.org/10.5194/acp-15-1865-2015

Heilman, W. E., Liu, Y., Urbanski, S., Kovalev, V., & Mickler, R. (2014). Wildland fire emissions, carbon, and climate: Plume rise, atmospheric transport, and chemistry

processes. Forest Ecology and Management, 317, 70–79. https://doi.org/10.1016/j.foreco.2013.02.001

Horowitz, L. W., Walters, S., Mauzerall, D. L., Emmons, L. K., Rasch, P. J., Granier, C., Tie, X., Lamarque, J.-F., Schultz, M. G., Tyndall, G. S., Orlando, J. J., & Brasseur, G. P. (2003). A global simulation of tropospheric ozone and related tracers: Description and evaluation of MOZART, version 2. Journal of Geophysical Research: Atmospheres, 108(D24), n/a-n/a. https://doi.org/10.1029/2002JD002853

Jacobson, M. C., Hansson, H. C., Noone, K. J., & Charlson, R. J. (2000). Organic atmospheric aerosols: Review and state of the science. Reviews of Geophysics, 38(2), 267–294. https://doi.org/10.1029/1998RG000045

Jimenez, J. L., Canagaratna, M. R., Donahue, N. M., Prevot, A. S. H., Zhang, Q., Kroll, J. H., DeCarlo, P. F., Allan, J. D., Coe, H., Ng, N. L., Aiken, A. C., Docherty, K. S., Ulbrich, I. M., Grieshop, A. P., Robinson, A. L., Duplissy, J., Smith, J. D., Wilson, K. R., Lanz, V. A., … Worsnop, D. R. (2009). Evolution of organic aerosols in the atmosphere. Science, 326(5959), 1525–1529. https://doi.org/10.1126/science.1180353

Kanakidou, M., Seinfeld, J. H., Pandis, S. N., Barnes, I., Dentener, F. J., Facchini, M. C., van Dingenen, R., Ervens, B., Nenes, A., Nielsen, C. J., Swietlicki, E., Putaud, J. P., Balkanski, Y., Fuzzi, S., Horth, J., Moortgat, G. K., Winterhalter, R., Myhre, C. E. L., Tsigaridis, K., … Wilson, J. (2004). Organic aerosol and global climate modelling: a review. Atmospheric Chemistry and Physics Discussions, 4(5), 5855–6024. https://doi.org/10.5194/acpd-4-5855-2004

Lee, A., Goldstein, A. H., Kroll, J. H., Ng, N. L., Varutbangkul, V., Flagan, R. C., & Seinfeld, J. H. (2006). Gas-phase products and secondary aerosol yields from the photooxidation of 16 different terpenes. Journal of Geophysical Research Atmospheres, 111, D17305. https://doi.org/10.1029/2006JD007050

Odum Jay, R., Hoffmann, T., Bowman, F., Collins, D., Flagan Richard, C., & Seinfeld John, H. (1996). Gas particle partitioning and secondary organic aerosol yields. Environmental Science and Technology, 30(8), 2580–2585. https://doi.org/10.1021/es950943+

Pankow, J. F. (1994). An absorption model of the gas/aerosol partitioning involved in the formation of secondary organic aerosol. *Atmospheric Environment*, *28*(2), 189–193. https://doi.org/10.1016/1352-2310(94)90094-9

Pathak, R. K., Presto, A. A., Lane, T. E., Stanier, C. O., Donahue, N. M., & Pandis, S. N. (2007). Ozonolysis of α-pinene: Parameterization of secondary organic aerosol mass fraction. Atmospheric Chemistry and Physics, 7(14), 3811–3821. https://doi.org/10.5194/acp-7-3811-2007

Pöschl, U. (2005). Atmospheric Aerosols: Composition, Transformation, Climate and Health Effects. Angewandte Chemie International Edition, 44(46), 7520–7540. https://doi.org/10.1002/anie.200501122

Schwantes, R. H., Emmons, L. K., Orlando, J. J., Barth, M. C., Tyndall, G. S., Hall, S. R., Ullmann, K., St Clair, J. M., Blake, D. R., Wisthaler, A., & Paul Bui, T. v. (2020). Comprehensive isoprene and terpene gas-phase chemistry improves simulated surface ozone in the southeastern US. Atmos. Chem. Phys, 20, 3739–3776. https://doi.org/10.5194/acp-20-3739-2020

Stockwell, W. R., Kirchner, F., Kuhn, M., & Seefeld, S. (1997). A new mechanism for regional atmospheric chemistry modeling. Journal of Geophysical Research Atmospheres, 102(D22), 25847–25879. https://doi.org/10.1029/97jd00849

Stockwell, W. R., Middleton, P., Chang, J. S., & Tang, X. (1990). The second generation regional acid deposition model chemical mechanism for regional air quality modeling. Journal of Geophysical Research, 95(D10), 16343. https://doi.org/10.1029/JD095iD10p16343

Valavanidis, A., Fiotakis, K., & Vlachogianni, T. (2008). Airborne Particulate Matter and Human Health: Toxicological Assessment and Importance of Size and Composition of Particles for Oxidative Damage and Carcinogenic Mechanisms. Journal of Environmental Science and Health, Part C, 26(4), 339–362. https://doi.org/10.1080/10590500802494538

Valorso, R., Aumont, B., Camredon, M., Raventos-Duran, T., Mouchel-Vallon, C., Ng, N. L., Seinfeld, J. H., Lee-Taylor, J., & Madronich, S. (2011). Explicit modelling of SOA formation from α-pinene photooxidation: Sensitivity to vapour pressure estimation. Atmospheric Chemistry and Physics, 11(14), 6895–6910. https://doi.org/10.5194/acp-11-6895-2011

Yarwood, G., Rao, S., Yocke, M., & Whitten, G. Z. (2005). Updates to the carbon bond chemical mechanism: CB05. Final report to the U.S. EPA. http://www.camx.com/publ/pdfs/cb05_final_report_120805.pdf

Zaveri, R. A., & Peters, L. K. (1999). A new lumped structure photochemical mechanism for large-scale applications. Journal of Geophysical Research: Atmospheres, 104(D23), 30387–30415. https://doi.org/10.1029/1999JD900876

Ziemann, P. J. (2011). Effects of molecular structure on the chemistry of aerosol formation from the OH-radical-initiated oxidation of alkanes and alkenes. International Reviews in Physical Chemistry, 30(2), 161–195. https://doi.org/10.1080/0144235X.2010.550728

Chapter 2: Using GECKO-A to derive mechanistic understanding of SOA formation from the ubiquitous but understudied camphene

2.1 Introduction

Sources of atmospheric monoterpene ($C_{10}H_{16}$) emissions are diverse, and include biogenic sources (Geron et al., 2000; Guenther et al., 1995; Hayward et al., 2001; Kesselmeier and Staudt, 1999; Kim et al., 2010; Ludley et al., 2009; Maleknia et al., 2007; Rinne et al., 2000; Steinbrecher et al., 1999; Tani et al., 2003; White et al., 2008), as well as pyrogenic sources (Akagi et al., 2011, 2013; Gilman et al., 2015; Hatch et al., 2015; Simpson et al., 2011). Monoterpenes account for an estimated one-fifth of total global biogenic volatile organic compound (BVOC) emissions (Guenther et al., 1995; Hallquist et al., 1999). Quantities and identities of monoterpenes emitted from biogenic sources primarily depend on plant species and temperature/light (Geron et al., 2000; Hayward et al., 2001; Yáñez-Serrano et al., 2018). Studies across biogenic source types (e.g., terrestrial vegetation, soil, and marine) typically include up to 14 individual monoterpenes, with α-pinene, β-pinene, camphene, 3-carene, limonene, myrcene, p-ocimene, and sabinene being the most widely reported and having the highest emissions (Ambrose et al., 2010; Bäck et al., 2012; Fehsenfeld et al., 1992; Geron et al., 2000; Hayward et al., 2001; Rinne et al., 2000; White et al., 2008; Yassaa et al., 2008). As with biogenic sources, the identities and quantities of monoterpenes from pyrogenic sources (e.g., biomass burning) vary as a function of plant species and fuel component (Hatch et al., 2019). Approximately 30 monoterpene isomers have been observed from biomass burning sources, with α-pinene, β-

pinene, camphene, 3-carene, limonene, and myrcene being commonly detected (Akagi et al., 2013; Gilman et al., 2015; Hatch et al., 2015).

Monoterpenes have a wide range of molecular structures, atmospheric lifetimes, and secondary organic aerosol (SOA) formation potentials. The molecular structures of monoterpenes can be acyclic or cyclic (with variability in the size and number of rings) and can include one to three C=C double bonds (Atkinson and Arey, 2003b; Calogirou et al., 1999; Jacobson et al., 2000; Lee et al., 2006a). The reaction rate constants of monoterpenes with atmospheric oxidants vary by orders of magnitude (Atkinson and Arey, 2003a; Geron et al., 2000); also, their atmospheric lifetimes vary from minutes to days (Atkinson and Arey, 2003b). Monoterpenes can react with atmospheric oxidants to form less-volatile oxidation products leading to the formation of SOA. SOA composes a significant fraction of atmospheric fine particulate matter ($PM_{2.5}$), which adversely affects air quality and impacts climate (Almatarneh et al., 2018; Hallquist et al., 1999; Jacobson et al., 2000; Kanakidou et al., 2004). The extent of SOA formation from monoterpenes can vary significantly, due to differences in their structures, reaction rates, and volatility of their oxidation and accretion products (Griffin et al., 1999; Ng et al., 2007; Zhang et al., 2015).

Over the past two decades, chamber studies have been performed using monoterpene precursors to elucidate their potential to form SOA under conditions approximating atmospheric relevance. For example, Griffin et al. (1999) used a series of outdoor chamber experiments to establish the SOA formation potential of fourteen biogenic compounds, including nine monoterpenes. Since then, several chamber studies

under varying experimental conditions have been conducted for individual monoterpenes including α-pinene, β-pinene, 3-carene, limonene, and myrcene (e.g., Amin et al., 2013; Boyd et al., 2017; Fry et al., 2014; Hatfield and Huff Hartz, 2011; Lee et al., 2006a; Ng et al., 2007; Presto et al., 2005; Presto and Donahue, 2006; Zhao et al., 2018). Additionally, chamber studies have been conducted to investigate gas-phase reaction pathways and major products from the reactions of monoterpenes with hydroxyl radical (OH), ozone (O_3), and nitrate radical (NO_3) (e.g., Draper et al., 2015; Kundu et al., 2012; Zhang et al., 2015). While some monoterpenes have been well studied in chambers or other laboratory reactors, other monoterpenes are relatively under studied, including some that are commonly measured in non-negligible quantities in the atmosphere.

Parameterizations used in air quality models are largely based on laboratory studies, thus widely studied monoterpenes (e.g., α-pinene and limonene) are often used as surrogates to represent the gas-phase chemistry and SOA formation of all terpenes (e.g., Carter, 2010; Saha and Grieshop, 2016; Stockwell et al., 1997). The lack of monoterpene-specific laboratory data can result in inadequate representation of monoterpene chemistry, including SOA formation, particularly where a diversity of unrepresented monoterpenes has a large contribution to total emissions. Camphene is one monoterpene that has been observed in the atmosphere but has little to no published data regarding SOA formation. Previous experimental and theoretical studies of camphene focused on the gas-phase reactions of camphene and product identification (Atkinson et al., 1990; Gaona-Colmán et al., 2017; Hakola et al., 1994). Recently, a density functional theory (DFT) approach was also used to investigate the oxidation of camphene and the fate of product radicals under

atmospherically relevant conditions (Baruah et al., 2018). While this approach identified plausible reaction pathways of camphene photooxidation and associated gas-phase products, formation of SOA was not considered.

In this work, a mechanistic study of SOA formation from camphene was conducted using the Generator for Explicit Chemistry and Kinetics of Organics in the Atmosphere (GECKO-A). GECKO-A has been previously used to study SOA formation from a number of precursors (e.g., Camredon et al., 2007; La et al., 2016; McVay et al., 2016; Valorso et al., 2011). GECKO-A was used here to generate nearly explicit mechanisms for camphene and the well-studied monoterpenes α-pinene and limonene. Model simulations were run under chamber-relevant conditions ("chamber reactivity simulations") to capture trends in simulated SOA mass and composition and compared with published observations using commonly reported metrics including SOA yields and oxygen/carbon (O/C) ratios. Model simulations were also run under idealized atmospheric conditions ("controlled reactivity simulations") to perform a direct comparison of camphene with α-pinene and limonene under tropospheric conditions; including comparisons of gas-phase oxidation pathways, gas-phase reactivity profiles, time-evolution of SOA mass and yields, and physicochemical property distributions of gas- and particle-phase products. The feasibility of using α-pinene or limonene as a surrogate for camphene was assessed. Based on these analyses, implications for air quality model predictions and opportunities for future studies were identified.

2.1 Method

2.1.1 GECKO-A Model description

SOA formation from three monoterpene precursors (α-pinene, limonene, and camphene) was modeled using GECKO-A. A description of GECKO-A is given by Aumont et al. (2005). GECKO-A is a modeling tool that generates nearly explicit gas-phase oxidation mechanisms for individual or multiple organic compounds under general atmospheric conditions (Aumont et al., 2005, 2012; Camredon et al., 2007), as well as the properties to represent the gas/particle mass transfer of the stable organic compounds present in the mechanisms (Camredon et al., 2007; Valorso et al., 2011). The nearly explicit chemical mechanism is generated using experimental data and a predefined protocol (Aumont et al., 2005, 2012; Camredon et al., 2007). The protocol is described in Aumont et al. (2005) and includes updates described in Aumont et al. (2013), La et al. (2016), McVay et al. (2016), and Valorso et al. (2011). In the absence of experimental data, reaction rate constants and products, as well as their physicochemical properties, are estimated based on structure-activity relationships (SARs) (Aumont et al., 2005). The saturation vapor pressures of stable organic compounds were estimated in this work using the Nannoolal method (Nannoolal et al., 2008). Autoxidation, however, is not considered in the current version of GECKO-A.

Some simplifications were applied in this work during the mechanism generation to reduce the size of the gas-phase chemical mechanisms: (1) the maximum generations of oxidation for each mechanism was set at six based on prior GECKO-A modeling results, where increasing the number of generations beyond six for hexadecane oxidation did not

result in significant changes in the evolution of the gas and particle phases (Aumont et al., 2012); (2) species with vapor pressure below 10^{-13} atm (equivalent to saturation concentration, C* of 1.023×10^{-3} μg m^{-3} for a species with molecular weight of 250 g mol^{-1}) were considered non-volatile and remained in the particle phase. (Valorso et al., 2011); (3) position isomers were lumped if the production yield of a species was lower than 10^{-3} (Valorso et al., 2011). The chemical mechanisms generated for this study included: 1.4×10^6 reactions and 2×10^5 oxidation products for α-pinene; 6.5×10^5 reactions and 9.3×10^4 oxidation products for limonene; and 1.3×10^6 reactions and 1.8×10^5 oxidation products for camphene. These mechanisms were then implemented in a box model to simulate the evolution of gaseous organic compounds and SOA formation (Aumont et al., 2005, 2012; Camredon et al., 2007). In the version of GECKO-A used for this work, gas/particle partitioning was calculated according to the saturation vapor pressure of each organic compound and assuming thermodynamic equilibrium between the gas and an ideal (activity coefficients = 1), homogeneous, and inert condensed phase. No condensed-phase reactions were included.

2.2 GECKO-A generated oxidation mechanisms

2.2.1 OH reaction scheme

The reaction pathways of OH-initiated oxidation of α-pinene, limonene, and camphene up to the formation of 1st-generation stable products are shown in Figs. 2.1, 2.2, and 2.3, respectively. The initial reaction steps proceed mainly by the addition of OH to the C=C double bond or by hydrogen abstraction. This leads to the formation of hydroxyalkyl radicals which react rapidly with O_2 to form peroxy radicals. The peroxy radicals can combine with NO, RO_2 or HO_2 to form stable products. The peroxy radicals can also lose an oxygen atom through reaction with NO to form alkoxy radicals, which is consistent with observations reported by Atkinson and Arey (1998) and Calogirou et al. (1999). For α-pinene oxidation, the hydroxyalkyl radicals primarily react with O_2 to form peroxy radicals, which then react with NO, RO_2 or HO_2 to form predominantly four-membered ring stable products or lose an oxygen atom to form alkoxy radicals. As observed by Lee et al. (2006b), the alkoxy radicals undergo subsequent reactions leading to formation of formaldehyde, acetone, and multifunctional products including pinonaldehyde. For limonene oxidation, reaction of the peroxy radicals with $NO/NO_3/RO_2$ followed by O_2 addition and NO to NO_2 conversion leads to the formation of limononaldehyde or limonaketone and formaldehyde, which are consistent with observations reported by Lee et al. (2006b). Alternatively, the peroxy radicals react with $NO/NO_3/RO_2$ to form ring-opened peroxy radicals, which further react to form multifunctional products. For camphene, the hydroxyalkyl radicals react rapidly with O_2 to form hydroxyalkylperoxy radicals. The hydroxyalkylperoxy radicals subsequently react

with NO, RO_2, and HO_2 to form stable products, or react with $NO/NO_3/RO_2$ to form hydroxyalkoxy radicals. The hydroxyalkoxy radicals then either decompose to form camphenilone (a bicyclic product) and formaldehyde, or react with O_2 to form five-membered ring hydroxyperoxy radicals, which further react to form multifunctional products. The reaction pathway of OH addition to the exocyclic double bond of camphene as represented in GECKO-A is in agreement with the observations made by Gaona-Colmán et al. (2017) and Reissell et al. (1999), as well as by Baruah et al. (2018) in their DFT study of OH-initiated oxidation of camphene. While camphene and α-pinene are structurally bicyclic, their 1st generation products resulting from the decomposition of the bicyclic hydroxyalkoxy radicals differ; camphene primarily forms five-membered ring 1st generation products while α-pinene primarily forms four-membered ring 1st generation products. Limonene, which is monocyclic, primarily forms ring-opened 1st generation products when its monocyclic hydroxyalkoxy radicals decompose.

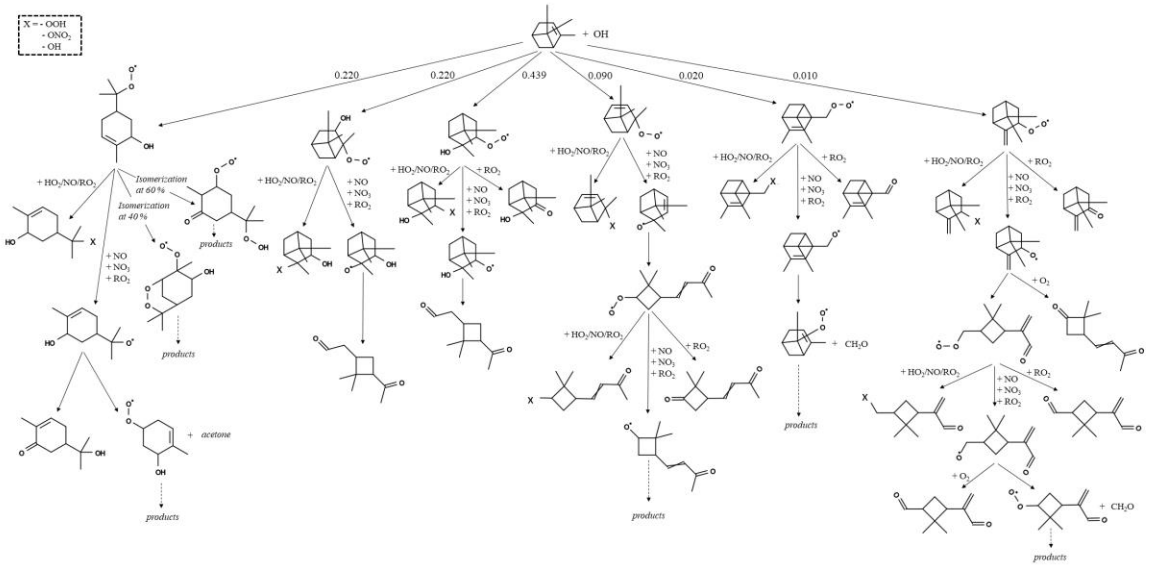

Figure 2.1: Initial oxidation pathways of α-pinene oxidation with OH as represented in GECKO-A.

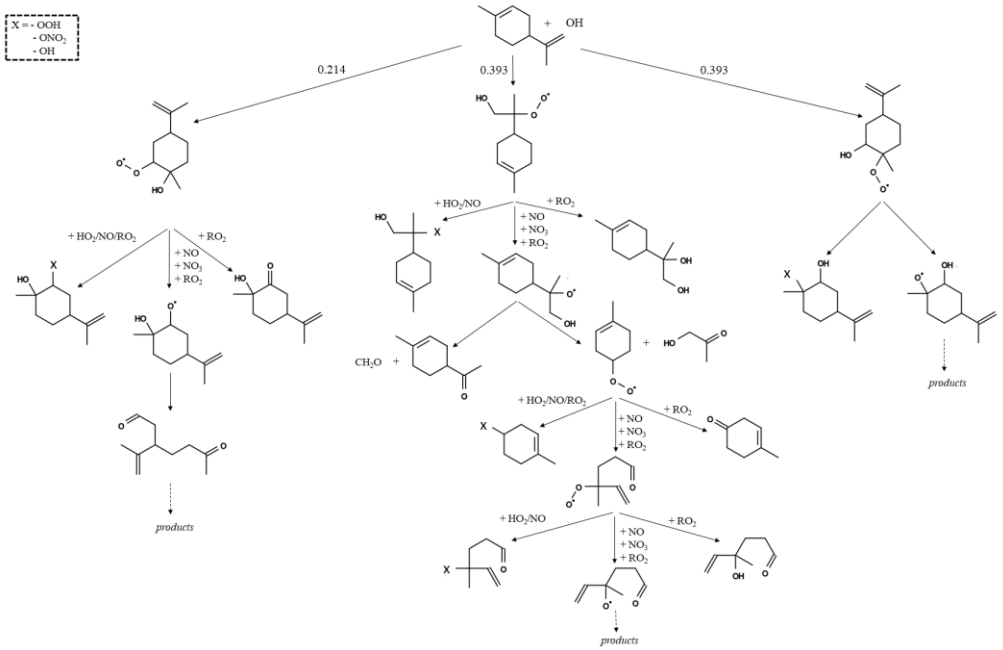

Figure 2.2: Initial oxidation pathways of limonene oxidation with OH as represented in GECKO-A.

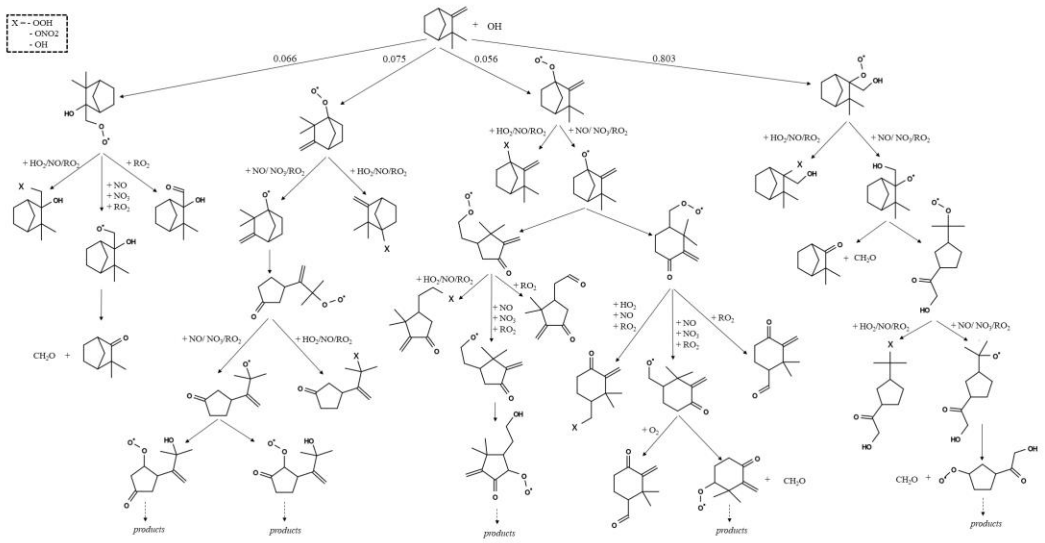

Figure 2.3: Initial oxidation pathways of camphene oxidation with OH as represented in GECKO-A.

2.2.2 O_3 reaction scheme

The initial oxidation pathways of O_3-initiated oxidation of α-pinene, limonene, and camphene are shown in Figs. A1, A2, and A3, respectively. The reaction starts with the addition of O_3 to the C=C double bond of the parent compound to form an ozonide, which rapidly undergoes bond cleavage to form a biradical Criegee intermediate bearing a carbonyl substituent for terpenes with an endocyclic double bond, or a biradical Criegee intermediate and a carbonyl for terpenes with an exocyclic double bond. The Criegee intermediate can stabilize by collisions and/or decompose (after possible rearrangement) to form peroxy radicals. The stabilized Criegee intermediates (SCI) undergo bimolecular reactions with H_2O, CO, NO and/or NO_2. The peroxy radicals then react with HO_2/NO/RO_2 to form stable products or react with NO/NO_3/RO_2 to form alkoxy radicals. For α-pinene, the alkoxy radicals either react with O_2 or decompose to form formaldehyde and peroxy radicals. The peroxy radicals further react to form peroxy acid, carboxylic acid, and CO_2.

For limonene, the alkoxy radical reactions primarily lead to the formation of organic nitrates, organic hydroperoxides, carboxylic acids, and peroxy acids. For camphene, the ozonide decomposes to form (1) camphenilone, a stable bicyclic product that has been observed experimentally by Calogirou et al. (1999) and Hakola et al. (1994); and (2) a bicyclic peroxy radical and formaldehyde, consistent with the camphene + O_3 mechanism reported by Gaona-Colmán et al. (2017). The bicyclic peroxy radical reacts with HO_2/NO/RO_2 to form stable products or reacts with NO/NO_3/RO_2 to form alkoxy radical which then further reacts to form five-membered ring products.

2.2.3 NO_3 reaction scheme

The initial oxidation pathways of NO_3-initiated oxidation of α-pinene, limonene, and camphene are shown in Figs. A4, A5, and A6, respectively. The NO_3 radical attacks the C=C double bond to form a nitratoalkyl radical which undergoes rapid reaction with O_2 to form a nitratoalkylperoxy radical. The nitratoalkylperoxy radicals of all three compounds react similarly in three ways: (1) with NO to form dinitrates; (2) with HO_2 or RO_2 to form nitratocarbonyls, nitratoalcohols, and nitratoperoxides (Calogirou et al., 1999); and (3) with NO/NO_3/RO_2 to form nitratoalkoxy radicals, which react further to form multifunctional products.

2.3 Simulation conditions

The objective of the chamber reactivity simulations was to compare GECKO-A model output with published SOA chamber data (Table 2.1). Here, no attempt is made to strictly reproduce the conditions of a given chamber experiment. Since the first objective

of this study focuses on the ability of the model to capture the major trends observed in chamber data (e.g., SOA yields and major species), the simulation conditions were therefore set to mimic (or be representative of) typical chamber conditions. Comparative analyses were performed for the precursors α-pinene and limonene, since they are among the well-studied monoterpenes in environmental chambers and sufficient data exist for measurement-model comparison. These simulations, chamber reactivity simulations, included photooxidation (P) and dark ozonolysis (DO) conditions, which were differentiated by the initial concentrations of NO, HONO, and O_3 as shown in Table 2.1. For both the P and DO conditions, the initial hydrocarbon mixing ratios were set at a relatively low (50 ppb) and a relatively high (150 ppb) level as compared with published chamber studies. This resulted in a total of four chamber reactivity simulations for each monoterpene precursor. In each simulation, 1 μg m^{-3} of organic seed with molecular weight of 250 g mol^{-1} was added to initiate gas/particle partitioning.

The objective of the controlled reactivity simulations was to examine SOA formation by camphene in the context of well-studied monoterpenes, specifically α-pinene and limonene, under controlled tropospheric conditions (Table 2.2). In these simulations, the gas-phase chemistry was not controlled by the individual precursors, but by other organic compounds as occurs in the ambient atmosphere. A mixture of ethane (10 ppb) and formaldehyde (50 ppb) was used to buffer (i.e. control) the gas-phase reactivity. Hence, the levels of the oxidants do not change when relatively small amounts of precursor were added in the simulation and therefore allows a straightforward comparison of oxidation mechanisms of the various terpenes. The NO_x and O_3 mixing ratios were held constant at

values of 1 ppb and 30 ppb respectively throughout the simulation. The controlled reactivity simulations included 0.1 ppb of initial precursor and 10 μg m^{-3} of organic seed.

All box-model simulations were performed under the following environmental conditions: temperature was fixed at 298 K; humidity was held at 5 %; and the solar zenith angle (required to compute the photolysis frequencies) was set at 50°, except for dark ozonolysis conditions where no photolysis was considered.

Table 2.1: Initial conditions for α-pinene and limonene chamber reactivity simulations.

Abbreviation	Description	HC (ppb)	NO (ppb)	HONO (ppb)	O_3 (ppb)	Organic seed (μg m^{-3})
P_LHC	Photooxidation Lower Hydrocarbon	50	110	10		1
P_HHC	Photooxidation Higher Hydrocarbon	150	110	10		1
DO_LHC	Dark Ozonolysis Lower Hydrocarbon	50	16		500	1
DO_HHC	Dark Ozonolysis Higher Hydrocarbon	150	16		500	1

Table 2.2: Initial conditions for camphene, α-pinene, and limonene controlled reactivity simulations. The levels of O_3 and NO_x were fixed during these simulations.

Abbreviation	Description	HC (ppb)	NO (ppb)	O_3 (ppb)	C_2H_6 (ppm)	CH_2O (ppb)	Organic seed (μg m^{-3})
CR	Controlled Reactivity	0.1	1	30	10	50	10

2.3 Results

2.3.1 Chamber reactivity simulations

2.3.1.1 Model-measurement comparison

In Fig. 2.4, SOA yields from the chamber reactivity simulations are shown with measured SOA yields from chamber studies. SOA data (see Table A1) were compiled from 12 published chamber studies (e.g., Chen et al., 2017; Griffin et al., 1999; Kim and Paulson, 2013; Kourtchev et al., 2014; Ng et al., 2007; Yu et al., 1999) in which α-pinene or limonene was used as a precursor and final SOA mass, SOA yield, and reacted hydrocarbon concentration (ΔHC) were reported (at least two of the three quantities). For the α-pinene photooxidation data, there is an apparent cluster around an SOA yield of 0.2 for SOA mass < 150 μg m^{-3} with which the model agrees (Fig. 2.4a). The scatter in the data is due to varying experimental conditions (e.g., temperature and NO_x mixing ratio). As previously observed, SOA yields of α-pinene tend to be higher at lower temperatures and lower NO_x conditions (higher initial VOC/NO_x ratios) (Kim and Paulson, 2013; Pathak et al., 2007b). For example, the two relatively high SOA yields (0.38 at 29.3 μg m^{-3} and 0.46 at 121.3 μg m^{-3}) had relatively low initial NO_x concentrations (Ng et al., 2007), while the two relatively low SOA yields (0.059 at 44 μg m^{-3} and 0.06 at 4.5 μg m^{-3}) had relatively high initial NO_x concentrations (Kim and Paulson, 2013; Ng et al., 2007). For mass loadings > 150 μg m^{-3}, α-pinene photooxidation SOA yield data plateaus at approximately 0.3, which also is captured by the model. In contrast, for limonene photooxidation, experimental data show a linear trend in the SOA yield as a function of SOA mass (for SOA mass > 25 μg m^{-3}), and the SOA yield does not plateau at higher SOA mass loadings. The observed linear

trend in SOA yield as a function of SOA mass is reflected in the model simulations (Fig. 2.4c). For α-pinene ozonolysis (Fig. 2.4b), there is an apparent cluster around an SOA yield of 0.2 for SOA mass < 200 μg m^{-3} with which the model agrees. The SOA yield plateaus at approximately 0.4 for SOA mass > 200 μg m^{-3}; the model simulations do not extend to this high mass range. For limonene ozonolysis, Fig. 2.4d shows the chamber SOA yield plateauing at approximately 0.8 (for mass loadings > 200 μg m^{-3}) which is captured by the model simulations. Overall, the model agrees well with the observed trends in SOA yield as a function of SOA mass.

Table 2.3 shows the simulated SOA mass-weighted average oxygen/carbon (O/C) ratios for α-pinene photooxidation (O/C = 0.93), α-pinene ozonolysis (O/C = 0.64), limonene photooxidation (O/C = 0.96), and limonene ozonolysis (O/C = 0.68). For α-pinene, the simulated SOA from photooxidation had higher average O/C than from ozonolysis. This is consistent with experiments by Kourtchev et al. (2015) in which the reported O/C for OH-initiated α-pinene SOA was higher than for α-pinene SOA initiated by ozonolysis. The same trend was predicted for limonene. Generally, the simulated O/C values were high relative to values reported from chamber studies. Reported average O/C values from chamber studies range from 0.3 to 0.65 for α-pinene photooxidation (e.g., Lambe et al., 2015; Pfaffenberger et al., 2013), 0.22 to 0.55 for α-pinene ozonolysis (e.g., Chen et al., 2011; Chhabra et al., 2010; Kourtchev et al., 2015), and 0.23 to 0.5 for limonene ozonolysis (e.g., Draper et al., 2015; Heaton et al., 2007; Walser et al., 2008). Factors known to affect the O/C ratios include mass loading, OH exposure (defined as the integral of OH concentration and residence time (Lambe et al., 2015)), and oligomerization.

Shilling et al. (2009) showed the dependency of O/C ratios on mass loadings for α-pinene, in which O/C ratio decreased from 0.45 to 0.38 as mass loading increased from 0.5 to 15 μg m^{-3}. Mass loading is not likely driving the differences in simulations and observations here, since the simulated mass loadings were similar to the mass loadings of the chamber experiments (e.g., Chhabra et al., 2011; Shilling et al., 2009) with which the O/C ratios were compared. Regarding OH exposure, calculated OH exposures for the photooxidation simulations (Table 2.3) were within the typically reported OH exposure ranges (5.4×10^{10}–4.0×10^{11} molec cm^{-3} s) from the chamber photooxidation experiments (e.g., Lambe et al., 2015; Pfaffenberger et al., 2013). Therefore, one explanation for the lower observed O/C values is the loss of H_2O during oligomerization (Chhabra et al., 2010; Reinhardt et al., 2007), a process that was likely occurring in the experiments but was not represented in the GECKO-A simulations. Additionally, for dark ozonolysis, the OH scavengers typically present in chamber experiments (e.g., Kourtchev et al., 2015; Shilling et al., 2009) were absent from the simulations.

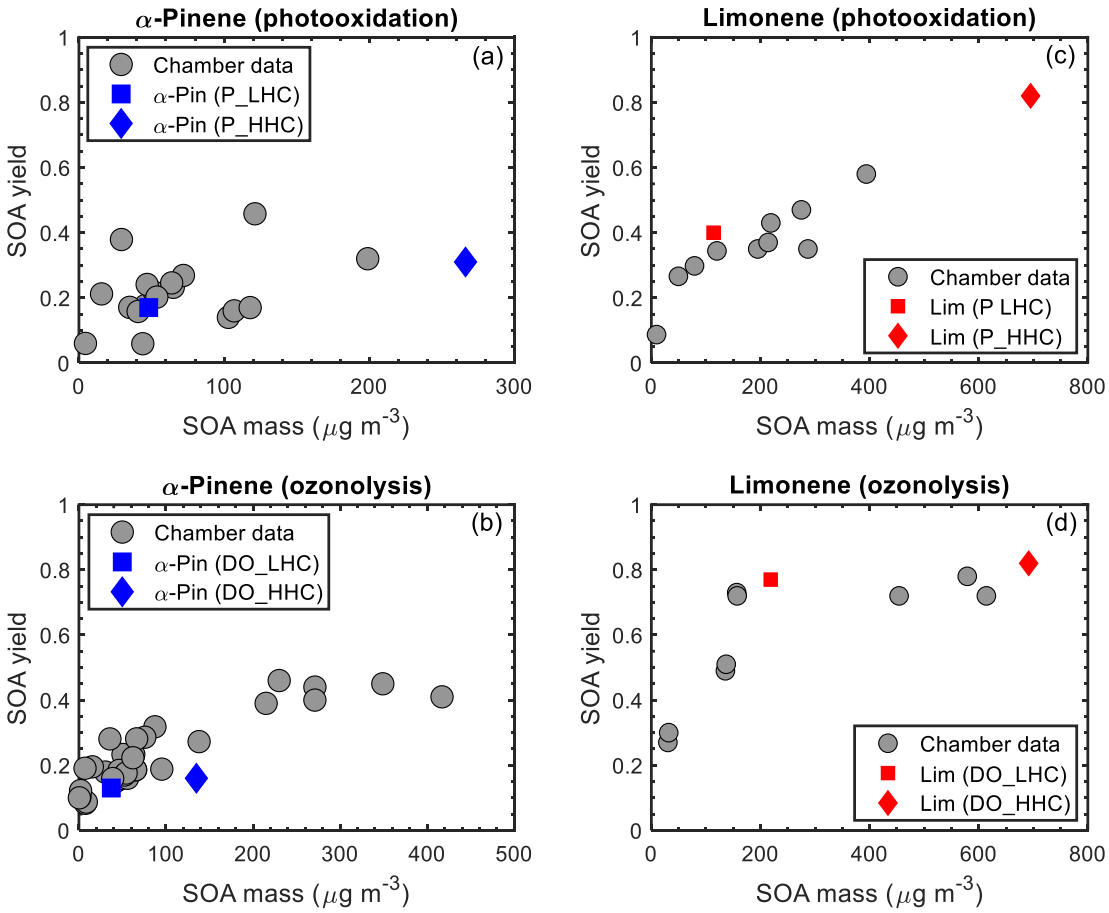

Figure 2.4: GECKO-A SOA yields are represented by blue (α-pinene) and red (limonene) markers; chamber SOA yields are represented by grey markers. The initial hydrocarbon mixing ratios are differentiated by shape; squares represent the simulation using the lower hydrocarbon (LHC) mixing ratio and diamonds the simulation using the higher hydrocarbon (HHC) mixing ratio.

Table 2.3: Calculated average mass-weighted O/C ratio and OH exposure at the end of the α-pinene and limonene photooxidation and ozonolysis simulations.

	Average O/C	OH exposure (molec cm^{-3} s)
α-Pinene photooxidation	0.93	6.7×10^{10}
α-Pinene ozonolysis	0.64	1.5×10^{10}
Limonene photooxidation	0.96	9.1×10^{10}
Limonene ozonolysis	0.68	1.7×10^{10}

2.3.1.2 Major products simulated for α-pinene and limonene

The results from the simulations using the lower hydrocarbon mixing ratio (LHC) and higher hydrocarbon mixing ratio (HHC) were qualitatively similar. Thus, here and in subsequent sections, only the results for the LHC simulations are shown and discussed; the corresponding figures for the HHC simulations are provided in the supplement. Figures 2.5 and 2.6 show the chemical structures and molecular formulae of the top 10 products in the gas and particle phases from the α-pinene photooxidation simulation. While the top 10 products may evolve with reaction time, only the final top 10 products are shown in Fig. 2.5. The top 10 gas-phase products (dominated by carbonyl, carboxyl, and nitrate functional groups) account for 46 % of the reacted α-pinene carbon mass, with acetone being the top contributor. Two of the top 10 gas-phase products, pinonic acid (i.e. (3-acetyl-2,2-dimethylcyclobutyl)acetic acid) and pinonaldehyde (i.e. (3-acetyl-2,2-dimethylcyclobutyl)acetaldehyde) are among the most commonly reported products in experimental studies (e.g., Lee et al., 2006b). The top 10 particle-phase products (dominated by carbonyl, carboxyl, hydroxyl, hydroperoxide, and nitrate functional groups) account for 42 % of the SOA mass and 7 % of the reacted α-pinene carbon mass. For limonene photooxidation (Figs. A10 and A11), the top 10 gas-phase products account for 34 % of reacted limonene, while the top 10 particle-phase products account for 50 % of the SOA mass and 20 % of the reacted limonene carbon mass. The top 10 particle-phase products are dominated by dinitrate and carbonyl functional groups, indicating the possible influence of multigeneration products from peroxy radicals + NO reactions.

The top 10 gas- and particle-phase products from the α-pinene ozonolysis simulation are shown in Fig. 2.6. The top 10 gas-phase products account for 62 % of the reacted α-pinene carbon mass, while the top 10 particle-phase products account for 42 % of the SOA mass and 6 % of the reacted α-pinene carbon mass. Three of the top 10 products have been previously reported in experimental product studies of α-pinene ozonolysis (e.g., Jang and Kamens, 1999; Larsen et al., 2001; Yu et al., 1999). They include one particle-phase product, pinic acid (3-(carboxymethyl)-2,2-dimethylcyclobutane-1-carboxylic acid); and two gas-phase products, pinonic acid (i.e. (3-acetyl-2,2-dimethylcyclobutyl)acetic acid) and pinonaldehyde (i.e. (3-acetyl-2,2-dimethylcyclobutyl)acetaldehyde). For limonene ozonolysis (Figs. A12 and A13), the top 10 gas-phase products account for 24 % of reacted limonene, while the top 10 particle-phase products account for 37 % of the SOA mass and 27 % of the reacted limonene carbon mass. The top 10 particle-phase products were dominated by carbonyl, carboxyl, hydroxyl, and hydroperoxide, indicating the influence of multi-generational products via peroxy radicals + HO_2/RO_2.

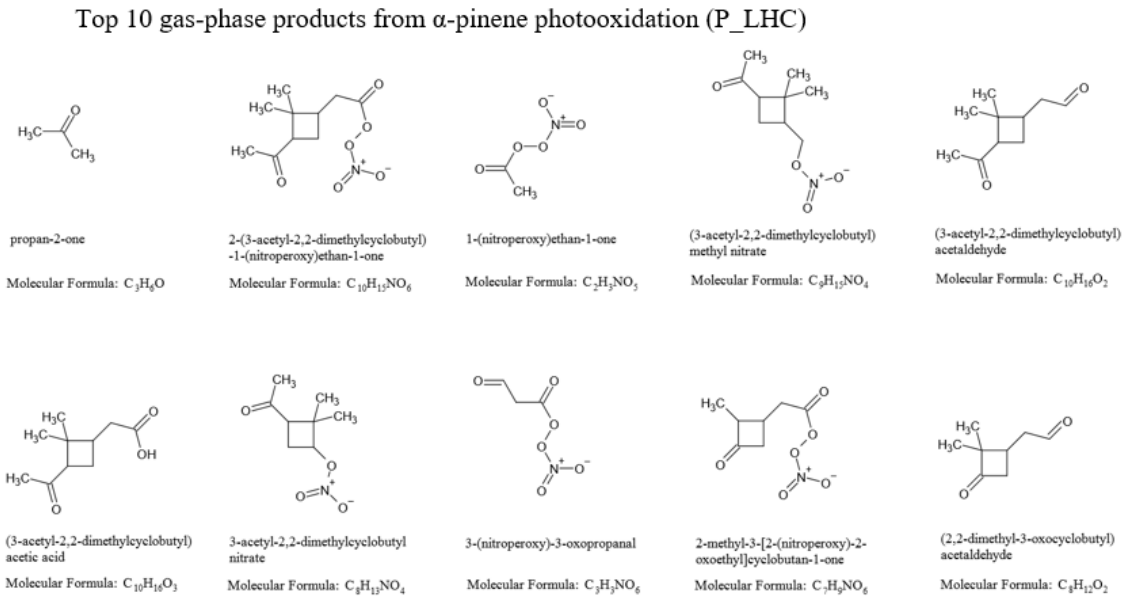

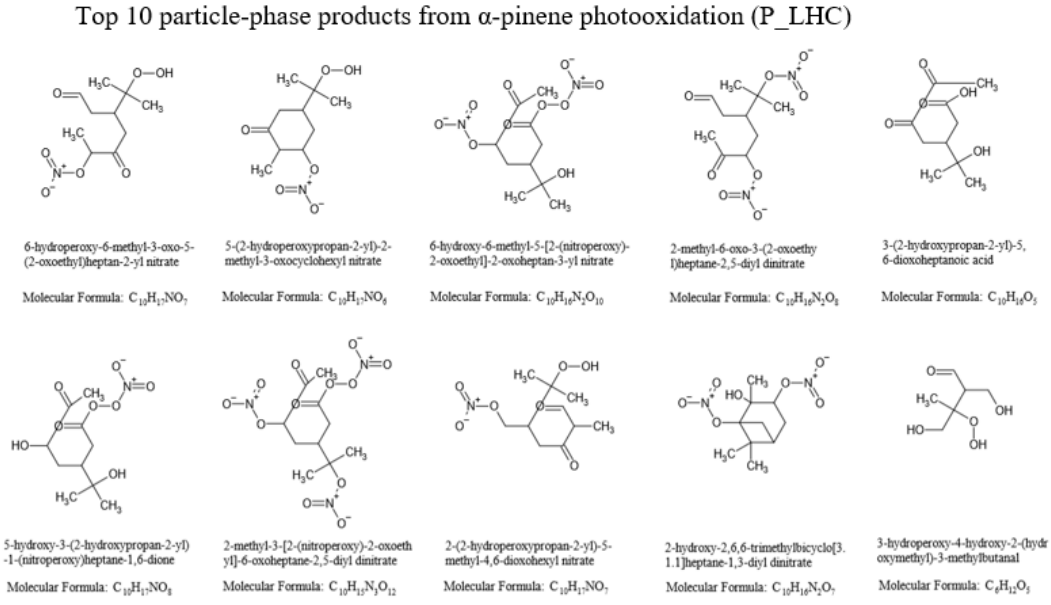

Figure 2.5: Simulated top 10 gas and top 10 particle-phases products from α-pinene photooxidation (P_LHC).

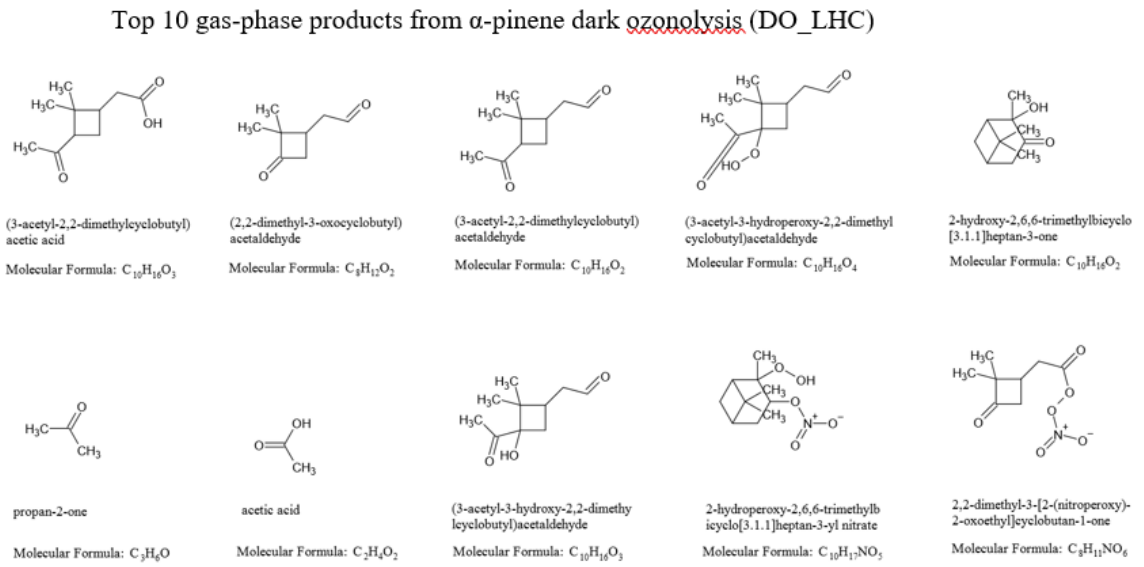

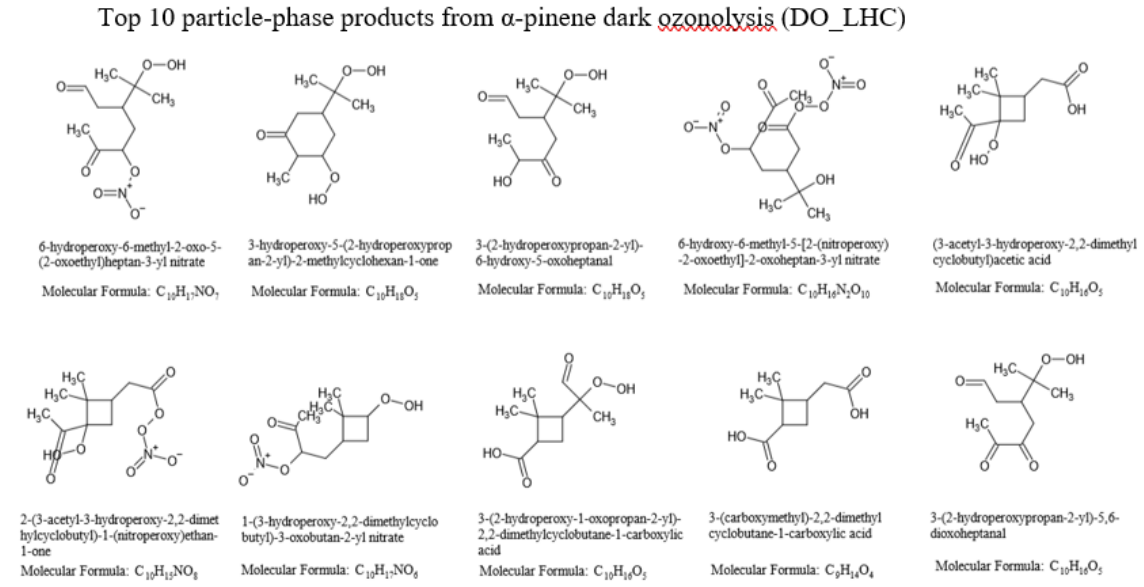

Figure 2.6: Top 10 gas phase and top 10 particle-phase products from α-pinene dark ozonolysis (DO_LHC) simulations.

2.3.1.3 Modeled SOA yield and carbon budget

Given the skill of the model in representing published chamber data (at both macroscopic and molecular levels), the model was used to explore the carbon budget in the simulations during photooxidation and ozonolysis. The time evolution of SOA yields for α-pinene and limonene during photooxidation and ozonolysis, as simulated by GECKO-A, is shown in Figs. 2.7a and 2.7b respectively. Also shown are the corresponding final SOA mass concentrations. As has been previously reported (Lee et al., 2006b), limonene had a higher SOA yield than α-pinene under both photooxidation and ozonolysis conditions.

The time evolution of the carbon budget during the photooxidation and ozonolysis simulations is shown in Figs. 2.7c to 2.7f. During photooxidation (Fig. 2.7c), the precursors were oxidized largely by OH and O_3 (see Fig. A7 for the relative fractions of precursor reacting with each oxidant), forming organic oxidation products in the gas phase. These gaseous oxidation products partitioned into the particle phase if their volatility was low enough. Oxidation products that remained in the gas phase reacted with OH, NO_3, and/or O_3, or were photolyzed if a chromophore was present; these subsequent gas-phase reactions formed additional oxidation products that partitioned to the particle phase or continued to react in the gas phase. At the end of 12 hours of photooxidation, the α-pinene system was dominated by organic oxidation products in the gas phase (70 %), with the remaining fractions being organic oxidation products in the particle phase (8 %) and $CO+CO_2$ (22 %). The high yield of gas-phase organics is largely influenced by the high concentrations of acetone and volatile C8 to C10 species (see Fig. 2.5 for top gas-phase products and Fig. A9a for the gas- and particle-phase product distribution). As shown in the α-pinene + OH

reaction scheme (Fig. 2.1) acetone is formed when the monocyclic alkoxy radical decomposes via O_2 addition. For limonene photooxidation (Fig. 2.7e), the concentration of acetone is lower than for α-pinene and more of the C8 to C10 gaseous species are further oxidized and partitioned into the particle phase (Fig. A9c). This resulted in a final distribution of 50 % gas-phase organic products, 20 % particle-phase organic products, and 30 % $CO+CO_2$. The simulated acetone yields are qualitatively consistent with experimental data that have shown yields of acetone from α-pinene photooxidation (Lee et al., 2006b; Wisthaler et al., 2001) can be up to four orders of magnitude higher than from limonene photooxidation (Lee et al., 2006b; Reissell et al., 1999).

For the α-pinene ozonolysis system (Fig. 2.7d), at the end of the simulation 88 % of the carbon is gas-phase organic products, 7 % particle-phase organic products, and 5 % $CO+CO_2$. For limonene ozonolysis (Fig. 2.7f), 50 % of the carbon fraction is gas-phase organics, 43 % particle-phase organics, and 7 % $CO+CO_2$. The higher particle-phase fraction for limonene ozonolysis is a result of the C8 and C10 organic products of limonene being more highly functionalized and thus partitioned to the particle phase (Figs. A9d and A13); whereas the C8 and C10 organic products of α-pinene are more volatile and partitioned to the gas phase (Figs. 2.7 and A9b).

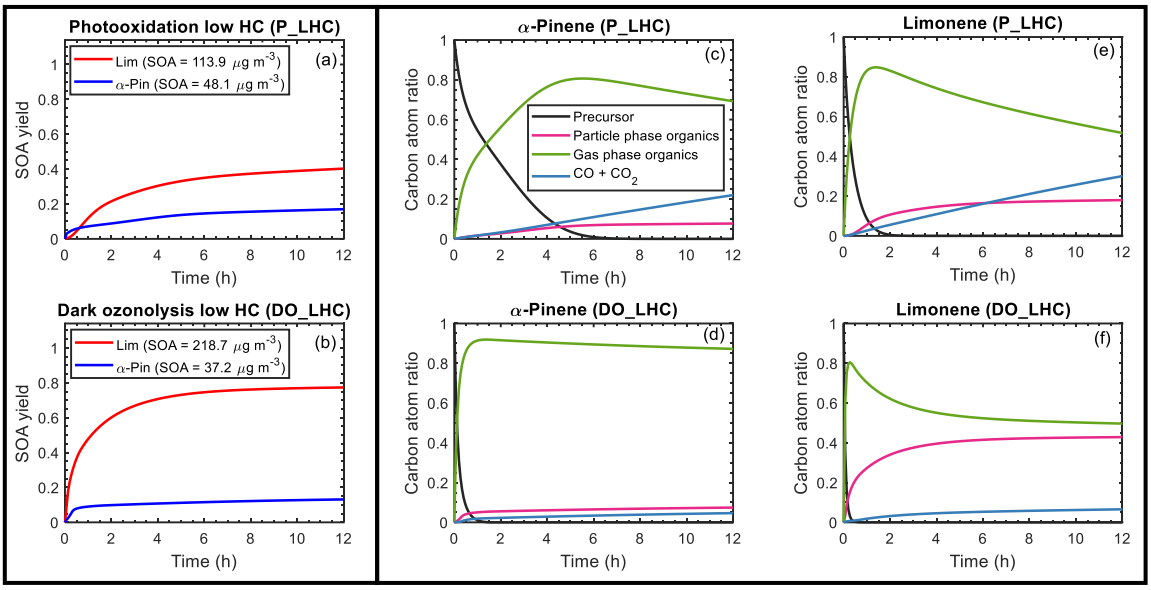

Figure 2.7: Simulated SOA yield (a and b) and carbon budget (c to f) as a function of time for α-pinene and limonene during photooxidation (a, c, e) and dark ozonolysis (b, d, f). The SOA yield curve for α-pinene is represented by a blue line; limonene is represented by a red line. For the carbon budget plots, the mixing ratios of the precursor (black line), particle-phase organics (magenta line), gas-phase organics (green line), and $CO+CO_2$ (blue line) are expressed as carbon atom ratios (ppbC/initial precursor in ppbC). The results shown are for the low hydrocarbon mixing ratio (50 ppb) simulations.

2.3.2 Controlled reactivity simulations

The GECKO-A simulations captured trends (e.g., SOA yields and major products) observed in chamber studies (section 3.1) for α-pinene and limonene (two common terpene model surrogates). Therefore, the GECKO-A model was used to perform a detailed study of SOA formation from camphene under idealized atmospheric ("controlled reactivity") conditions, which were compared with analogous simulations for α-pinene and limonene.

2.3.2.1 Gas-phase chemistry

Time-dependent mixing ratios of HO_2, OH, and NO_3 are shown in Fig. 2.8 for the controlled reactivity simulations performed at 0.1 ppb of HC_o (camphene, α-pinene, or limonene) and 10 µg m^{-3} of organic seed. The O_3 and total NO_x levels were fixed so that the oxidant (OH, O_3, and NO_3) levels would remain stable during the simulations. The time profiles of HO_2, OH, and NO_3 are independent of the precursor, confirming that the gas-phase oxidant levels are controlled by the added ethane and formaldehyde. This allows for a comparative assessment of the monoterpenes. The reaction rate of camphene with O_3 is extremely slow (two and three orders of magnitude lower than the rate constants for α-pinene+O_3 and limonene+O_3 respectively (Atkinson and Arey, 2003a)); thus camphene predominately reacts with OH in the simulations, while α-pinene and limonene react with O_3 and OH (see Fig. A26 for relative fractions).

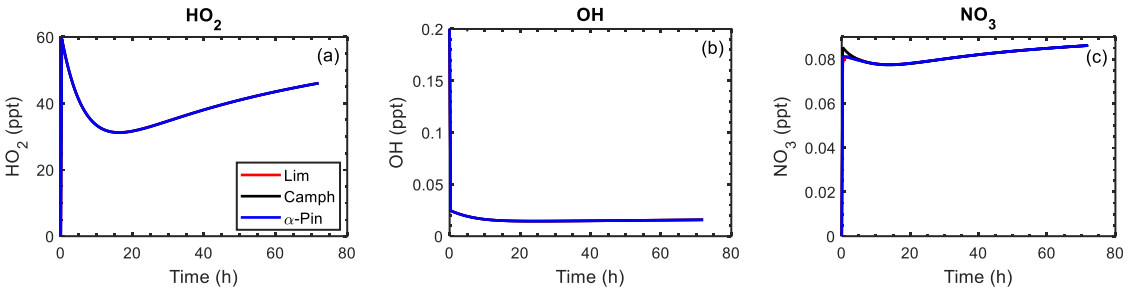

Figure 2.8: Mixing ratios of HO_2, OH, and NO_3 as function of time for limonene (red line), camphene (black line), and α-pinene (blue line) during the controlled reactivity simulations with 0.1 ppb of HC_o and 10 µg m^{-3} of organic seed. By design, the profiles of the mixing ratios for each precursor overlap except for at the very beginning of the NO_3 profile.

2.3.2.2 Simulated SOA formation

Figure 2.9 illustrates the simulated SOA yields as a function of atmospheric aging time (Fig. 2.9a) and the SOA yield as function of reacted HC concentration (Fig. 9b) for the controlled reactivity simulations. The atmospheric aging time, τ is defined as:

$$\tau = \frac{1}{[\mathrm{OH}]_{atm}} \int_0^t [\mathrm{OH}]_{sim} dt \quad (1)$$

where $[OH]_{atm}$ is the atmospheric OH concentration (2×10^6 molecule cm^{-3} was assumed) and $[OH]_{sim}$ is the simulated OH concentration. Camphene was predicted to form more SOA (0.26 μg m^{-3}) than α-pinene (0.14 μg m^{-3}) but less than limonene (0.42 μg m^{-3}) after 14.5 hours of aging time (Fig. 2.9a). The simulation results in Fig. 2.9b show that camphene, which reacts predominantly with OH (Fig. A26), forms low volatility products (more SOA at lower ΔHC) at the start of the reaction than α-pinene and limonene. However, after the precursor is completely consumed, the SOA yield of limonene exceeds that of camphene. The relatively shorter lifetimes of limonene with the oxidants allow more time for limonene oxidation products to react further to form extremely low volatility products. As previously reported (Lee et al., 2006b), and as simulated herein, limonene has the highest SOA yield among well studied monoterpenes. However, the final SOA yield of camphene was relatively high, approximately twice that of α-pinene.

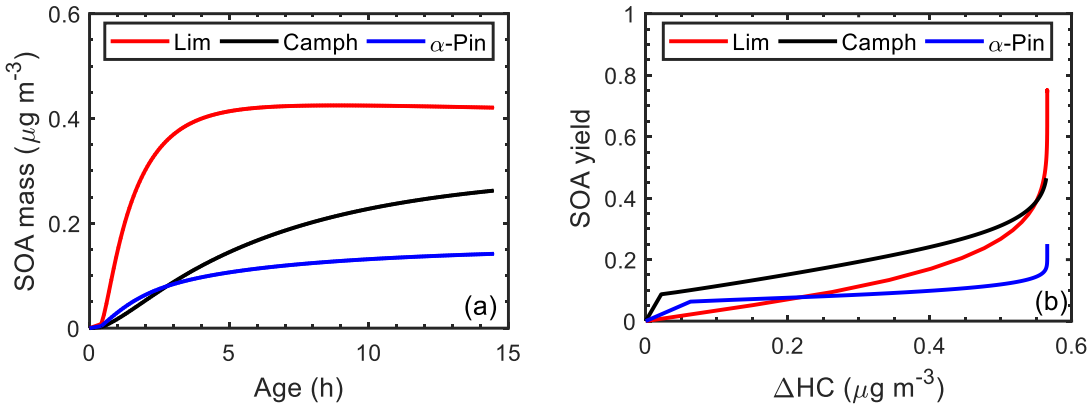

Figure 2.9: (a) Simulated SOA mass as a function of atmospheric aging time (reaction with OH) and (b) simulated SOA yield as a function of reacted hydrocarbon concentration (ΔHC) during controlled reactivity simulation at 0.1 ppb HC_o with 10 µg m^{-3} seed for limonene (red line), camphene (black line), and α-pinene (blue line).

2.3.2.3 Gas- and particle-phase product distribution

Figure 2.10 shows the product distribution in the gas- and particle-phases after 72 hours (equivalent to 14.5 hours of atmospheric OH aging time) for the controlled reactivity simulations. While thousands of secondary species are formed during the oxidation of a given monoterpene, only species that contribute ≥ 0.01 % of the total gas- or particle-phase mass were included in Fig. 2.10. Also, all C1 species, as well as seven of the C2 gas-phase products (whose concentrations were largely a direct result of ethane chemistry) were omitted from Fig. 2.10. For camphene (Fig. 2.10a), the particle phase is largely dominated by C10 species with 3 to 5 functional groups, followed by highly functionalized C7 species (typically with 4 to 5 functional groups). Similarly, for limonene (Fig. 2.10b), the particle phase is dominated by C10 species with 4 to 5 functional groups, followed by C7 to C9 species with 4 to 5 functional groups. However, for α-pinene (Fig. 2.10c), there is a broad distribution of C8 to C10 products (with 3 to 4 functional groups) contributing to the

particle phase. Generally, the volatility of particle-phase products from camphene and limonene was lower than from α-pinene. As shown in Fig. 2.10a, a large fraction of gas-phase products from camphene, as compared to limonene, is composed of C9 and C10 products whose volatility was not low enough to partition to the particle phase. This further explains the SOA yields shown in Fig. 2.9b where limonene SOA yield exceeded camphene SOA yield at the end of the reaction.

Figure 2.11 shows the final mass percentages of α-pinene, camphene, and limonene particle-phase oxidation products grouped into three volatility categories. The volatility categories were assigned based on the calculated mass saturation concentrations (C*) of the simulated products. Log C* values in the range of < -3.5, -3.5 to -0.5, and -0.5 to 2.5 were assigned respectively as extremely low-volatility, low-volatility, and semi-volatile organic compounds (ELVOCs, LVOCs, and SVOCs) (Chuang and Donahue, 2016; Zhang et al., 2015). Limonene, which had the highest simulated SOA yield among the three studied monoterpenes, was largely LVOCs (59 %), followed by ELVOCs (24 %) and then SVOCs (17 %). Camphene SOA was also largely LVOCs (67 %), followed by SVOCs (28 %), and then a significantly lower fraction of ELVOCs (4 %) than limonene. In contrast, α-pinene SOA was dominated by SVOCs (50 %), followed by LVOCs (48 %), and then ELVOCs (2 %). For α-pinene and camphene, intermediate-volatility organic compounds (IVOCs) were less than 1 % of the SOA mass. For experimental studies of α-pinene ozonolysis, Zhang et al. (2015) reported a fractional contribution of ~68 % SVOCs to final SOA mass, which is similar to the contribution predicted using GECKO-A.

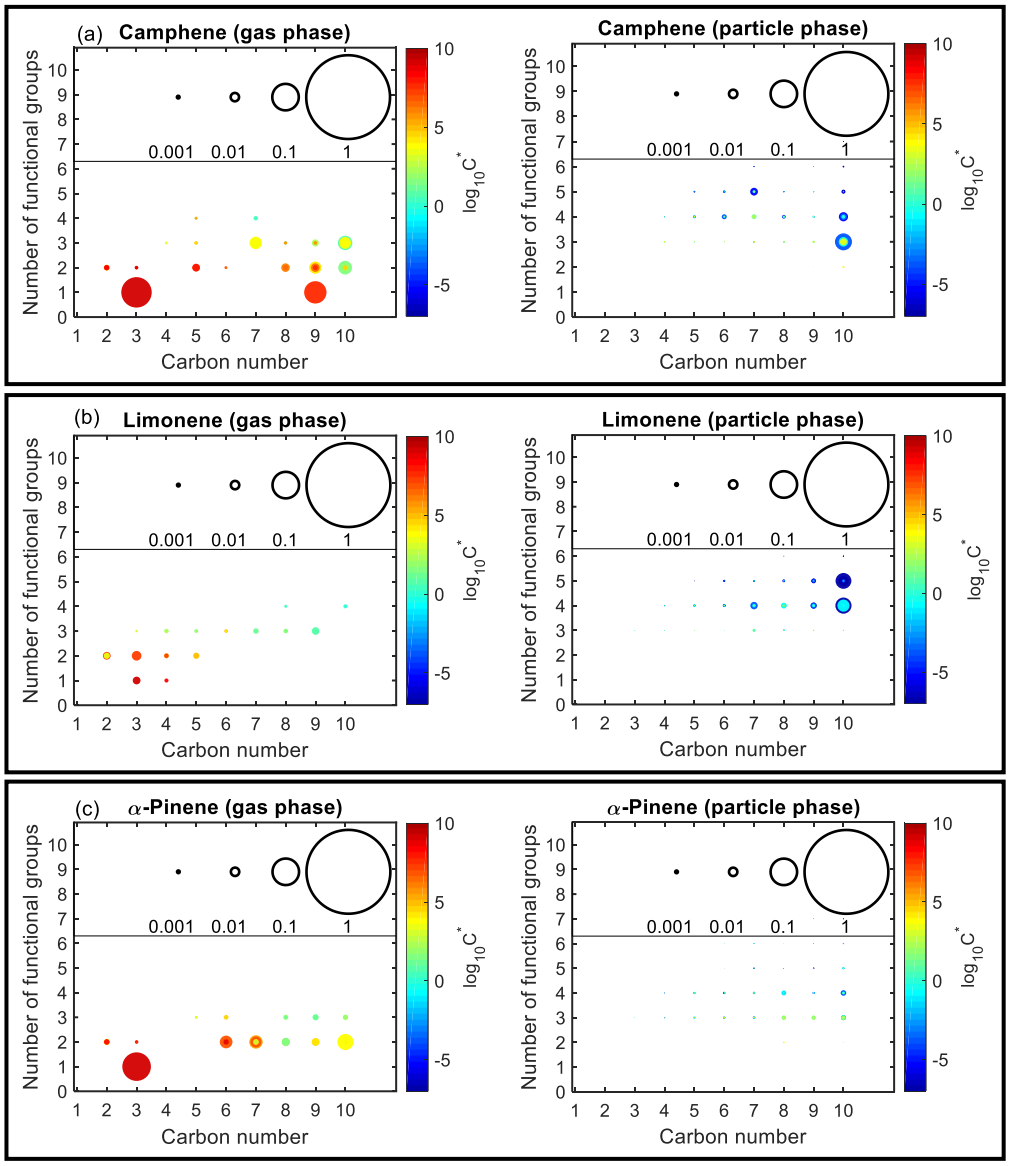

Figure 2.10: Number of functional groups associated with gas- and particle-phase species as a function of carbon number. Results are shown for camphene, α-pinene, and limonene after 72 hours of oxidation under controlled reactivity condition. The markers are sized by the ratio of their mixing ratio (in ppbC) to the initial mixing ratio of the precursor (in ppbC). The colors of the markers are scaled by volatility (represented by saturation concentration, C*).

2.3.2.4 Using α-pinene limonene as a surrogate for camphene

For the controlled reactivity simulations, the final SOA mass and yield of camphene (0.26 μg m^{-3}, 0.46) were between the final SOA mass and yield of α-pinene (0.14 μg m^{-3}, 0.25) and limonene (0.42 μg m^{-3}, 0.74). This suggests that camphene could potentially be represented in models as a 50/50 mixture of α-pinene + limonene. To test this, a controlled reactivity simulation was run with 50 ppt α-pinene + 50 ppt limonene; simulation results were then compared with the simulation results for 0.1 ppb of camphene. Figure 2.12a shows that while the slopes of the SOA yield curves differ over the course of the reaction, the SOA masses (0.26 μg m^{-3} for 50 % α-pinene + 50 % limonene and 0.26 μg m^{-3} for camphene) and yields (0.46 for 50 % α-pinene + 50 % limonene and 0.47 for camphene) were approximately equal at the end of the simulation. However, the end of simulation particle-phase volatility distributions (Fig. 2.12b) are notably different. The 50 % α-pinene + 50 % limonene simulation had a significantly higher fraction (25 %) of ELVOCs, influenced by the low volatility limonene products, than the camphene simulation (4 %). These results suggest that while the final SOA mass and yield of the 50/50 α-pinene + limonene mixture were representative of camphene, the properties (e.g., volatility) of the particle-phase products were not. The volatility distributions will influence the formation of SOA at the lowest mass loadings and will also influence changes in SOA mass as a function of dilution, with the surrogate mixture (50 % α-pinene + 50 % limonene) producing less volatile SOA than predicted for camphene. Thus, the extent to which camphene can be represented by α-pinene + limonene will depend on the application. To improve the representation of camphene, a second simulation was run with 50 ppt α-pinene

+ 50 ppt limonene, where the rate constants of α-pinene and limonene were replaced with the rate constants of camphene during the chemical mechanism generation. However, the representation of camphene SOA by the 50/50 α-pinene + limonene mixture did not improve (resulted in higher final SOA yield of 0.51) when the rate constants of α-pinene and limonene were replaced with those of camphene (Fig. 2.12a). Also, representing camphene by the limonene mechanism with camphene rate constants did not improve the representation of camphene SOA (see Fig. A29). This illustrates the importance of both the reaction rates and structure on SOA formation from monoterpenes.

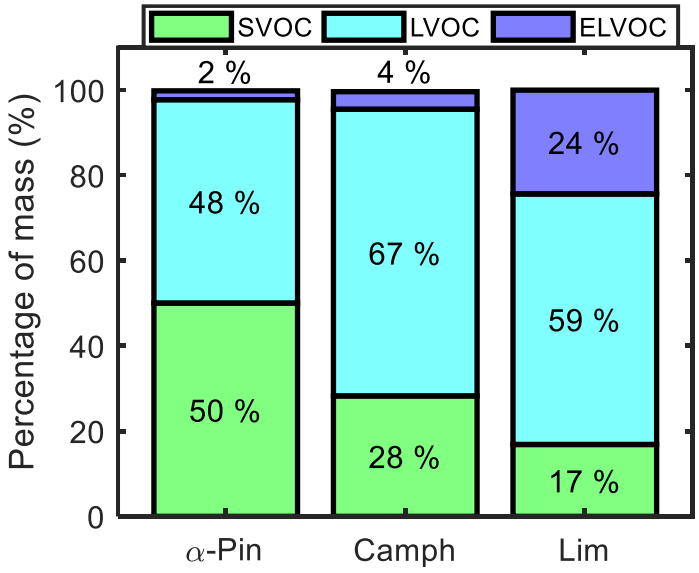

Figure 2.11: Mass percentage of four volatility categories in the particle phase at the end of the controlled reactivity simulations for α-pinene, camphene, and limonene.

To demonstrate the potential impact of including a parameterized representation of SOA formation by camphene in air quality models, SOA mass and yields were predicted for three wildland fire fuels based on the measured monoterpene distributions in Hatch et al. (2015) for black spruce, and Hatch et al. (2019) for Douglas fir and lodgepole pine. The top five monoterpenes by emissions factor (mass of compound emitted/mass fuel burned) represent ~70-80 % of the total monoterpene emission factor (EF) for each of these fuels. These top five monoterpenes were used to represent SOA formation for each fuel by normalizing the EF for each fuel; assigning α-pinene as the model surrogate for all measured compounds except limonene, including camphene; and then reassigning camphene as 50 % α-pinene and 50 % limonene. SOA mass concentrations and yields were predicted assuming a background PM level of 50 μg m^{-3} and ΔHC = 10 ppb and using published two-product SOA parameters based on Griffin et al. (1999) (Table A3) and volatility basis set (VBS) parameters (low NO_x, dry) based on Pathak et al. (2007b) (for α-pinene) and Zhang et al. (2006) (for limonene) (Table A4). The two model parameterizations were used to represent a range of potential outcomes. The SOA yields using the two-product parameters were lower than predicted here for α-pinene (~0.1), but similar for camphene (~0.6); using the VBS parameters, the yields were similar for α-pinene (~0.2) but higher than predicted here for camphene (~0.9). The total OA mass loadings in the parameterized SOA calculations were a factor of 3-6 higher than in the GECKO-A controlled reactivity simulations, which is consistent with the higher SOA yield for camphene predicted using the VBS parameters. The results of the SOA calculations are summarized in Table 2.4. For lodgepole pine, there is no change in SOA mass, because

camphene is not one of the top five monoterpenes by EF. However, for fuels in which camphene contributed significantly to the measured monoterpene EF, SOA mass increased by 43-50 % for black spruce and by 56-108 % for Douglas fir.

Table 2.4: SOA yield and mass predicted using 2-product and VBS parameters for top five monoterpenes by emission factor (EF) from black spruce, Douglas fir, and lodgepole pine.

		$Yield_{\alpha pin}$	$Yield_{lim}$	$SOA_{\alpha pin}$ ($\mu g\ m^{-3}$)	SOA_{lim} ($\mu g\ m^{-3}$)	SOA_{total} ($\mu g\ m^{-3}$)	% increase in SOA
				Black Spruce			
2-Product	Assignment 1	0.099	0.6	4.5	6.4	10.9	50 %
	Assignment 2	0.103	0.6	3.6	12.8	16.4	
VBS	Assignment 1	0.194	0.93	8.8	9.9	18.7	43 %
	Assignment 2	0.202	0.93	7	19.7	26.7	
				Douglas Fir			
2-Product	Assignment 1	0.098	0.6	4.5	6.1	10.6	108 %
	Assignment 2	0.108	0.6	2.5	19.6	22.1	
VBS	Assignment 1	0.194	0.93	8.9	9.4	18.3	56 %
	Assignment 2	0.203	0.93	6.6	21.9	28.5	
				Lodgepole Pine			
2-Product	Assignment 1	0.097	0.6	4.7	4.6	9.3	
VBS	Assignment 1	0.192	0.93	9.3	7.1	16.4	

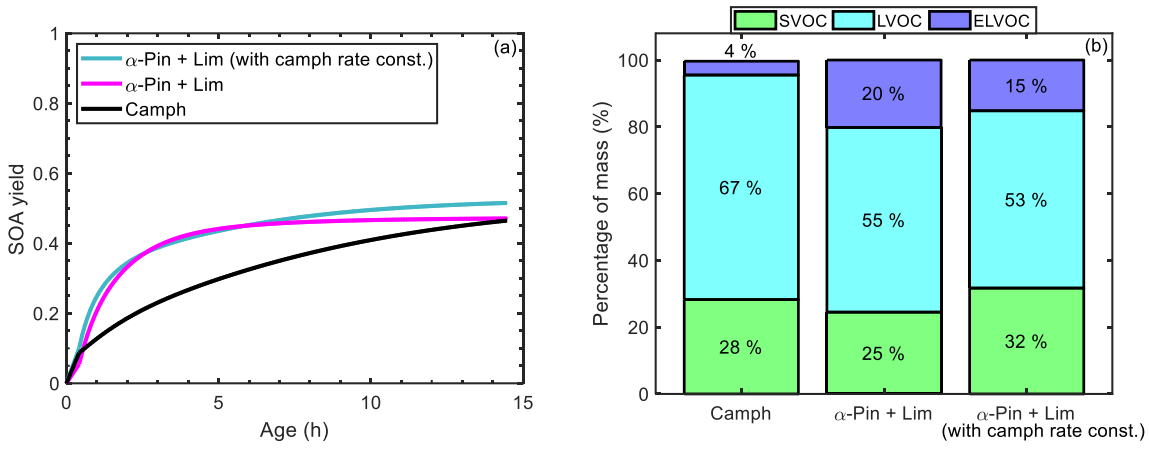

Figure 2. 12: (a) Simulated SOA yield as a function of atmospheric aging time for camphene (black line), 50 % α-pinene + 50 % limonene (magenta line), and 50 % α-pinene + 50 % limonene where the rate constants of α-pinene and limonene were replaced with the rate constants of camphene (green line); and (b) mass percentage of four volatility categories in the particle phase at the end of the controlled reactivity simulations for camphene, 50 % α-pinene + 50 % limonene, and limonene, and 50 % α-pinene + 50 % limonene where the rate constants of α-pinene and limonene were replaced with the rate constants of camphene.

2.4 Conclusions

While camphene is a ubiquitous monoterpene, measured in significant quantities from both biogenic and pyrogenic sources, little is known about SOA formation from camphene and there are no published parameterizations to represent camphene SOA in air quality models. GECKO-A simulations suggest that the initial organic oxidation products of camphene are of low volatility and can condense at low OA mass loadings; lower than oxidation products predicted for α-pinene and limonene. Predicted final SOA yields for camphene in the controlled reactivity simulations (~45 %) were in between those predicted for α-pinene (25 %) and limonene (~75 %), suggesting that SOA formation from camphene can be represented in air quality models assuming a 50/50 (α-pinene/limonene) surrogate

mixture. Calculations based on measured monoterpene distributions for three wildland fire fuels illustrate that accounting for camphene, in this case using the surrogate mixture and published SOA parameterizations for α-pinene and limonene, increased predicted SOA mass from monoterpenes by 43-108 %. This demonstrates the potential impact of representing SOA formation from camphene in air quality models, and the need for an appropriate parameterization. The surrogate mixture appears to represent the SOA mass and yield of camphene well, but not necessarily the volatility distribution of the products. Further modeling and/or experimental studies are needed to develop and test a suitable SOA parameterization for representing camphene in air quality models.

References

Akagi, S. K., Yokelson, R. J., Wiedinmyer, C., Alvarado, M. J., Reid, J. S., Karl, T., Crounse, J. D., and Wennberg, P. O.: Emission factors for open and domestic biomass burning for use in atmospheric models, Atmos. Chem. Phys., 11(9), 4039–4072, https://doi.org/10.5194/acp-11-4039-2011, 2011.

Akagi, S. K., Yokelson, R. J., Burling, I. R., Meinardi, S., Simpson, I., Blake, D. R., McMeeking, G. R., Sullivan, A., Lee, T., Kreidenweis, S., Urbanski, S., Reardon, J., Griffith, D. W. T., Johnson, T. J., and Weise, D. R.: Measurements of reactive trace gases and variable O_3 formation rates in some South Carolina biomass burning plumes, Atmos. Chem. Phys., 13(3), 1141–1165, https://doi.org/10.5194/acp-13-1141-2013, 2013.

Almatarneh, M. H., Elayan, I. A., Poirier, R. A., and Altarawneh, M.: The ozonolysis of cyclic monoterpenes: A computational review, Can. J. Chem., 96(3), 281–292, https://doi.org/10.1139/cjc-2017-0587, 2018.

Ambrose, J. L., Haase, K., Russo, R. S., Zhou, Y., White, M. L., Frinak, E. K., Jordan, C., Mayne, H. R., Talbot, R., and Sive, B. C.: A comparison of GC-FID and PTR-MS toluene measurements in ambient air under conditions of enhanced monoterpene loading, Atmos. Meas. Tech, 3(4), 959–980, https://doi.org/10.5194/amt-3-959-2010, 2018.

Amin, H. S., Hatfield, M. L., and Huff Hartz, K. E.: Characterization of secondary organic aerosol generated from ozonolysis of α-pinene mixtures, Atmos. Environ., 67, 323–330, https://doi.org/10.1016/j.atmosenv.2012.10.063, 2013.

Atkinson, R., and Arey, J.: Atmospheric chemistry of biogenic Organic Compounds, Accounts of Chemical Research, 31(9), 574–583, https://doi.org/10.1021/ar970143z, 1998.

Atkinson, R., and Arey, J.: Atmospheric degradation of volatile organic compounds, Chem. Rev., 103(12), 4605–4638, https://doi.org/10.1021/cr0206420, 2003a.

Atkinson, R., and Arey, J.: Gas-phase tropospheric chemistry of biogenic volatile organic compounds: A review, Atmos. Environ., 37(2), 197–219, https://doi.org/10.1016/S1352-2310(03)00391-1, 2003b.

Atkinson, R., Aschmann, S. M., and Arey, J.: Rate constants for the gas-phase reactions of OH and NO_3 radicals and O_3 with sabinene and camphene at 296±2 K, Atmos, Environ. Part A, General Topics, 24(10), 2647–2654, https://doi.org/10.1016/0960-1686(90)90144-C, 1990.

Aumont, B., Szopa, S., and Madronich, S.: Modelling the evolution of organic carbon during its gas-phase tropospheric oxidation: development of an explicit model based on a

self generating approach, Atmos. Chem. Phys. Discuss., 5(1), 703–754, https://doi.org/10.5194/acpd-5-703-2005, 2005.

Aumont, B., Valorso, R., Mouchel-Vallon, C., Camredon, M., Lee-Taylor, J., and Madronich, S.: Modeling SOA formation from the oxidation of intermediate volatility n-alkanes, Atmos. Chem. Phys., 12(16), 7577–7589, https://doi.org/10.5194/acp-12-7577-2012, 2012.

Aumont, Bernard, Camredon, M., Mouchel-Vallon, C., La, S., Ouzebidour, F., Valorso, R., Lee-Taylor, J., and Madronich, S.: Modeling the influence of alkane molecular structure on secondary organic aerosol formation, Faraday Discuss., 165, 105–122, https://doi.org/10.1039/c3fd00029j, 2013.

Bäck, J., Aalto, J., Henriksson, M., Hakola, H., He, Q., and Boy, M.: Chemodiversity of a Scots pine stand and implications for terpene air concentrations, Biogeosciences, 9(2), 689–702, https://doi.org/10.5194/bg-9-689-2012, 2012.

Baruah, S. D., Gour, N. K., Sarma, P. J., and Deka, R. C.: OH-initiated mechanistic pathways and kinetics of camphene and fate of product radical: a DFT approach. Environ, Sci. Pollut. R., 25(3), 2147–2156, https://doi.org/10.1007/s11356-017-0646-2, 2018.

Boyd, C. M., Nah, T., Xu, L., Berkemeier, T., and Ng, N. L.: Secondary organic aerosol (SOA) from nitrate radical oxidation of monoterpenes: Effects of temperature, dilution, and humidity on aerosol formation, mixing, and evaporation, Environ. Sci. Tech., 51(14), 7831–7841, https://doi.org/10.1021/acs.est.7b01460, 2017.

Calogirou, A., Larsen, B. R., and Kotzias, D.: Gas-phase terpene oxidation products: A review, Atmos. Environ., 33(9), 1423–1439, https://doi.org/10.1016/S1352-2310(98)00277-5, 1999.

Camredon, M., Aumont, B., Lee-Taylor, J., and Madronich, S.: The SOA/VOC/NO_x system: An explicit model of secondary organic aerosol formation. Atmos. Chem. Phys., 7(21), 5599–5610, https://doi.org/10.5194/acp-7-5599-2007, 2007.

Carter, W. P. L.: Development of a condensed SAPRC-07 chemical mechanism, Atmos. Environ., 44(40), 5336–5345, https://doi.org/10.1016/j.atmosenv.2010.01.024, 2010.

Chen, F., Zhou, H., Gao, J., and Hopke, P. K.: A chamber study of secondary organic aerosol (SOA) formed by ozonolysis of d-limonene in the presence of NO, Aerosol and Air Quality Research, 17(1), 59–68, https://doi.org/10.4209/aaqr.2016.01.0029, 2017.

Chen, Q., Liu, Y., Donahue, N. M., Shilling, J. E., and Martin, S. T.: Particle-phase chemistry of secondary organic material: Modeled compared to measured O:C and H:C

elemental ratios provide constraints, Environ. Sci. Tech., 45(11), 4763–4770, https://doi.org/10.1021/es104398s, 2011.

Chhabra, P. S., Flagan, R. C., and Seinfeld, J. H.: Elemental analysis of chamber organic aerosol using an aerodyne high-resolution aerosol mass spectrometer, Atmos. Chem. Phys., 10(9), 4111–4131, https://doi.org/10.5194/acp-10-4111-2010, 2010.

Chhabra, P. S., Ng, N. L., Canagaratna, M. R., Corrigan, A. L., Russell, L. M., Worsnop, D. R., Flagan, R. C., and Seinfeld, J. H.: Elemental composition and oxidation of chamber organic aerosol, Atmos. Chem. Phys, 11, 8827–8845, https://doi.org/10.5194/acp-11-8827-2011, 2011.

Chuang, W. K., and Donahue, N. M.: A two-dimensional volatility basis set-Part 3: Prognostic modeling and NO_x dependence, Atmos. Chem. Phys., 16(1), 123–134, https://doi.org/10.5194/acp-16-123-2016, 2016.

Draper, D. C., Farmer, D. K., Desyaterik, Y., and Fry, J. L.: A qualitative comparison of secondary organic aerosol yields and composition from ozonolysis of monoterpenes at varying concentrations of NO_2, Atmos. Chem. Phys., 15(21), 12267–12281, https://doi.org/10.5194/acp-15-12267-2015, 2015.

Fehsenfeld, F., Calvert, J., Fall, R., Goldan, P., Guenther, A. B., Hewitt, C. N., Lamb, B., Liu, S., Trainer, M., Westberg, H., and Zimmerman, P.: Emissions of volatile organic compounds from vegetation and the implications for atmospheric chemistry, Global Biogeochem. Cy., 6(4), 389–430, https://doi.org/10.1029/92GB02125, 1992.

Fry, J. L., Draper, D. C., Barsanti, K. C., Smith, J. N., Ortega, J., Winkler, P. M., Lawler, M. J., Brown, S. S., Edwards, P. M., Cohen, R. C., and Lee, L.: Secondary organic aerosol formation and organic nitrate yield from NO_3 oxidation of biogenic hydrocarbons, Environ. Sci. Tech., 48(20), 11944–11953, https://doi.org/10.1021/es502204x, 2014.

Gaona-Colmán, E., Blanco, M. B., Barnes, I., Wiesen, P., and Teruel, M. A.: OH- and O_3-initiated atmospheric degradation of camphene: Temperature dependent rate coefficients, product yields and mechanisms, RSC Adv., 7(5), 2733–2744, https://doi.org/10.1039/c6ra26656h, 2017.

Geron, C., Rasmussen, R., Arnts, R. R., and Guenther, A.: A review and synthesis of monoterpene speciation from forests in the United States, Atmos. Environ., 34(11), 1761–1781, https://doi.org/10.1016/S1352-2310(99)00364-7, 2000.

Gilman, J. B., Lerner, B. M., Kuster, W. C., Goldan, P. D., Warneke, C., Veres, P. R., Roberts, J. M., de Gouw, J. A., Burling, I. R., and Yokelson, R. J.: Biomass burning emissions and potential air quality impacts of volatile organic compounds and other trace

gases from fuels common in the US, Atmos. Chem. Phys., 15(24), 13915–13938, https://doi.org/10.5194/acp-15-13915-2015, 2015.

Griffin, R. J., Cocker, D. R., Flagan, R. C., and Seinfeld, J. H.: Organic aerosol formation from the oxidation of biogenic hydrocarbons, J. Geophys. Res. Atmos., 104(D3), 3555–3567, https://doi.org/10.1029/1998JD100049, 1999.

Guenther, A., Hewitt, C. N., Erickson, D., Fall, R., Geron, C., Graedel, T., Harley, P., Klinger, L., Lerdau, M., Mckay, W. A., Pierce, T., Scholes, B., Steinbrecher, R., Tallamraju, R., Taylor, J., and Zimmerman, P.: A global model of natural volatile organic compound emission, J. Geophys. Res., 100(D5), 8873–8892, https://doi.org/10.1029/94JD02950, 1995.

Hakola, H., Arey, J., Aschmann, S. M., and Atkinson, R.: Product formation from the gas-phase reactions of OH radicals and O_3 with a series of monoterpenes, J. Atmos. Chem., 18(1), 75–102, https://doi.org/10.1007/BF00694375, 1994.

Hallquist, M., Wängberg, I., Ljungström, E., Barnes, I., and Becker, K. H.: Aerosol and product yields from NO_3 radical-initiated oxidation of selected monoterpenes, Environ. Sci. Tech., 33(4), 553–559, https://doi.org/10.1021/es980292s, 1999.

Hatch, L. E., Luo, W., Pankow, J. F., Yokelson, R. J., Stockwell, C. E., and Barsanti, K. C.: Identification and quantification of gaseous organic compounds emitted from biomass burning using two-dimensional gas chromatography-time-of-flight mass spectrometry, Atmos. Chem. Phys., 15(4), 1865–1899, https://doi.org/10.5194/acp-15-1865-2015, 2015.

Hatch, L. E., Jen, C. N., Kreisberg, N. M., Selimovic, V., Yokelson, R. J., Stamatis, C., York, R. A., Foster, D., Stephens, S. L., Goldstein, A. H., and Barsanti, K. C.: Highly speciated measurements of terpenoids emitted from laboratory and mixed-conifer forest prescribed fires, Environ. Sci. Tech., 53(16), 9418–9428, https://doi.org/10.1021/acs.est.9b02612, 2019.

Hatfield, M. L., and Huff Hartz, K. E.: Secondary organic aerosol from biogenic volatile organic compound mixtures, Atmos. Environ., 45(13), 2211–2219, https://doi.org/10.1016/j.atmosenv.2011.01.065, 2011.

Hayward, S., Muncey, R. J., James, A. E., Halsall, C. J., and Hewitt, C. N.: Monoterpene emissions from soil in a Sitka spruce forest, Atmos. Environ., 35(24), 4081–4087, https://doi.org/10.1016/S1352-2310(01)00213-8, 2001.

Heaton, K. J., Dreyfus, M. A., Wang, S., and Johnston, M. v.: Oligomers in the early stage of biogenic secondary organic aerosol formation and growth, Environ. Sci. Tech., 41(17), 6129–6136, https://doi.org/10.1021/es070314n, 2007.

Jacobson, M. C., Hansson, H. C., Noone, K. J., and Charlson, R. J.: Organic atmospheric aerosols: Review and state of the science, Rev. Geophys., 38(2), 267–294, https://doi.org/10.1029/1998RG000045, 2000.

Jang, M., and Kamens, R. M.: Newly characterized products and composition of secondary aerosols from the reaction of α-pinene with ozone, Atmos. Environ., 33(3), 459–474, https://doi.org/10.1016/S1352-2310(98)00222-2, 1999.

Kanakidou, M., Seinfeld, J. H., Pandis, S. N., Barnes, I., Dentener, F. J., Facchini, M. C., van Dingenen, R., Ervens, B., Nenes, A., Nielsen, C. J., Swietlicki, E., Putaud, J. P., Balkanski, Y., Fuzzi, S., Horth, J., Moortgat, G. K., Winterhalter, R., Myhre, C. E. L., Tsigaridis, K., Vignati, E., Stephanou, E. G., and Wilson, J.: Organic aerosol and global climate modelling: A review, Atmos. Chem. Phys. Discuss., 4(5), 5855–6024, https://doi.org/10.5194/acpd-4-5855-2004, 2004.

Kesselmeier, J., and Staudt, M.: Biogenic volatile organic compounds (VOC): An overview on emission, physiology and ecology, J. Atmos. Chem., 33(1), 23–88, https://doi.org/10.1023/A:1006127516791, 1999.

Kim, H., and Paulson, S. E.: Real refractive indices and volatility of secondary organic aerosol generated from photooxidation and ozonolysis of limonene, α-pinene and toluene, Atmos. Chem. Phys., 13(15), 7711–7723, https://doi.org/10.5194/acp-13-7711-2013, 2013.

Kim, S., Karl, T., Guenther, A., Tyndall, G., Orlando, J., Harley, P., Rasmussen, R., and Apel, E.: Emissions and ambient distributions of Biogenic Volatile Organic Compounds (BVOC) in a ponderosa pine ecosystem: Interpretation of PTR-MS mass spectra, Atmos. Chem. Phys., 10(4), 1759–1771, https://doi.org/10.5194/acp-10-1759-2010, 2010.

Kourtchev, I., Fuller, S. J., Giorio, C., Healy, R. M., Wilson, E., O'Connor, I., Wenger, J. C., McLeod, M., Aalto, J., Ruuskanen, T. M., Maenhaut, W., Jones, R., Venables, D. S., Sodeau, J. R., Kulmala, M., and Kalberer, M.: Molecular composition of biogenic secondary organic aerosols using ultrahigh-resolution mass spectrometry: Comparing laboratory and field studies, Atmos. Chem. Phys., 14(4), 2155–2167. https://doi.org/10.5194/acp-14-2155-2014, 2014.

Kourtchev, I., Doussin, J. F., Giorio, C., Mahon, B., Wilson, E. M., Maurin, N., Pangui, E., Venables, D. S., Wenger, J. C., and Kalberer, M.: Molecular composition of fresh and aged secondary organic aerosol from a mixture of biogenic volatile compounds: A high-resolution mass spectrometry study, Atmos. Chem. Phys., 15(10), 5683–5695, https://doi.org/10.5194/acp-15-5683-2015, 2015.

Kundu, S., Fisseha, R., Putman, A. L., Rahn, T. A., and Mazzoleni, L. R.: High molecular weight SOA formation during limonene ozonolysis: Insights from ultrahigh-resolution FT-

ICR mass spectrometry characterization, Atmos. Chem. Phys., 12(12), 5523–5536, https://doi.org/10.5194/acp-12-5523-2012, 2012.

La, Y. S., Camredon, M., Ziemann, P. J., Valorso, R., Matsunaga, A., Lannuque, V., Lee-Taylor, J., Hodzic, A., Madronich, S., and Aumont, B.: Impact of chamber wall loss of gaseous organic compounds on secondary organic aerosol formation: Explicit modeling of SOA formation from alkane and alkene oxidation, Atmos. Chem. Phys., 16(3), 1417–1431, https://doi.org/10.5194/acp-16-1417-2016, 2016.

Lambe, A. T., Chhabra, P. S., Onasch, T. B., Brune, W. H., Hunter, J. F., Kroll, J. H., Cummings, M. J., Brogan, J. F., Parmar, Y., Worsnop, D. R., Kolb, C. E., and Davidovits, P.: Effect of oxidant concentration, exposure time, and seed particles on secondary organic aerosol chemical composition and yield, Atmos. Chem. Phys., 15(6), 3063–3075, https://doi.org/10.5194/acp-15-3063-2015, 2015.

Larsen, B. R., di Bella, D., Glasius, M., Winterhalter, R., Jensen, N. R., and Hjorth, J.: Gas-phase OH oxidation of monoterpenes: Gaseous and particulate products, J. Atmos. Chem., 38(3), 231–276, https://doi.org/10.1023/A:1006487530903, 2001.

Lee, A., Goldstein, A. H., Keywood, M. D., Gao, S., Varutbangkul, V., Bahreini, R., Ng, N. L., Flagan, R. C., and Seinfeld, J. H.: Gas-phase products and secondary aerosol yields from the ozonolysis of ten different terpenes, J. Geophys. Res. Atmos., 111, D07302. https://doi.org/10.1029/2005JD006437, 2006a.

Lee, A., Goldstein, A. H., Kroll, J. H., Ng, N. L., Varutbangkul, V., Flagan, R. C., and Seinfeld, J. H.: Gas-phase products and secondary aerosol yields from the photooxidation of 16 different terpenes, J. Geophys. Res. Atmos., 111, D17305, https://doi.org/10.1029/2006JD007050, 2006b.

Ludley, Katherine. E., Jickells, S. M., Chamberlain, P. M., Whitaker, J., and Robinson, C. H.: Distribution of monoterpenes between organic resources in upper soil horizons under monocultures of Picea abies, Picea sitchensis and Pinus Sylvestris, Soil Biol. Biochem., 41(6), 1050–1059, https://doi.org/10.1016/J.SOILBIO.2009.02.002, 2009.

Maleknia, S. D., Bell, T. L., and Adams, M. A.: PTR-MS analysis of reference and plant-emitted volatile organic compounds, Int. J. Mass Spectrom., 262(3), 203–210, https://doi.org/10.1016/j.ijms.2006.11.010, 2007.

McVay, R. C., Zhang, X., Aumont, B., Valorso, R., Camredon, M., La, Y. S., Wennberg, P. O., and Seinfeld, J. H.: SOA formation from the photooxidation of α-pinene: Systematic exploration of the simulation of chamber data, Atmos. Chem. Phys., 16(5), 2785–2802, https://doi.org/10.5194/acp-16-2785-2016, 2016.

Nah, T., McVay, R. C., Zhang, X., Boyd, C. M., Seinfeld, J. H., and Ng, N. L.: Influence of seed aerosol surface area and oxidation rate on vapor wall deposition and SOA mass yields: A case study with α-pinene ozonolysis, Atmos. Chem. Phys., 16(14), 9361–9379, https://doi.org/10.5194/acp-16-9361-2016, 2016.

Nannoolal, Y., Rarey, J., and Ramjugernath, D.: Estimation of pure component properties part 3. Estimation of the vapor pressure of non-electrolyte organic compounds via group contribution and group interactions, Fluid Phase Equilibr., 269(1–2), 117–133, https://doi.org/10.1016/j.fluid.2008.04.020, 2008.

Ng, N. L., Chhabra, P. S., Chan, A. W. H., Surratt, J. D., Kroll, J. H., Kwan, A. J., McCabe, D. C., Wennberg, P. O., Sorooshian, A., Murphy, S. M., Dalleska, N. F., Flagan, R. C., and Seinfeld, J. H.: Effect of NO_x level on secondary organic aerosol (SOA) formation from the photooxidation of terpenes, Atmos. Chem. Phys., 7(19), 5159–5174, https://doi.org/10.5194/acp-7-5159-2007, 2007.

Pathak, R. K., Presto, A. A., Lane, T. E., Stanier, C. O., Donahue, N. M., and Pandis, S. N.: Ozonolysis of α-pinene: Parameterization of secondary organic aerosol mass fraction, Atmos. Chem. Phys., 7(14), 3811–3821, https://doi.org/10.5194/acp-7-3811-2007, 2007a.

Pathak, R. K., Stanier, C. O., Donahue, N. M., and Pandis, S. N.: Ozonolysis of α-pinene at atmospherically relevant concentrations: Temperature dependence of aerosol mass fractions (yields), J. Geophys. Res. Atmos., 112(3), 1–8, https://doi.org/10.1029/2006JD007436, 2007b.

Pfaffenberger, L., Barmet, P., Slowik, J. G., Praplan, A. P., Dommen, J., Prévôt, A. S. H., and Baltensperger, U.: The link between organic aerosol mass loading and degree of oxygenation: An α-pinene photooxidation study, Atmos. Chem. Phys., 13(13), 6493–6506, https://doi.org/10.5194/acp-13-6493-2013, 2013.

Presto, A. A., Huff Hartz, K. E., and Donahue, N. M.: Secondary organic aerosol production from terpene ozonolysis. 2. Effect of NO_x concentration, Environ. Sci. Tech., 39, 7046–7054, https://doi.org/10.1021/es050400s, 2005.

Presto, A. A., and Donahue, N. M.: Investigation of α-pinene + ozone secondary organic aerosol formation at low total aerosol mass, Environ. Sci. Tech., 40(11), 3536–3543, https://doi.org/10.1021/es052203z, 2006.

Reinhardt, A., Emmenegger, C., Gerrits, B., Panse, C., Dommen, J., Baltensperger, U., Zenobi, R., and Kalberer, M.: Ultrahigh mass resolution and accurate mass measurements as a tool to characterize oligomers in secondary organic aerosols, Anal. Chem., 79(11), 4074–4082, https://doi.org/10.1021/ac062425v, 2007.

Reissell, A., Harry, C., Aschmann, S. M., Atkinson, R., and Arey, J.: Formation of acetone from the OH radical- and O_3-initiated reactions of a series of monoterpenes, J. Geophys. Res. Atmos., 104(D11), 13869–13879, https://doi.org/10.1029/1999JD900198, 1999.

Rinne, J., Tuovinen, J. P., Laurila, T., Hakola, H., Aurela, M., and Hypén, H.: Measurements of hydrocarbon fluxes by a gradient method above a northern boreal forest, Agr. Forest Meteorol., 102(1), 25–37, https://doi.org/10.1016/S0168-1923(00)00088-5, 2000.

Saha, P. K., and Grieshop, A. P.: Exploring divergent volatility properties from yield and thermodenuder measurements of secondary organic aerosol from α-pinene ozonolysis, Environ. Sci. Tech., 50(11), 5740–5749, https://doi.org/10.1021/acs.est.6b00303, 2016.

Shilling, J. E., Chen, Q., King, S. M., Rosenoern, T., Kroll, J. H., R.Worsnop, D., DeCarlo, P. F., Aiken, A. C., Sueper, D., Jimenez, J. L., and Martin, S. T.: Loading-dependent elemental composition of α-pinene SOA particles, Atmos. Chem. Phys., 9(3), 771–782, https://doi.org/10.5194/acp-9-771-2009, 2009.

Simpson, I. J., Akagi, S. K., Barletta, B., Blake, N. J., Choi, Y., Diskin, G. S., Fried, A., Fuelberg, H. E., Meinardi, S., Rowland, F. S., Vay, S. A., Weinheimer, A. J., Wennberg, P. O., Wiebring, P., Wisthaler, A., Yang, M., Yokelson, R. J., and Blake, D. R.: Boreal forest fire emissions in fresh Canadian smoke plumes: C1-C10 volatile organic compounds (VOCs), CO2, CO, NO2, NO, HCN and CH3CN, Atmos. Chem. Phys., 11(13), 6445–6463, https://doi.org/10.5194/acp-11-6445-2011, 2011.

Steinbrecher, R., Hauff, K., Rössler, J., Dürr, M., and Seufert, G.: Monoterpene emission from soils in orange plantations of the Valencian Citrus belt, Spain, Physics and Chemistry of the Earth, Part B: Hydrology, Oceans and Atmosphere, 24(6), 695–698, https://doi.org/10.1016/S1464-1909(99)00067-2, 1999.

Stockwell, W. R., Kirchner, F., Kuhn, M., and Seefeld, S.: A new mechanism for regional atmospheric chemistry modeling, J. Geophys. Res. Atmos., 102(D22), 25847–25879, https://doi.org/10.1029/97jd00849, 1997.

Tani, A., Hayward, S., and Hewitt, C. N.: Measurement of monoterpenes and related compounds by proton transfer reaction-mass spectrometry (PTR-MS), Int. J. Mass Spectrom., 223–224, 561–578, https://doi.org/10.1016/S1387-3806(02)00880-1, 2003.

Valorso, R., Aumont, B., Camredon, M., Raventos-Duran, T., Mouchel-Vallon, C., Ng, N. L., Seinfeld, J. H., Lee-Taylor, J., and Madronich, S.: Explicit modelling of SOA formation from α-pinene photooxidation: Sensitivity to vapour pressure estimation, Atmos. Chem. Phys., 11(14), 6895–6910, https://doi.org/10.5194/acp-11-6895-2011, 2011.

Walser, M. L., Desyaterik, Y., Laskin, J., Laskin, A., and Nizkorodov, S. A.: High-resolution mass spectrometric analysis of secondary organic aerosol produced by ozonation of limonene, Phys. Chem. Chem. Phys., 10(7), 1009–1022, https://doi.org/10.1039/b712620d, 2008.

White, M. L., Russo, R. S., Zhou, Y., Mao, H., Varner, R. K., Ambrose, J., Veres, P., Wingenter, O. W., Haase, K., Stutz, J., Talbot, R., and Sive, B. C.: Volatile organic compounds in northern New England marine and continental environments during the ICARTT 2004 campaign, J. Geophys. Res. Atmos., 113(8), 1–16, https://doi.org/10.1029/2007JD009161, 2008.

Wisthaler, A., Jensen, N. R., Winterhalter, R., Lindinger, W., and Hjorth, J.: Measurements of acetone and other gas phase product yields from the OH-initiated oxidation of terpenes by proton-transfer-reaction mass spectrometry (PTR-MS), Atmos. Environ., 35(35), 6181–6191, https://doi.org/10.1016/S1352-2310(01)00385-5, 2001.

Yáñez-Serrano, A. M., Nölscher, A. C., Bourtsoukidis, E., Gomes Alves, E., Ganzeveld, L., Bonn, B., Wolff, S., Sa, M., Yamasoe, M., Williams, J., Andreae, M. O., and Kesselmeier, J.: Monoterpene chemical speciation in a tropical rainforest: Variation with season, height, and time of day at the Amazon Tall Tower Observatory (ATTO), Atmos. Chem. Phys., 18(5), 3403–3418, https://doi.org/10.5194/acp-18-3403-2018, 2018.

Yassaa, N., Peeken, I., Zllner, E., Bluhm, K., Arnold, S., Spracklen, D., and Williams, J.: Evidence for marine production of monoterpenes, Environ. Chem., 5(6), 391–401, https://doi.org/10.1071/EN08047, 2008.

Yu, J., Cocker III, D. R., Griffin, R. J., Flagan, R. C., and Seinfeld, J. H.: Gas-Phase Ozone Oxidation of Monoterpenes: Gaseous and Particulate Products, J. Atmos. Chem., 34(2), 207–258, https://doi.org/10.1023/A:1006254930583, 1999.

Zhang, J., Huff Hartz, K. E., Pandis, S. N., and Donahue, N. M.: Secondary organic aerosol formation from limonene Ozonolysis: Homogeneous and heterogeneous influences as a function of NO_x, J. Phys. Chem. A., 110(38), 11053–11063, https://doi.org/10.1021/jp062836f, 2006.

Zhang, X, McVay, R. C., Huang, D. D., Dalleska, N. F., Aumont, B., Flagan, R. C., and Seinfeld, J. H.: Formation and evolution of molecular products in alpha-pinene secondary organic aerosol, P. Natl. Aca. Sci. USA, 112(46), 14168–14173, https://doi.org/10.1073/pnas.1517742112, 2015.

Zhao, D., Schmitt, S. H., Wang, M., Acir, I. H., Tillmann, R., Tan, Z., Novelli, A., Fuchs, H., Pullinen, I., Wegener, R., Rohrer, F., Wildt, J., Kiendler-Scharr, A., Wahner, A., and Mentel, T. F.: Effects of NO_x and SO_2 on the secondary organic aerosol formation from

photooxidation of α-pinene and limonene, Atmos. Chem. Phys., 18(3), 1611–1628, https://doi.org/10.5194/acp-18-1611-2018, 2018.

Appendix A

Table A1: SOA data compiled from published chamber studies for photooxidation and ozonolysis of α-pinene and limonene.

Condition	T (K)	$[O_3]_o$ (ppb)	NO_x (ppb)	$[HC]_o$ (ppb)	ΔHC (μg m^{-3})	SOA mass (μg m^{-3})	SOA yield	Reference
α-Pinene photooxidation	312-306		230	150	804.6	44.0	0.06	Kim and Paulson (2013)
α-Pinene photooxidation	310-312-306		110	152	788.8	103.0	0.14	Kim and Paulson (2013)
α-Pinene photooxidation	306-309		50	142	743.9	107.0	0.16	Kim and Paulson (2013)
α-Pinene photooxidation	312-319-315		47	153	683.0	118.0	0.17	Kim and Paulson (2013)
α-Pinene photooxidation	300			51	260.0	46.0	0.18	Mcvay et al. (2016)
α-Pinene photooxidation	300			56	280.0	65.0	0.23	Mcvay et al. (2016)
α-Pinene photooxidation	300			53	240.0	52.0	0.22	Mcvay et al. (2016)
α-Pinene photooxidation	298			51	268.0	72.0	0.27	Mcvay et al. (2016)
α-Pinene photooxidation	297			53	205.0	35.0	0.17	Mcvay et al. (2016)
α-Pinene photooxidation	297			49	195.0	47.0	0.24	Mcvay et al. (2016)
α-Pinene photooxidation	293				616.6	199.0	0.32	Lee et al. (2006b)
α-Pinene photooxidation	298		0		76.8	29.3	0.38	Ng et al. (2007)
α-Pinene photooxidation	298		1		264.2	121.3	0.46	Ng et al. (2007)
α-Pinene photooxidation	296		198		73.4	15.6	0.21	Ng et al. (2007)

α-Pinene photooxidation	299		938		69.8	4.5	0.06	Ng et al. (2007)
α-Pinene photooxidation	298		968		259.2	40.8	0.16	Ng et al. (2007)
α-Pinene photooxidation			0		259.9	63.9	0.25	Chhabra et al. (2011)
α-Pinene photooxidation			400		265.6	53.7	0.20	Chhabra et al. (2011)
Limonene photooxidation	310-305		300	208	1110.4	96-287	0.35	Kim and Paulson (2013)
Limonene photooxidation	309-313		98	140	735.5	34-195	0.35	Kim and Paulson (2013)
Limonene photooxidation	297-299		120	157	801.0	32-214	0.37	Kim and Paulson (2013)
Limonene photooxidation	311-315		41	130	680.0	11-219	0.43	Kim and Paulson (2013)
Limonene photooxidation	308-312-307		39	130	690.6	14-275	0.47	Kim and Paulson (2013)
Limonene photooxidation	313.4		105		109.0	9.5	0.09	Griffin et al. (1999)
Limonene photooxidation	313.4		80.2		186.2	49.6	0.27	Griffin et al. (1999)
Limonene photooxidation	309.4		139		265.2	79.1	0.30	Griffin et al. (1999)
Limonene photooxidation	309.4		140		348.8	120.2	0.34	Griffin et al. (1999)
Limonene photooxidation	294				676.5	394.0	0.58	Lee et al. (2006b)
α-Pinene ozonolysis	299-300	500		143	592.2	28-230	0.46	Kim and Paulson (2013)
α-Pinene ozonolysis	296-299	500		150	724.3	39-271	0.44	Kim and Paulson (2013)
α-Pinene ozonolysis	296-301	500		170	866.2	37-271	0.40	Kim and Paulson (2013)

α-Pinene ozonolysis	296-295	500	160	897.5	71-349	0.45	Kim and Paulson (2013)
α-Pinene ozonolysis	291-293	500	126	669.8	34-215	0.39	Kim and Paulson (2013)
α-Pinene ozonolysis		200	49.5	282.0	42.3	0.15	Kourtchev et al. (2014)
α-Pinene ozonolysis		200	50.5	312.5	50.0	0.16	Kourtchev et al. (2014)
α-Pinene ozonolysis		200	55.2	349.4	55.9	0.16	Kourtchev et al. (2014)
α-Pinene ozonolysis	298	100	290.2 ±23.2	278.1	62.0 ±1.2	0.23	Nah et al. (2016)
α-Pinene ozonolysis	298	100	280.5 ±22.4	267.0	63.0 ±0.8	0.23	Nah et al. (2016)
α-Pinene ozonolysis	298	100	238.7 ±19.1	222.5	50.6 ±1.6	0.23	Nah et al. (2016)
α-Pinene ozonolysis	298	500	274 ±21.9	278.1	87.3 ±0.3	0.32	Nah et al. (2016)
α-Pinene ozonolysis	298	500	264 ±21.2	261.4	75.7 ±0.6	0.29	Nah et al. (2016)
α-Pinene ozonolysis	298	500	236.1 ±18.9	239.2	66.3 ±1.9	0.28	Nah et al. (2016)
α-Pinene ozonolysis	309.9			89.3	7.4	0.08	Griffin et al. (1999)
α-Pinene ozonolysis	309.9			97.3	8.5	0.09	Griffin et al. (1999)
α-Pinene ozonolysis	303.3			169.4	30.3	0.18	Griffin et al. (1999)
α-Pinene ozonolysis	303.3			248.7	46.0	0.18	Griffin et al. (1999)
α-Pinene ozonolysis	308			306.7	52.3	0.17	Griffin et al. (1999)
α-Pinene ozonolysis	308			349.8	65.1	0.19	Griffin et al. (1999)

α-Pinene ozonolysis	308	237		59.2	306.7	54.2	0.18	Yu et al. (1999)
α-Pinene ozonolysis	308	269		67.2	350.3	65.1	0.19	Yu et al. (1999)
α-Pinene ozonolysis	306	74		107.1	244.3	38.8	0.16	Yu et al. (1999)
α-Pinene ozonolysis	293				1052.2	417.0	0.41	Lee et al. (2006a)
α-Pinene ozonolysis	298.15±1 2	300			126.8	35.6	0.28	Chen et al. (2011)
α-Pinene ozonolysis	298.15±1 3	300			11.7	1.2	0.10	Chen et al. (2011)
α-Pinene ozonolysis	298.15±1 4	300			15.6	1.9	0.12	Chen et al. (2011)
α-Pinene ozonolysis	298.15±1 5	300			78.9	15.4	0.20	Chen et al. (2011)
α-Pinene ozonolysis	298.15±1 6	300			506.5	95.2	0.19	Chen et al. (2011)
α-Pinene ozonolysis	298.15±1 7	300			506.5	138.0	0.27	Chen et al. (2011)
α-Pinene ozonolysis	298.15±1 8	300			36.7	7.0	0.19	Chen et al. (2011)
α-Pinene ozonolysis	298.15±1 9	300			5.0	0.5	0.10	Chen et al. (2011)
α-Pinene ozonolysis			0		278.1	62.0	0.22	Chhabra et al. (2011)
Limonene ozonolysis	298-300	500		167	925.8	579.0	0.78	Kim and Paulson (2013)
Limonene ozonolysis	293-295	500		198	1116.3	614.0	0.72	Kim and Paulson (2013)
Limonene ozonolysis	294-296	500		150	842.8	454.0	0.72	Kim and Paulson (2013)
Limonene ozonolysis	295-296	69.7	33.7	154	257.0	135.7	0.49	Chen et al. (2017)

Limonene ozonolysis	295-296	71	35.2	150	269.0	137.2	0.51	Chen et al. (2017)
Limonene ozonolysis	295-297	72.1	58.9	158	220.0	156.5	0.73	Chen et al. (2017)
Limonene ozonolysis	296-297	70.3	62.4	153	228.0	157.3	0.72	Chen et al. (2017)
Limonene ozonolysis	296-297	1.1	67.1	155	144.0	30.3	0.27	Chen et al. (2017)
Limonene ozonolysis	295-296	0.9	68.2	159	138.0	31.8	0.30	Chen et al. (2017)

Table A2: Normalized emission factor (EF) for model surrogates representing top five monoterpenes (by EF) from black spruce, Douglas fir, and lodgepole pine (Hatch et al., 2015, 2017). In Assignment 1, α-pinene is used to represent all monoterpenes except limonene. In Assignment 2, camphene is represented as 50 % α-pinene and 50 % limonene. EFs of assignments 1 and 2 for lodgepole pine are the same, because camphene is not one of the top five monoterpenes by EF.

	Black Spruce		**Douglas Fir**		**Lodgepole Pine**	
	$EF_{\alpha pin}$	EF_{lim}	$EF_{\alpha pin}$	EF_{lim}	$EF_{\alpha pin}$	EF_{lim}
Assignment 1	0.81	0.19	0.8	0.2	0.86	0.14
Assignment 2	0.62	0.38	0.6	0.4	0.86	0.14

Table A3: Two-product SOA yield parameters for α-pinene and limonene based on Griffin et al. (1999).

	2-product			
	α_1	α_2	C^*_1	C^*_2
α-pinene	0.038	0.326	5.8	250.0
limonene	0.239	0.363	18.2	188.7

Table A4: Volatility basis set (VBS) parameters (low NO_x, dry) based on Pathak et al. (2007b) (for α-pinene) and Zhang et al. (2006) (for limonene).

	VBS (low NO_x)				
C*	0	1	10	100	1000
α-pinene	-	0.07	0.038	0.179	0.3
limonene	0.03	0.29	0.31	0.3	0.6

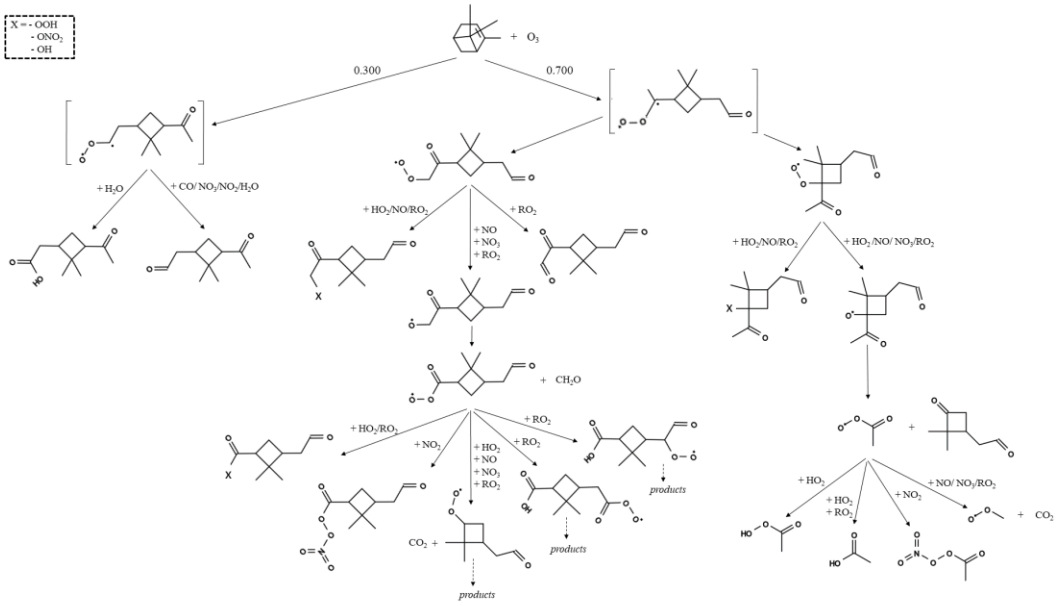

Figure A1: Initial oxidation pathways of α-pinene with O_3 as represented in GECKO-A.

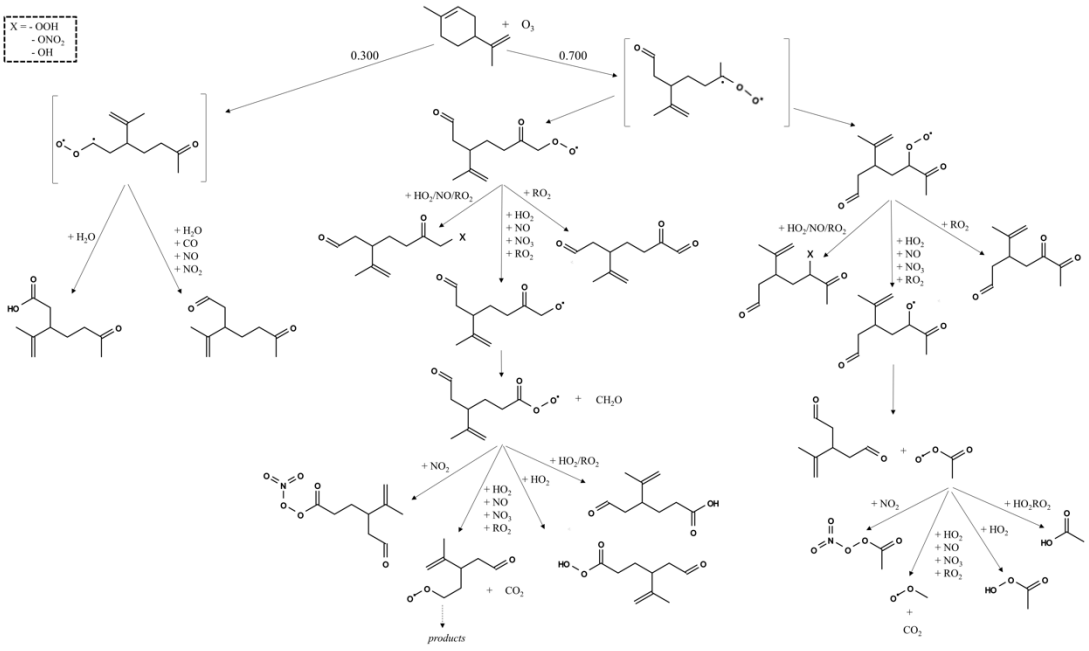

Figure A2: Initial oxidation pathways of limonene with O_3 as represented in GECKO-A.

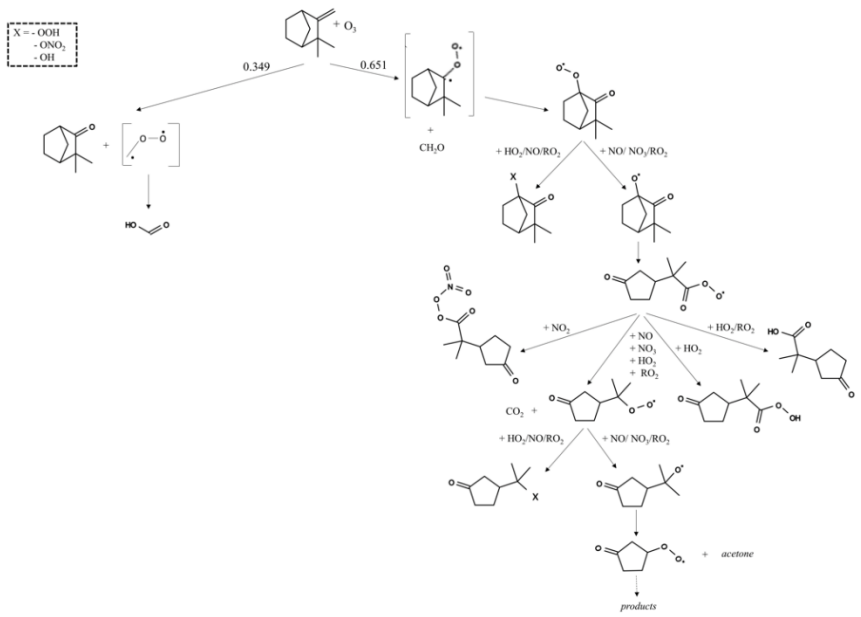

Figure A3: Initial oxidation pathways of camphene with O_3 as represented in GECKO-A.

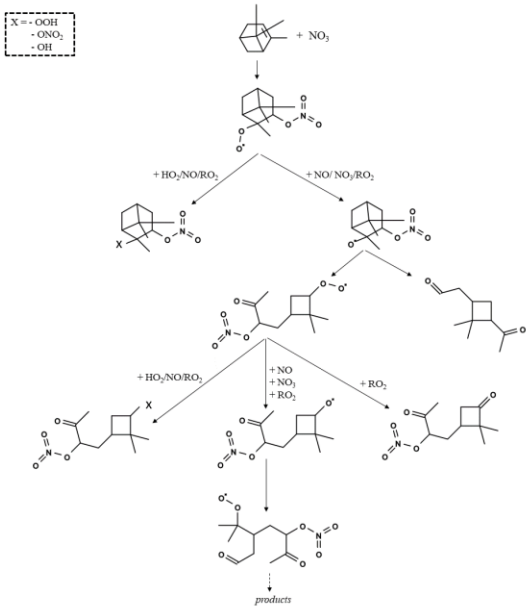

Figure A4: Initial oxidation pathways of α-pinene with NO_3 as represented in GECKO-A.

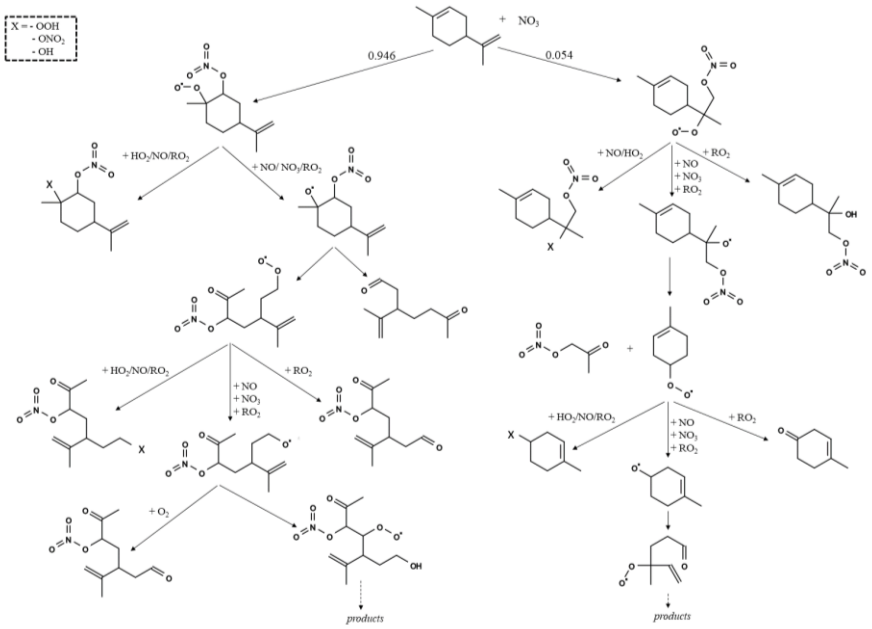

Figure A5: Initial oxidation pathways of limonene with NO_3 as represented in GECKO-A.

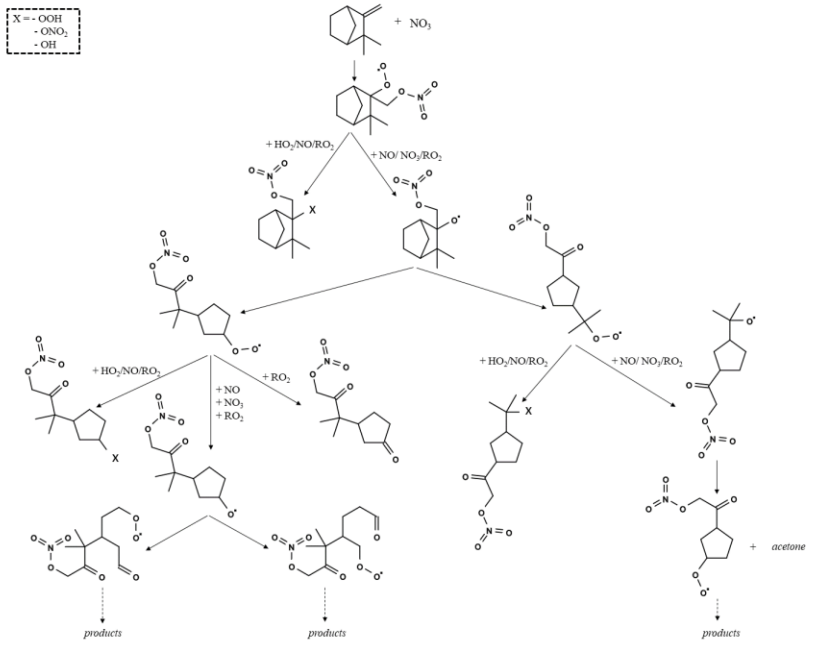

Figure A6: Initial oxidation pathways of camphene with NO_3 as represented in GECKO-A.

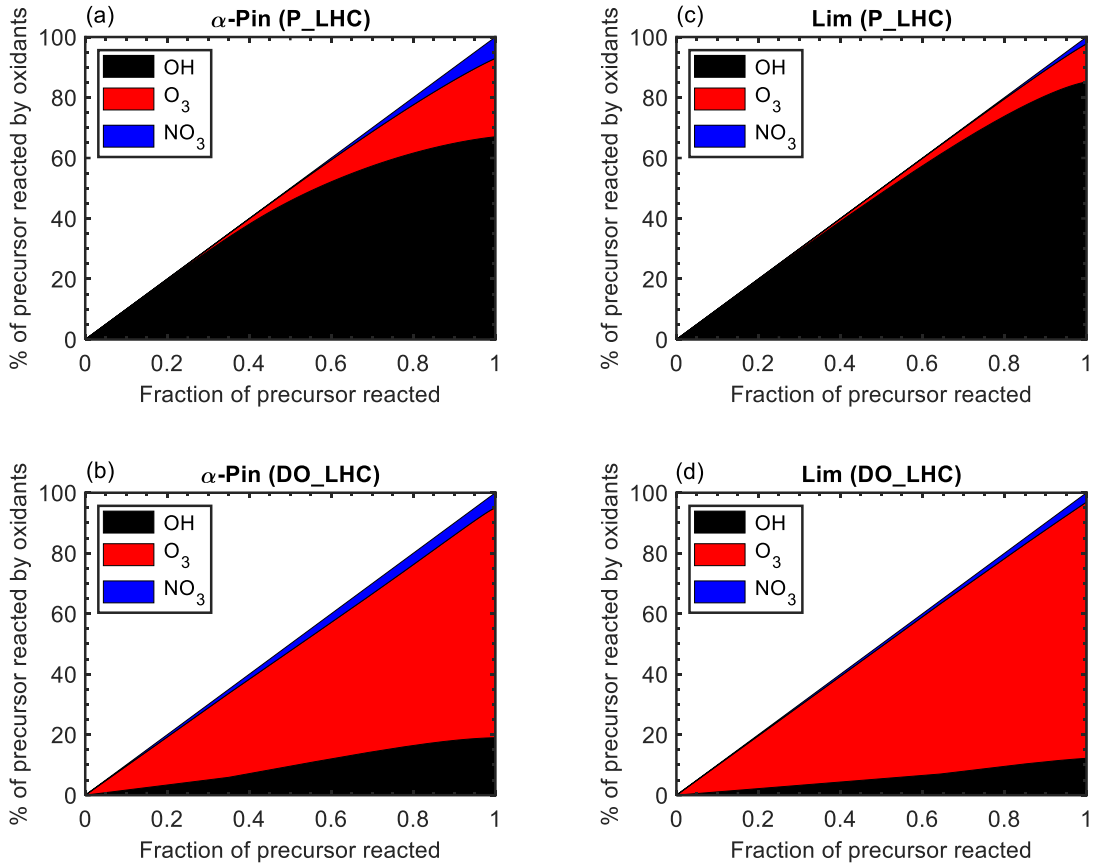

Figure A7: Percentage of precursor consumed by OH (black), O_3 (red), and NO_3 (blue) as a function of fraction of precursor reacted for α-pinene and limonene under photooxidation and ozonolysis (for lower initial precursor mixing ratio of 50 ppb).

Figure A7 shows the percentage of the simulated precursor consumption by the three main oxidants: hydroxyl radical (OH), ozone (O_3), and nitrate radical (NO_3). Under photooxidation, both α-pinene and limonene initially react predominantly with OH. As the reaction progresses (after ~ 30 % of the precursor is reacted), removal of the precursor by O_3 and NO_3 begins to grow until the precursor is completely reacted. The results in Fig. S7a indicate that ~67 % of α-pinene is removed by OH, 25 % by O_3, and ~8 % by NO_3; similarly, as shown in Fig. S7c 85% of limonene is removed by OH, 12% by O_3 and 3 % by NO_3 during photooxidation. For α-pinene ozonolysis, the consumption is largely by O_3 (~75 %) and OH(~20 %), to a lesser extent by NO_3; (~5 %); for limonene, consumption is dominated by O_3 (~85 %), followed by OH (~10 %), and NO_3 (~5 %). Unlike in many

chamber experiments, there is no OH scrubber in the simulations. Also, as NO_3 is formed by reaction of O_3 with NO_2 during the dark ozonolysis simulation, a small percentage of the precursor reacts with NO_3 since no light is available to photolyze the NO_3.

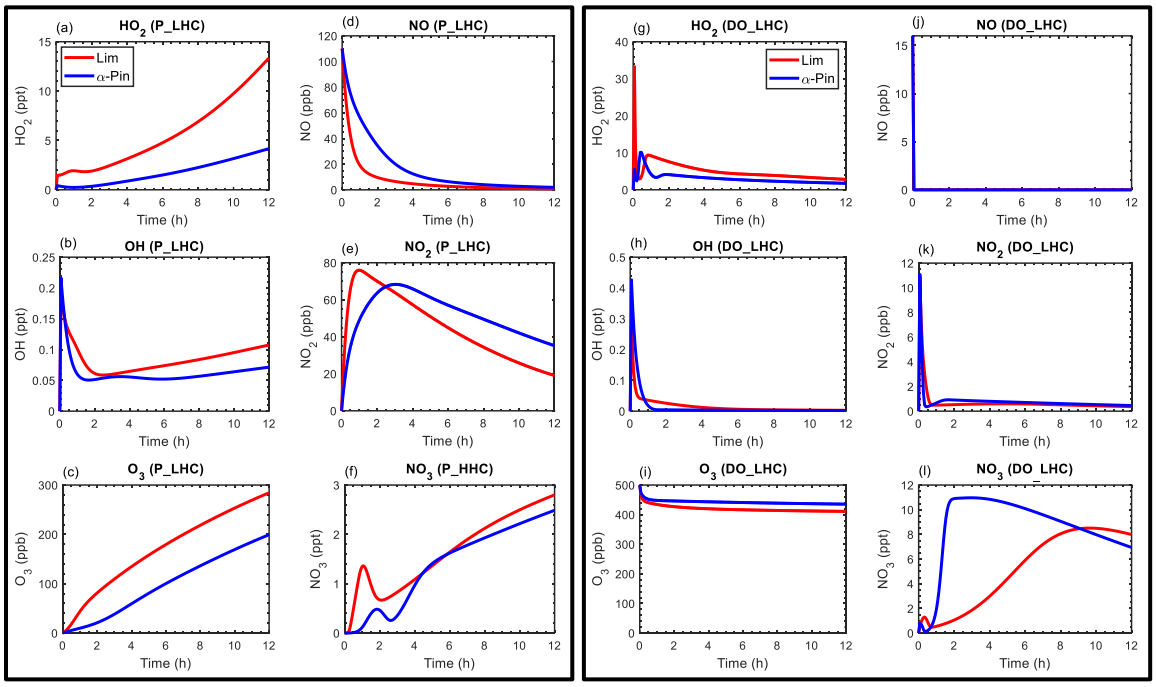

Figure A8: The mixing ratios of HO_2, OH, O_3, NO, NO_2, and NO_3 as a function of time for α-pinene (blue line) and limonene (red line) (with the low initial hydrocarbon (LHC) mixing ratio of 50 ppb) during photooxidation (P) and dark ozonolysis (DO) simulations.

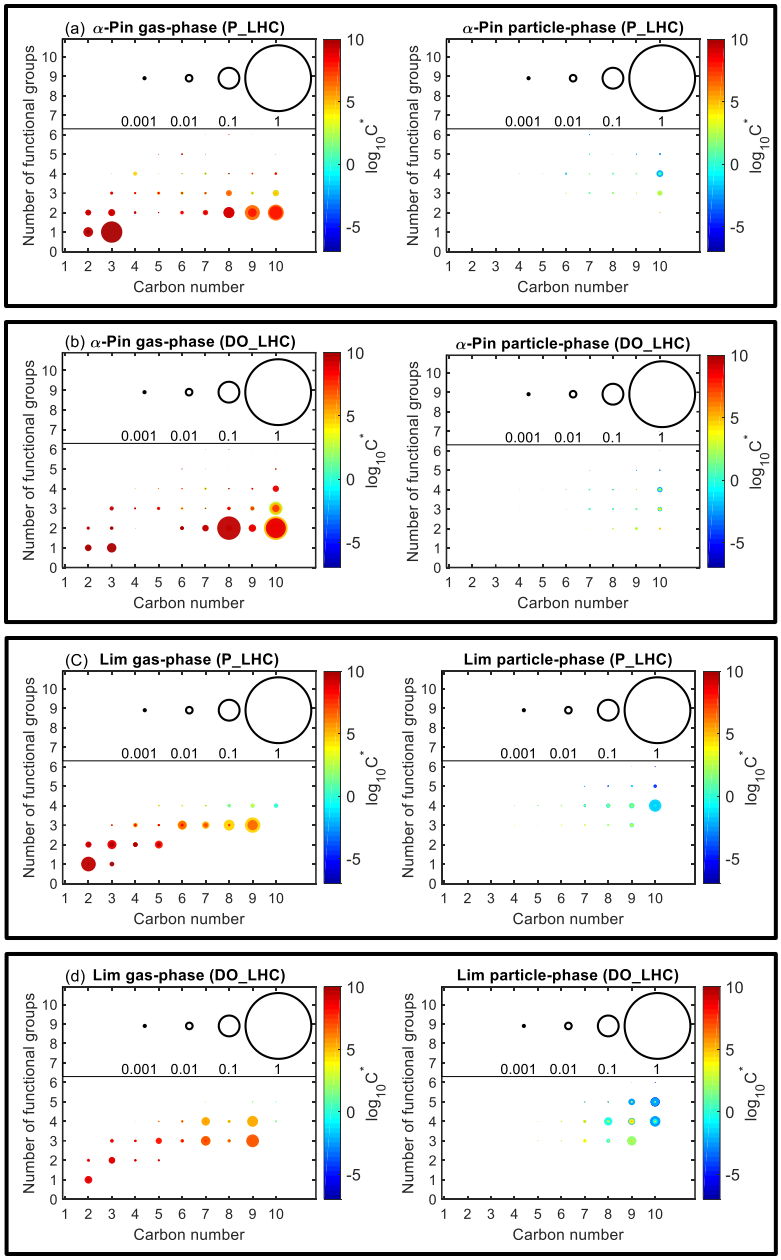

Figure A9: Number of functional groups associated with gas- and particle-phase species as a function of carbon number. Results are shown for camphene, α-pinene, and limonene after 12 hours of oxidation under photooxidation (P) and dark ozonolysis (DO) with lower hydrocarbon (LHC) mixing ratio of 50 ppb. The markers are sized by the ratio of their mixing ratio (in ppbC) to the initial mixing ratio of the precursor (in ppbC). The colors of the markers are scaled by volatility (represented by saturation concentration, C*).

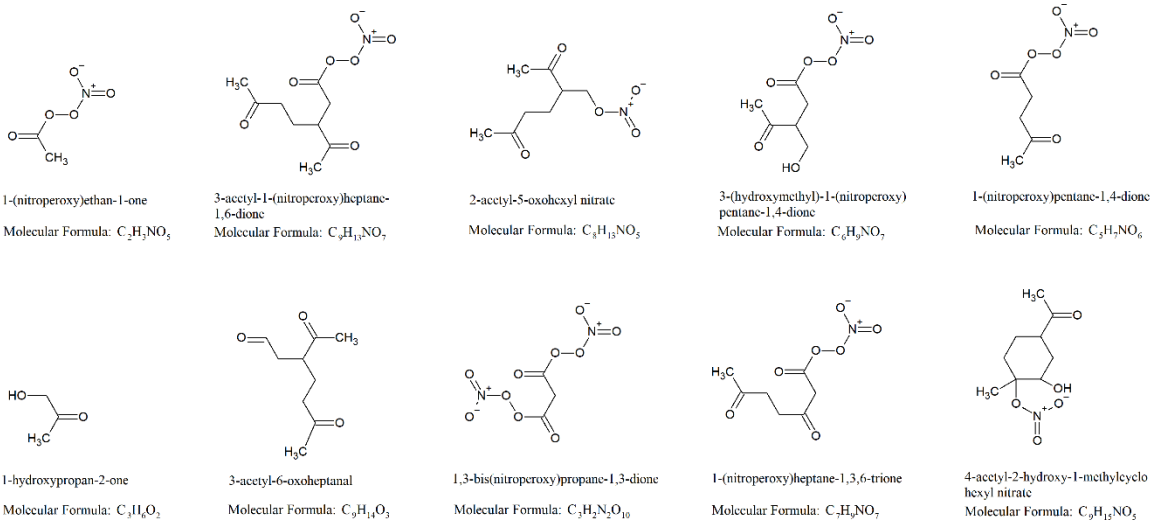

Figure A10: Top 10 gas-phase products from limonene photooxidation low hydrocarbon (P_LHC) simulation.

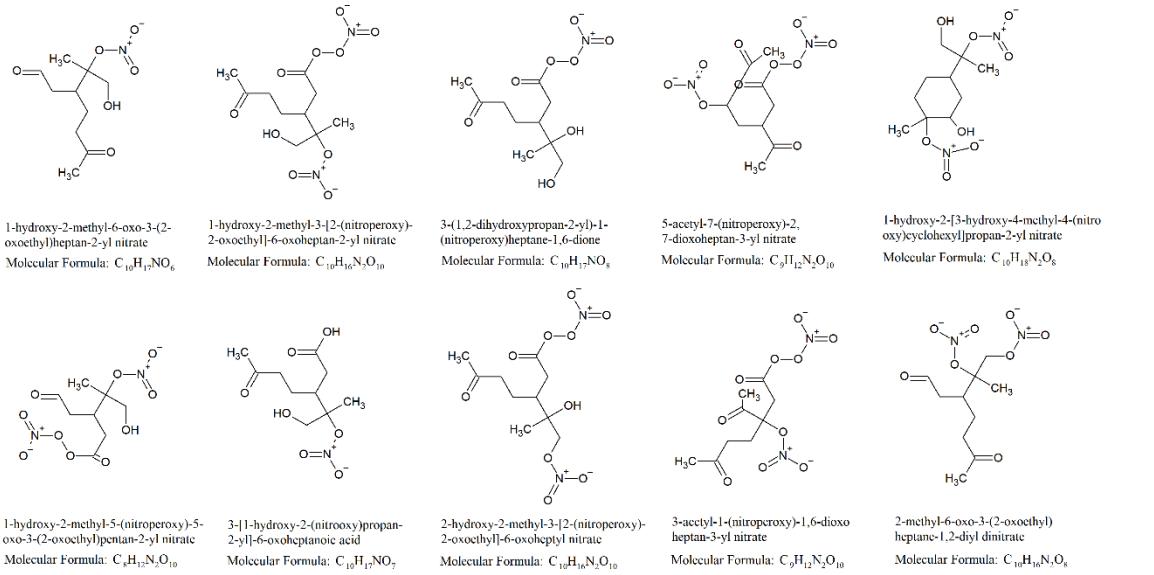

Figure A11: Top 10 particle-phase products from limonene photooxidation low hydrocarbon (P_LHC) simulation.

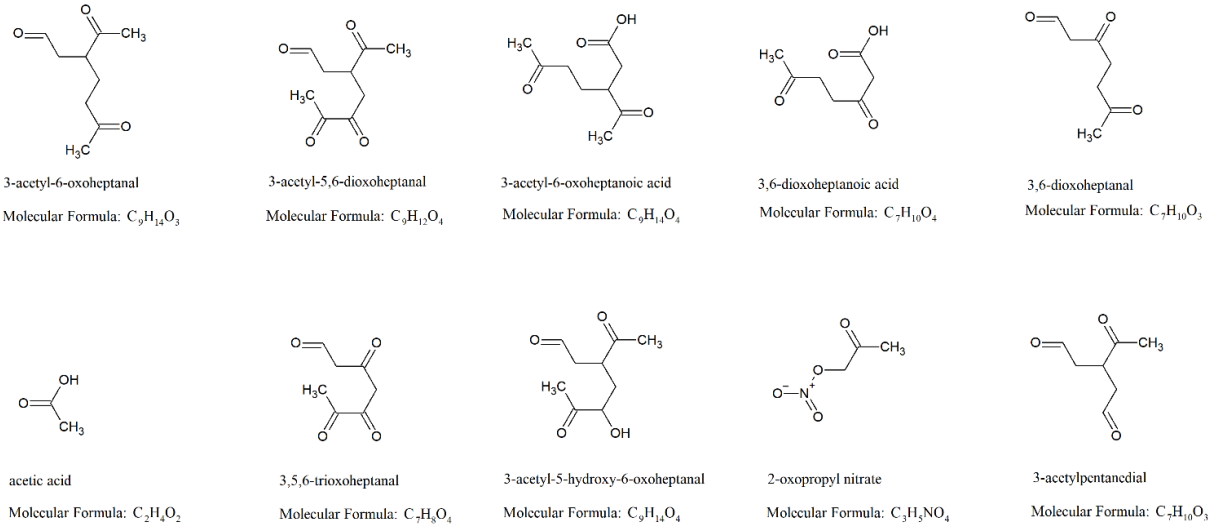

Figure A12: Top 10 gas-phase products from limonene dark ozonolysis low hydrocarbon (DO_LHC) simulation.

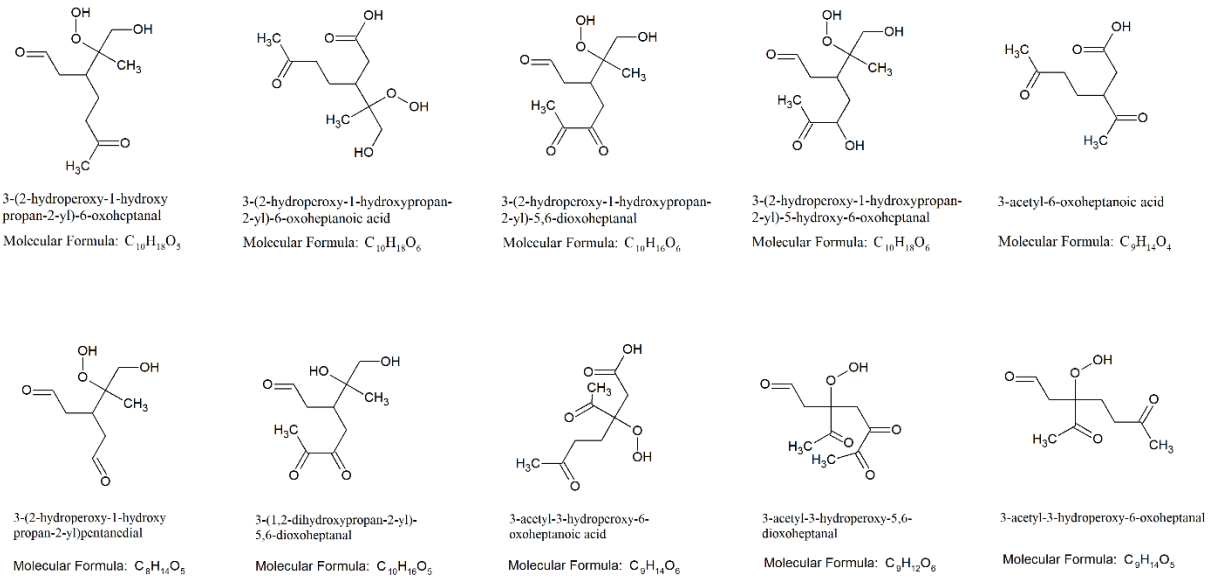

Figure A13: Top 10 particle-phase products from limonene dark ozonolysis low hydrocarbon (DO_LHC) simulation.

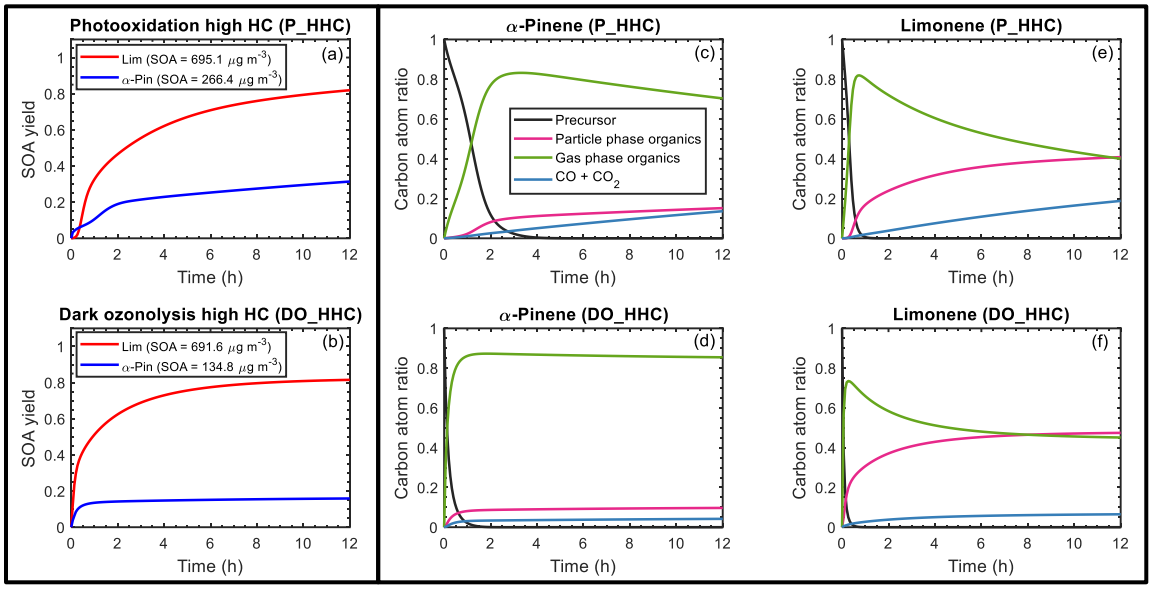

Figure A14: Simulated SOA yield as a function of time (a and b) and carbon budget (c to f) for α-pinene and limonene during photooxidation (a, c, e) and dark ozonolysis (b, d, f). The SOA yield curve for α-pinene is represented by a blue line; limonene is represented by a red line. For the carbon budget plots, the mixing ratios of the precursor (black line), particle-phase organics (magenta line), gas-phase organics (green line), and $CO+CO_2$ (blue line) are expressed as carbon atom ratios (in ppbC)/initial precursor (in ppbC). The results shown are for the high hydrocarbon mixing ratio (150 ppb) simulations.

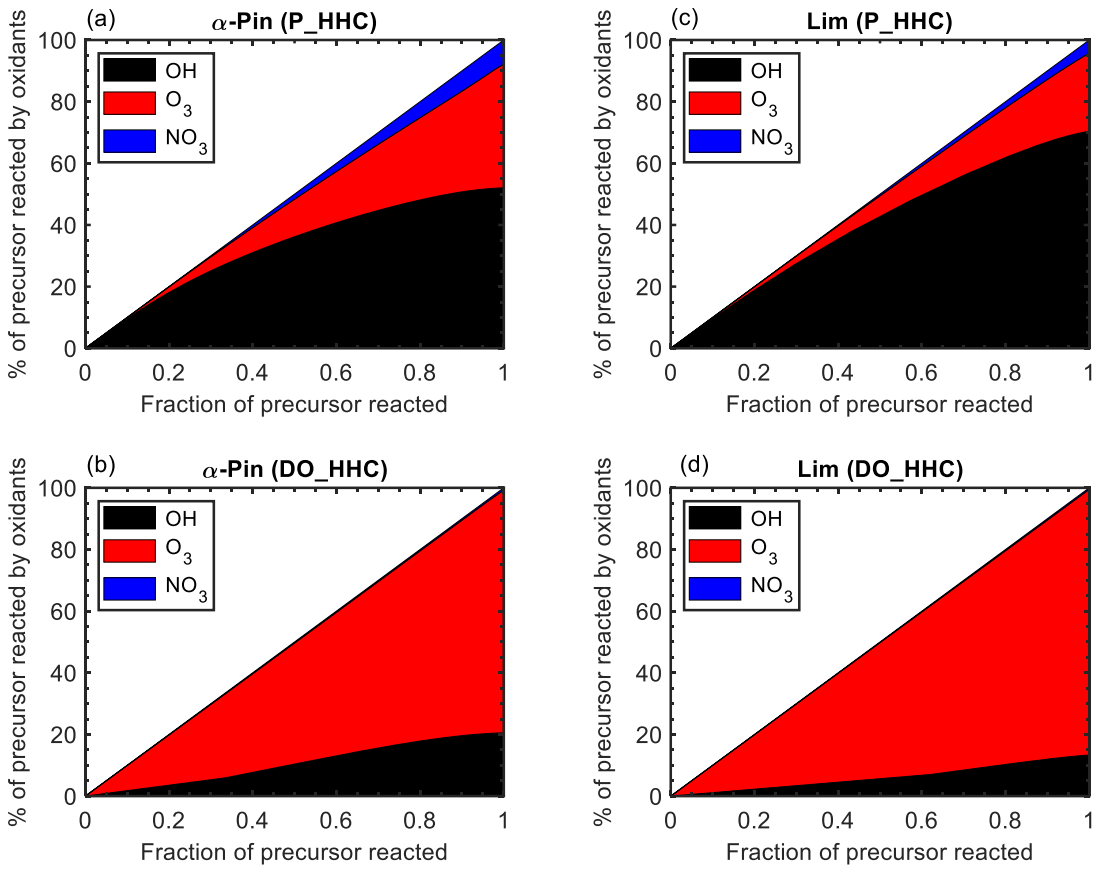

Figure A15: Percentage of precursor consumed by OH (black), O_3 (red), and NO_3 (blue) as a function of fraction of precursor reacted for α-pinene and limonene under photooxidation and ozonolysis (for higher initial precursor concentration of 150 ppb).

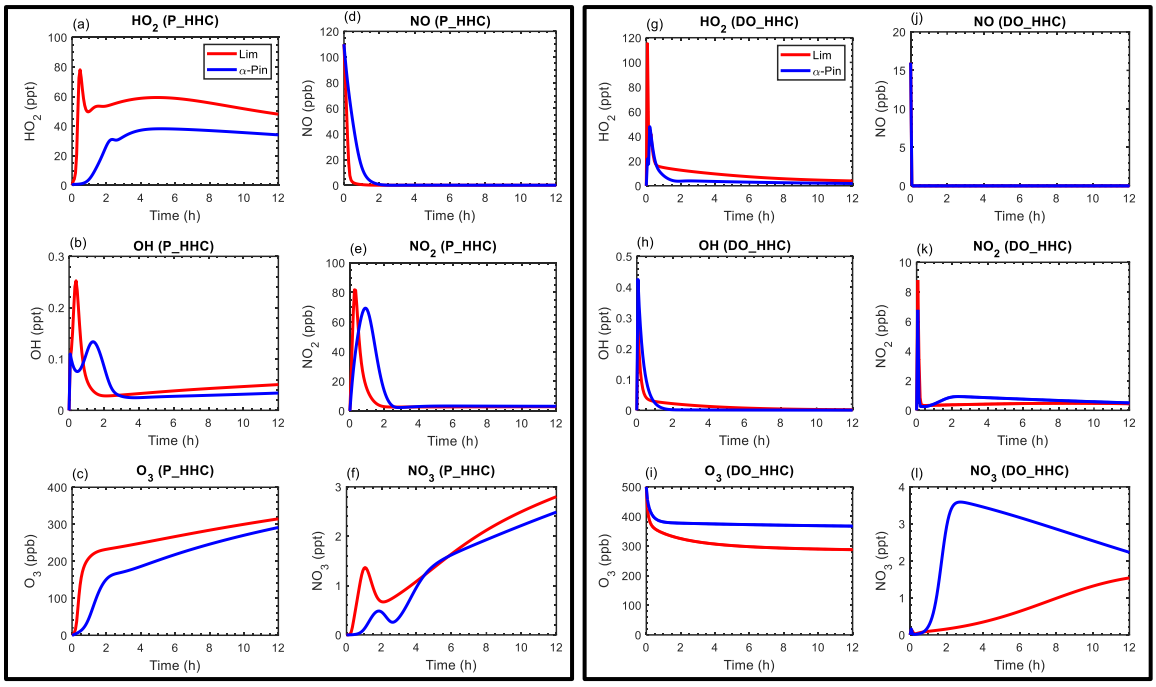

Figure A16: Mixing ratios of HO_2, OH, O_3, NO, NO_2, and NO_3 as function of time for limonene (red line), camphene (black line), and α-pinene (blue line) during the photooxidation and ozonolysis (with higher initial hydrocarbon mixing ratio of 150 ppb).

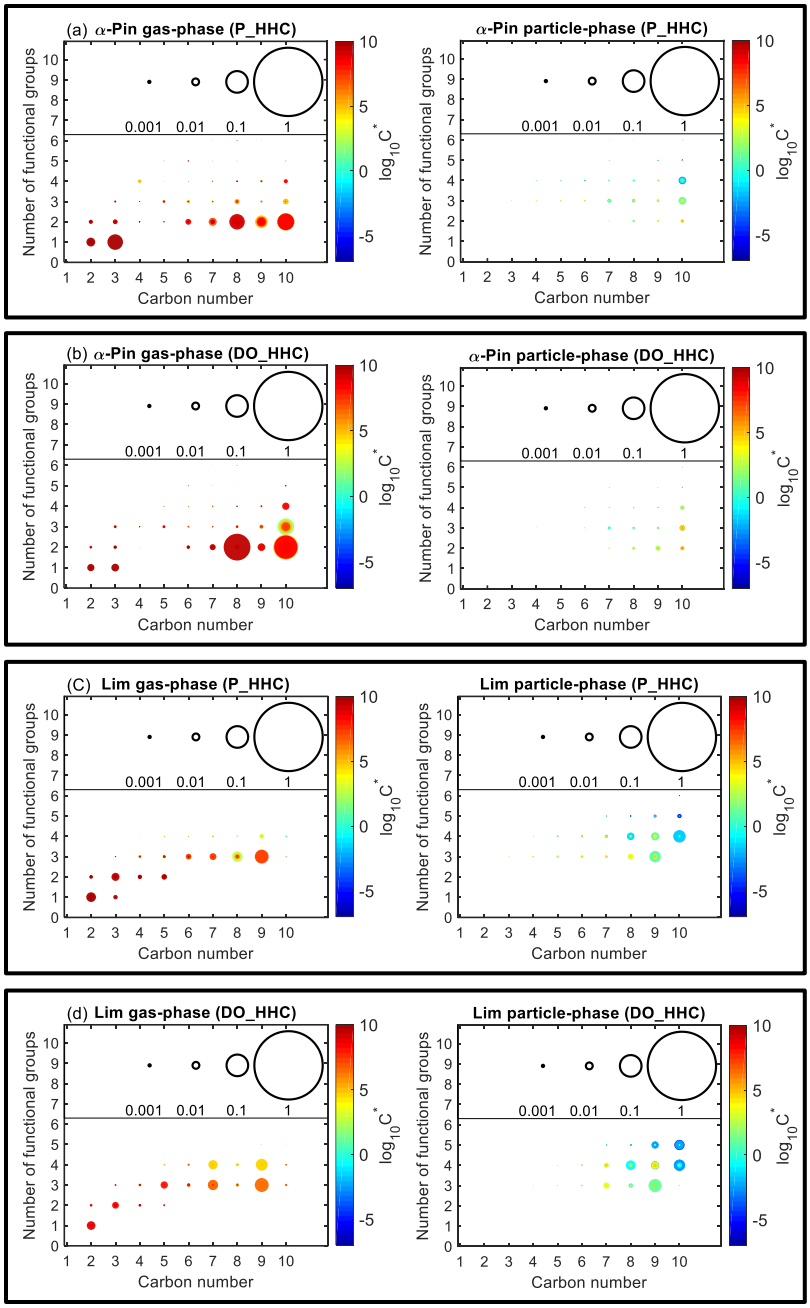

Figure A17: Number of functional groups associated with gas- and particle-phase species as a function of carbon number. Results are shown for camphene, α-pinene, and limonene after 12 hours of oxidation under photooxidation (P) and dark ozonolysis (DO) with higher hydrocarbon (LHC) mixing ratio of 150 ppb. The markers are sized by the ratio of theirmixing ratio (in ppbC) to the initial mixing ratio of the precursor (in ppbC). The colors of the markers are scaled by volatility (represented by saturation concentration, C*).

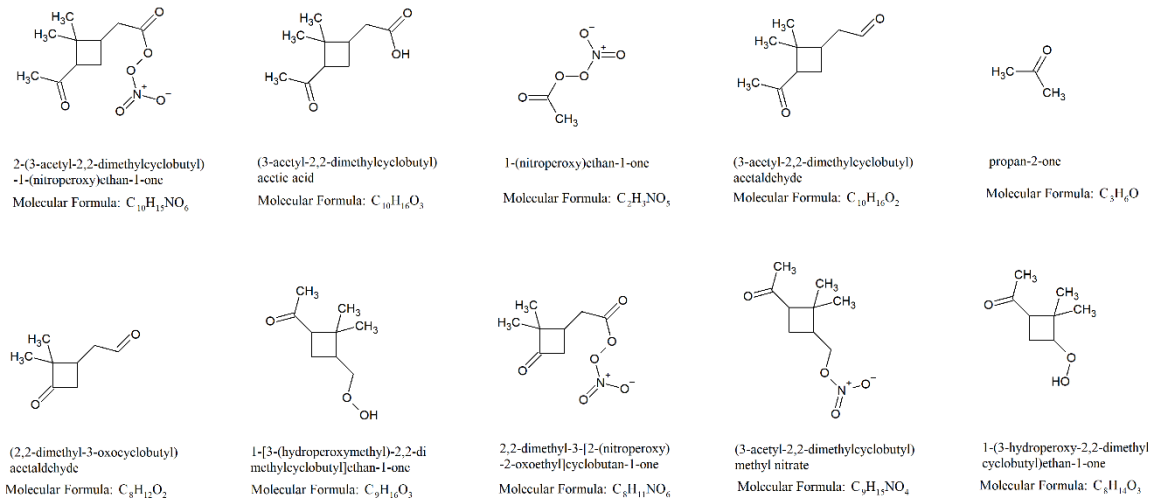

Figure A18: Top 10 gas-phase products from α-pinene photooxidation high hydrocarbon (P_HHC) simulations.

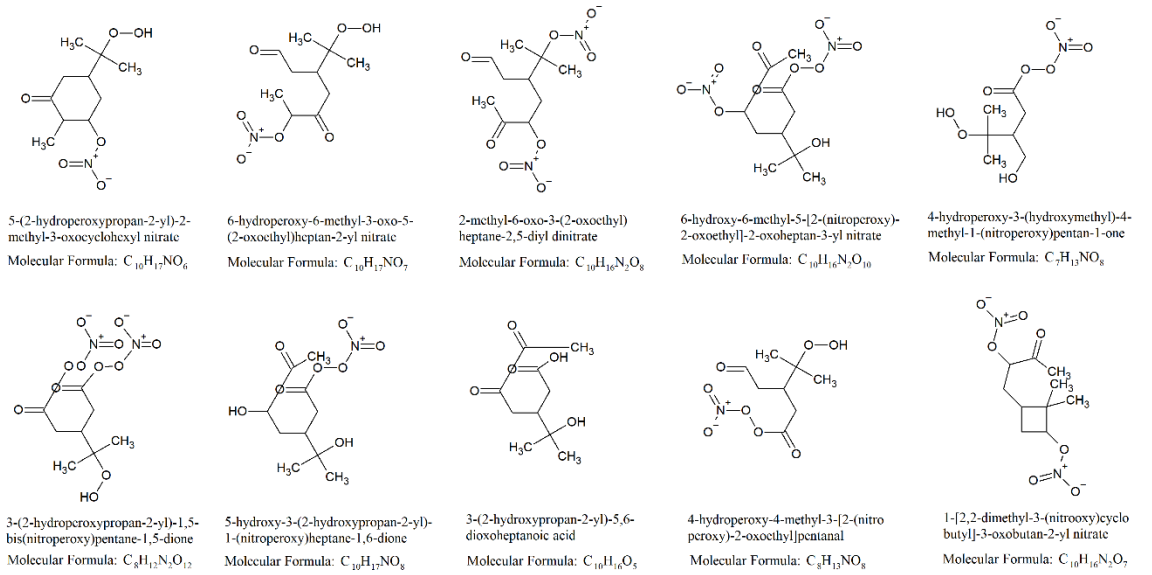

Figure A19: Top 10 particle-phase products from α-pinene photooxidation high hydrocarbon (P_HHC) simulations.

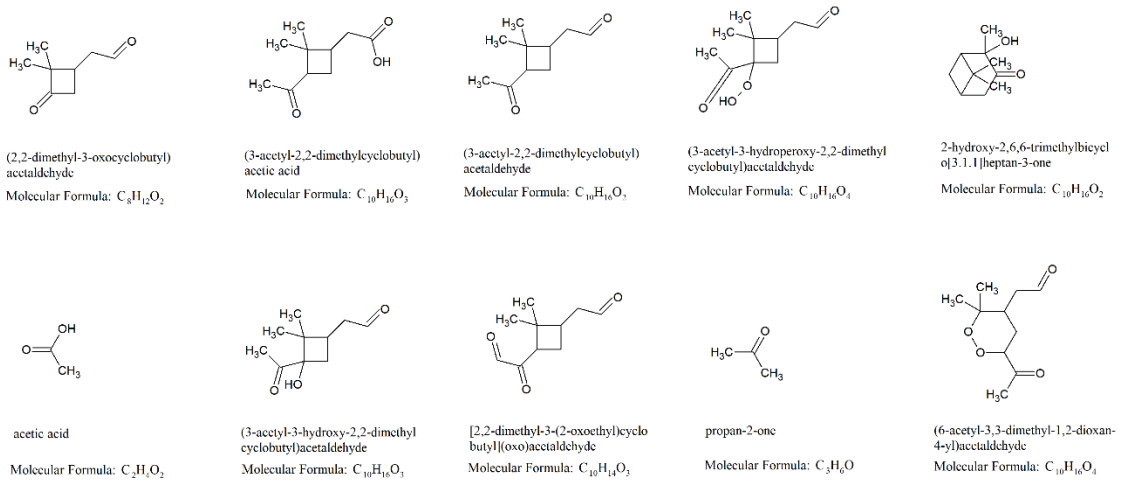

Figure A20: Top 10 gas-phase products from α-pinene dark ozonolysis high hydrocarbon (DO_HHC) simulations.

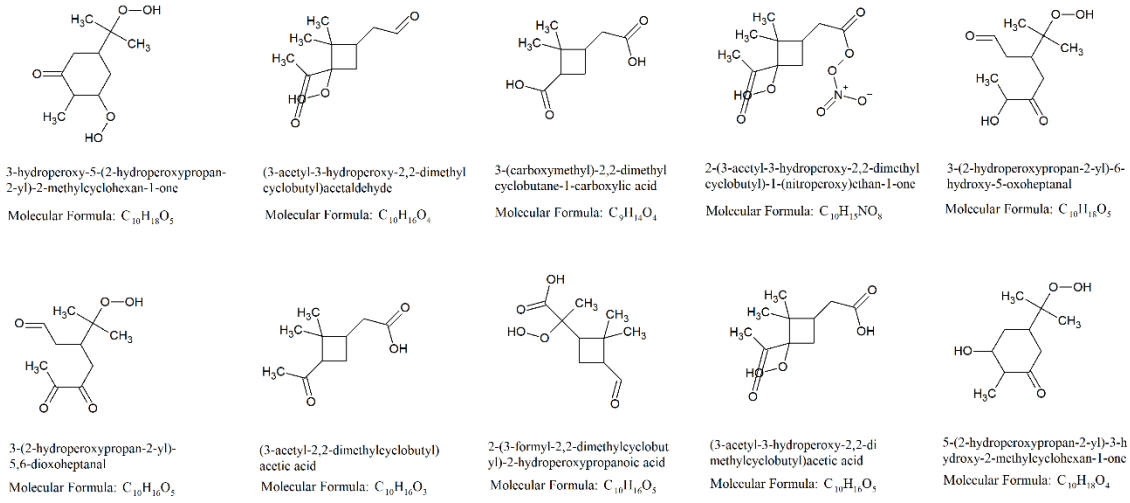

Figure A21: Top 10 particle-phase products from α-pinene dark ozonolysis high hydrocarbon (DO_HHC) simulations.

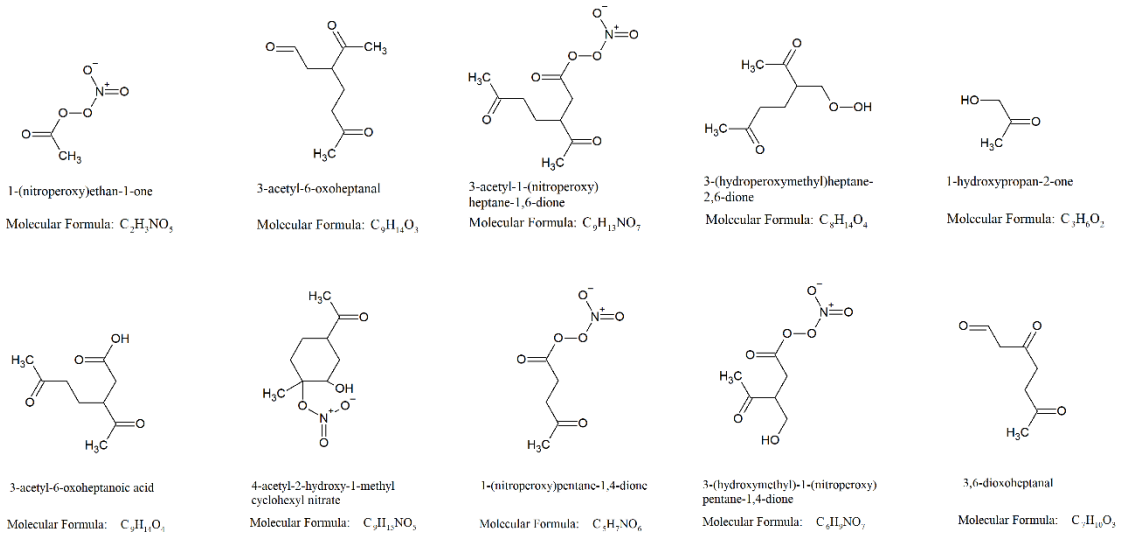

Figure A22: Top 10 gas-phase products from limonene photooxidation high hydrocarbon (P_HHC).

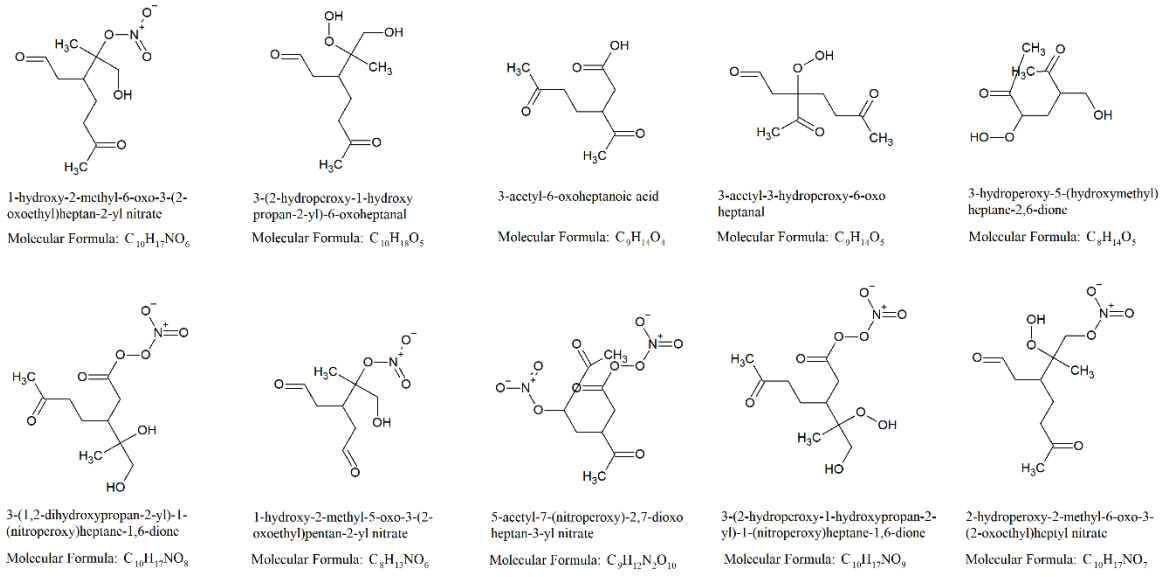

Figure A23: Top 10 particle-phase products from limonene photooxidation high hydrocarbon (P_HHC).

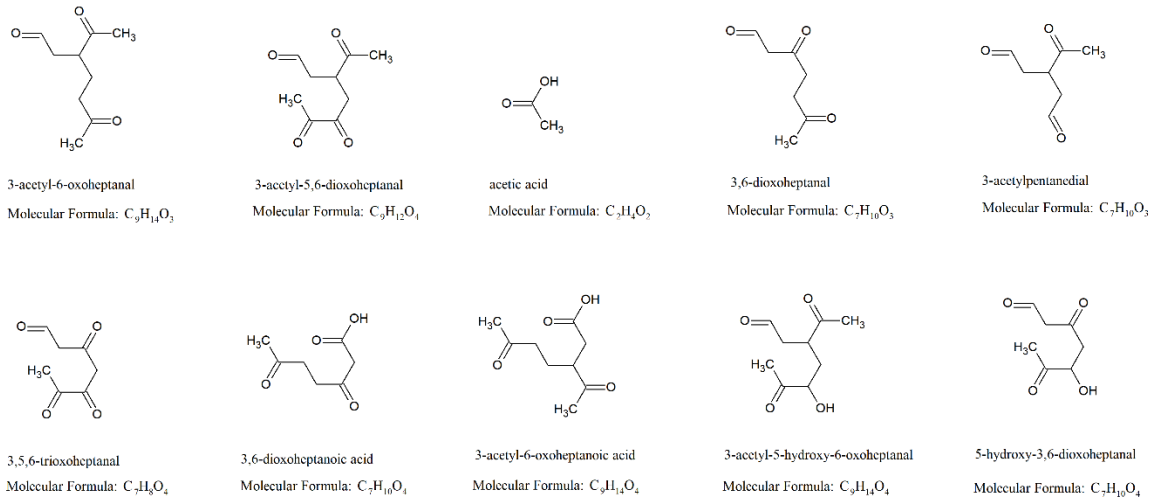

Figure A24: Top 10 gas-phase products from limonene dark ozonolysis high hydrocarbon (DO_HHC).

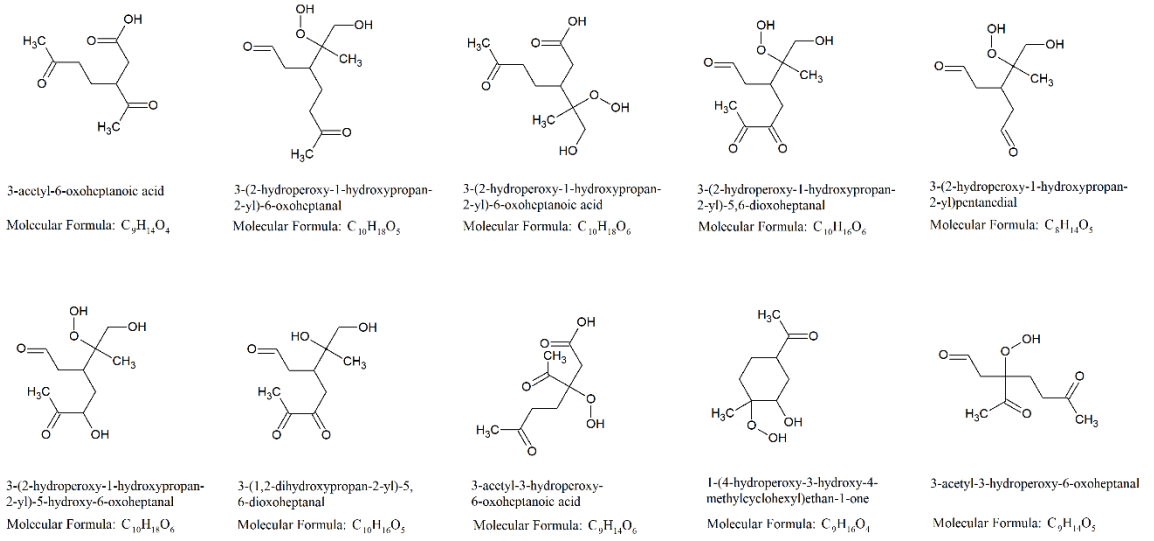

Figure A25: Top 10 particle-phase products from limonene dark ozonolysis high hydrocarbon (DO_HHC).

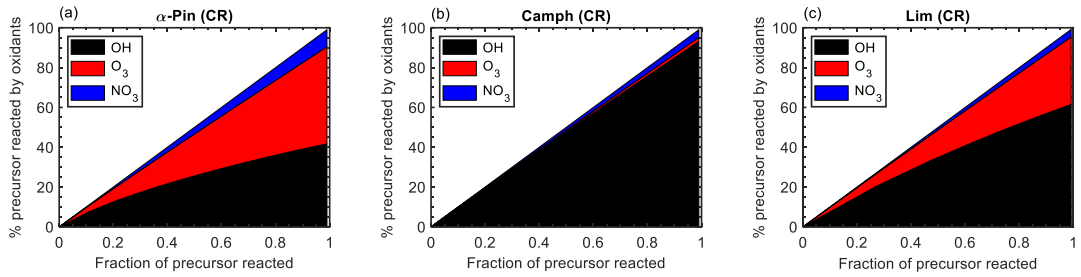

Figure A26: Percentage of precursor reacted by OH (black), O_3 (red), and NO_3 (blue) as a function of fraction of precursor reacted for α-pinene, camphene, and limonene during controlled reactivity (CR) simulations.

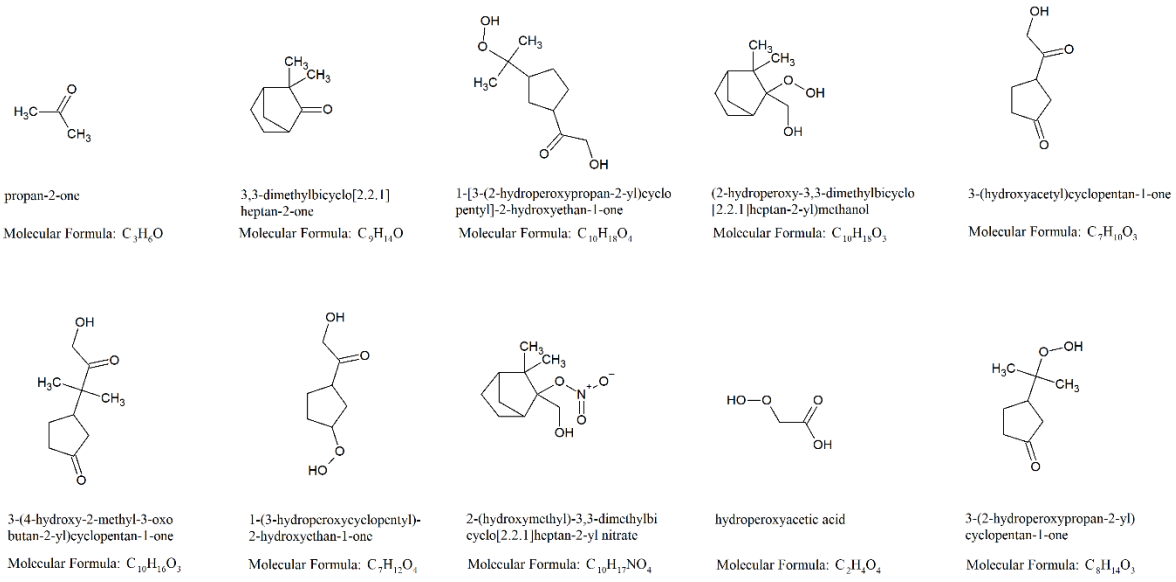

Figure A27: Top 10 gas-phase products from camphene controlled reactivity simulation.

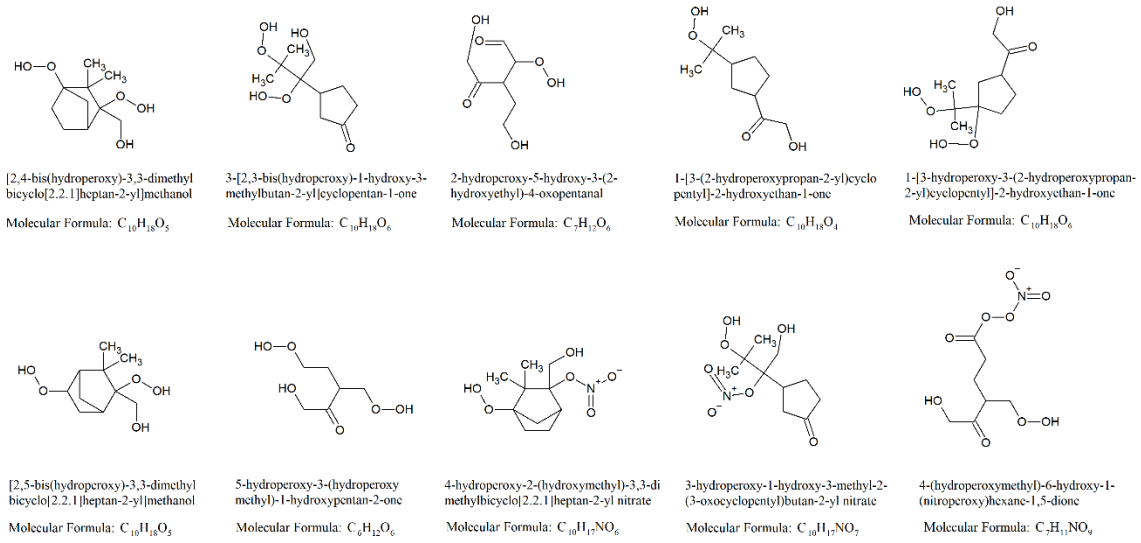

Figure A28: Top 10 particle-phase products from camphene controlled reactivity simulation.

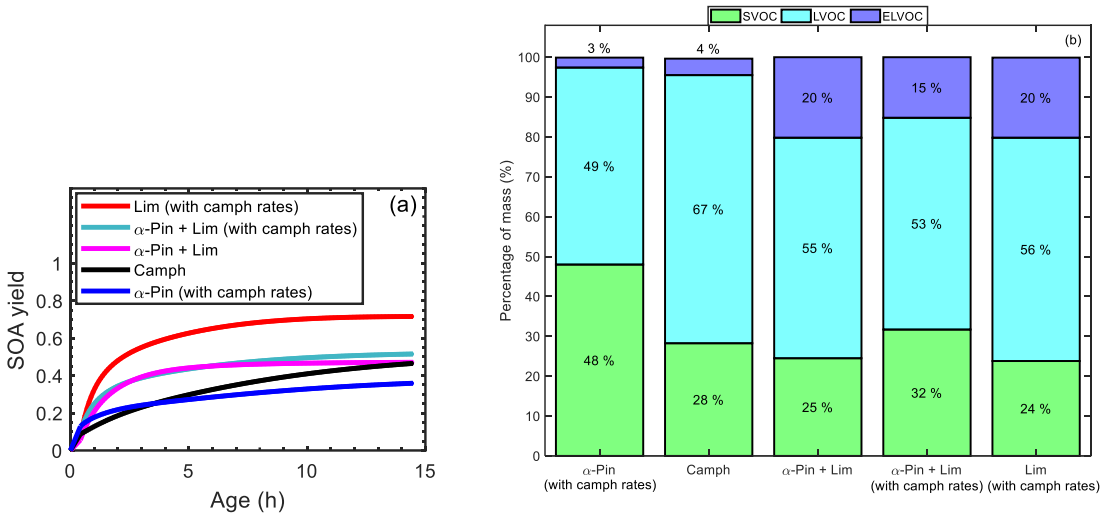

Figure A29: (a) Simulated SOA yield as a function of atmospheric aging time for camphene (black line), 50 % α-pinene + 50 % limonene (magenta line), α-pinene with camphene rate constants (blue line), limonene with camphene rate constants (red line), and 50 % α-pinene + 50 % limonene where the rate constants of α-pinene and limonene were replaced with the rate constants of camphene (green line); and (b) mass percentage of four volatility categories in the particle phase at the end of the controlled reactivity simulations for camphene, 50 % α-pinene + 50 % limonene, α-pinene with camphene rate constants, limonene with camphene rate constants, and 50 % α-pinene + 50 % limonene where the rate constants of α-pinene and limonene were replaced with the rate constants of camphene.

Chapter 3: Model-Measurement Comparison of Secondary Organic Aerosol Formation from the Photooxidation of Camphene

3.1 Introduction

Camphene is an abundant monoterpene emitted from both pyrogenic sources (e.g., Akagi et al., 2013; Gilman et al., 2015; Hatch et al., 2015) and biogenic sources (Geron et al., 2000; Hayward et al., 2001; Ludley et al., 2009; Maleknia et al., 2007; Rinne et al., 2000; Tani et al., 2003; White et al., 2008). The quantities of camphene emitted from biogenic sources (e.g., forests, marine, and soil) typically depend on plant species, temperature, and light (e.g., Hayward et al., 2001; Yáñez-Serrano et al., 2018; White et al., 2008). Likewise, emissions of camphene from pyrogenic sources are influenced by fuel component and plant type (e.g., Hatch et al., 2019). For example, in laboratory and prescribed fire measurements reported by Hatch et al. (2019), camphene was among the top two monoterpenes, based on emission factor (mass of compound emitted/mass of fuel burned), emitted from subalpine and Douglas fir fires. Monoterpenes, when emitted to the atmosphere, can act as secondary organic aerosol (SOA) precursors. The SOA formation potential of individual monoterpenes can vary greatly based on their molecular structure, atmospheric lifetimes, and the volatility of their oxidation products (Atkinson and Arey, 2003; Griffin et al., 1999; Ng et al., 2007; Zhang et al., 2015). Elucidating SOA formation from individual monoterpenes is crucial since SOA forms a significant mass fraction of particulate matter (PM) (Jimenez et al., 2009), which adversely impacts climate and air quality (Almatarneh et al., 2018; Jacobson et al., 2000; Kanakidou et al., 2004). Despite the efforts to model and measure SOA from monoterpenes, a large number of monoterpenes remain understudied.

While camphene is emitted in non-negligible quantities, its SOA formation has not been explored experimentally. Past studies on camphene have been limited to gas-phase reactivity and product identification (e.g., Atkinson et al., 1990; Gaona-Colmán et al., 2017; Hakola et al., 1994). Additionally, Baruah et al. (2018) performed density functional theory (DFT) study on the gas-phase oxidation and product formation from camphene. Recently, Afreh et al. (2020) used an explicit model to explore SOA formation from camphene. They demonstrated that, under controlled atmospheric conditions, the camphene SOA yield can be approximately twice the α-pinene SOA yield. Also, Afreh et al. (2020) demonstrated the potential importance of representing camphene SOA in air quality models. While the mechanistic study on camphene provided great insight into SOA formation potential of camphene, no chamber data were available for model-measurement comparison.

In this work, GECKO-A simulations were performed for camphene under chamber photooxidation conditions to further explore SOA formation from camphene. Initial conditions included five hydrocarbon mixing ratios and two NOx levels (with and without addition of initial NOx). To allow model-measurement comparison, chamber experiments were conducted in the UCR environmental chamber under similar photooxidation conditions. The model-measurement comparison included SOA yield trends and gas-phase reactivity. GECKO-A results provided mechanistic explanation to the SOA trends observed in the chamber data.

3.2 Method

3.2.1 Chamber studies and results

The chamber studies detailed in this section were led by Qi Li, a graduate student in Dr. Cocker's research group. Qi Li ran the chamber experiments and provided the chamber data output. My role was to help establish the initial conditions, propose new experiments based on GECKO-A simulations, and analyze simulation results.

Photooxidation experiments were conducted for camphene in the UCR environmental dual chamber under two NOx conditions: (1) injection of 60-138 ppb NOx, referred to as "with NOx"; and (2) with no injection of initial NOx, referred to as "without NOx". For each NOx condition, six experiments with different initial hydrocarbon mixing ratios were performed. The H_2O_2 mixing ratio ranged from 854 to 1576 ppb. The relative humidity (< 0.1 %) and temperature (300 ± 1 K) in the chamber were controlled for all experiments. The summary of the initial conditions and chamber SOA data are provided in Table 3.1 To facilitate model-measurement comparison, GECKO-A simulations were performed for camphene under photooxidation conditions similar to those used for the chamber experiments.

Table 3. 1: Initial conditions and chamber SOA data for camphene photooxidation experiments.

Experiment	NO (ppb)	NO_2 (ppb)	ΔHC (ppb)	ΔHC ($\mu g\ m^{-3}$)	SOA mass ($\mu g\ m^{-3}$)	SOA yield
With NOx						
EPA2577b	45	14	171.87	950.00	529.34	0.56
EPA2548a	42	56	131.00	719.00	428.80	0.60
EPA2548b	45	49	60.40	332.00	199.50	0.60
EPA2594b	5	2	42.80	236.60	96.00	0.41
EPA2558b	51	11	31.98	172.00	112.32	0.65
EPA2595b	114	24	25.30	139.80	46.10	0.33
EPA2593b	86	2	7.30	40.40	14.60	0.36
Without NOx						
EPA2559a	-	-	152.69	844.00	162.44	0.19
EPA2540a	-	-	108.00	597.00	158.60	0.27
EPA2540b	-	-	55.20	305.00	84.40	0.28
EPA2559b	-	-	27.68	153.00	42.01	0.27
EPA2602b	-	-	8.80	48.80	3.69	0.08
EPA2592b	-	-	7.40	41.10	6.10	0.15

3.2.2 Model description and simulation conditions

SOA formation from camphene was simulated using a nearly explicit model, GECKO-A. GECKO-A relies on experimental data and structure-activity relationships (SARs) to generate detailed oxidation reaction schemes for organic compounds and simulate their SOA formation under general atmospheric conditions. Aumont et al. (2005) provided a detailed description of GECKO-A. In this work, GECKO-A was used to derive an oxidation scheme of up to six generations for camphene. The camphene oxidation scheme included 1.3×10^6 reactions and 1.8×10^5 oxidation products. The camphene oxidation scheme was coupled to the GECKO-A box model to simulate SOA formation. The gas/particle partitioning of oxidation species was based on the absorptive model by

Pankow et al., (1994), where a thermodynamic equilibrium between the gas and an ideal particle phase was assumed (Camredon et al., 2007). Autoxidation and particle-phase reactions were not considered in the model.

Table 3.2: Initial conditions of GECKO-A simulations.

Duration (h)	HC (ppb)	NO (ppb)	H_2O_2 (ppb)
With NOx			
8	10	80	1000
8	25	80	1000
8	50	80	1000
8	100	80	1000
8	150	80	1000
Without NOx			
8	10	0	1000
8	25	0	1000
8	50	0	1000
8	100	0	1000
8	150	0	1000

GECKO-A simulations were performed for camphene under chamber photooxidation conditions, where the initial hydrocarbon concentration was varied with 80 ppb of NOx present and without NOx present (Table 3.2). For both NOx conditions, the initial hydrocarbon mixing ratios ranged from 10 ppb to 150 ppb. All simulations were run under the following initial conditions: 1000 ppb of H_2O_2 and 1 µg m^{-3} of organic seed with molecular weight of 250 g mol^{-1}, 298 K temperature, 50 % relative humidity, and 50^o solar zenith angle (required to compute the photolysis frequencies). Simulation results for

camphene were compared with chamber data including SOA yield and gas-phase reactivity.

3.3 Results and discussion

3.3.1 Model-measurement SOA yield comparison

The SOA yields based on the chamber data (Fig 3.1a) and the simulations (Fig. 3.1b) are shown in Figure 3.1; experiments and simulations with NOx are indicated using solid circles and without NOx using solid squares. While the simulated SOA yields (0.81-0.93) were higher than the measured SOA yields (0.33-0.65) when NOx was present, the SOA yield trends were similar. As shown in Fig. 3.1b, the simulated SOA yield increased with SOA mass for SOA mass < 200, plateaued for SOA mass between 200 and 550 $\mu g\ m^{-3}$, and then decreased for SOA mass > 550 $\mu g\ m^{-3}$. The decrease in SOA yield from 0.93 (at 524 $\mu g\ m^{-3}$) to 0.86 (at 717 $\mu g\ m^{-3}$) is due to the influence of NO_3 chemistry and the slower consumption of camphene as the initial hydrocarbon mixing ratio of camphene increased from 100 ppb to 150 ppb. Without NOx present, the simulated SOA yield (0.73-1.25) and mass (70-511 $\mu g\ m^{-3}$) were significantly higher than the measured SOA yield (0.08-0.26) and mass (2.6-124). At low mass loadings (SOA mass < 300 $\mu g\ m^{-3}$), there is a reverse in the SOA yield trend between with/without NOx between the model and measurements; for the model, without NOx has a higher SOA yield while for the measurements, the without NOx has a lower SOA yield. Model-measurement comparisons for the without NOx conditions should be made carefully, as GECKO-A has not been optimized for low NOx conditions. As shown in Fig. 3.1b, for the simulations without NOx, the SOA yield decreased with increasing SOA mass. However, for the measurements

without, SOA yield increased initially, plateaued for SOA mass between 40 and 160 µg m^{-3}, and then decreased SOA mass > 160 µg m^{-3}.

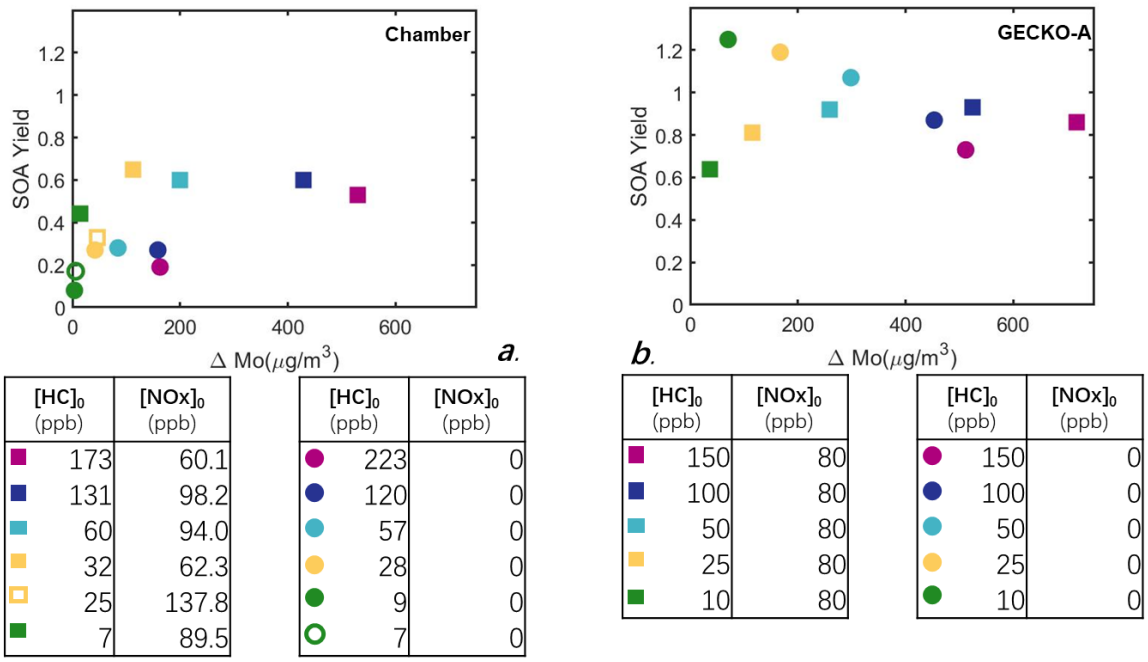

[HC]0 (ppb)	[NOx]0 (ppb)
173	60.1
131	98.2
60	94.0
32	62.3
25	137.8
7	89.5

[HC]0 (ppb)	[NOx]0 (ppb)
223	0
120	0
57	0
28	0
9	0
7	0

[HC]0 (ppb)	[NOx]0 (ppb)
150	80
100	80
50	80
25	80
10	80

[HC]0 (ppb)	[NOx]0 (ppb)
150	0
100	0
50	0
25	0
10	0

Figure 3.1: SOA yields of camphene as a function of SOA mass derived from environmental chamber experimental results (a) and GECKO-A simulations results (b).

3.3.2 Gas-phase reactivity comparison

Figure 3.2 shows the model-chamber comparison of mixing ratios of camphene, O_3, and OH as function of time for camphene oxidation with NOx and without NOx. The camphene decay was slightly faster in the chamber experiment than simulated by the model under both NOx conditions. The ozone levels (280-310 ppb) simulated by the model were within the range of ozone levels (100-350 ppb) measured in the chamber when NOx was present.

In the absence of NOx, the simulated ozone levels (0.07-0.3 ppb) were significantly lower than the measured ozone levels (20-50 ppb). The relatively higher ozone levels measured in experiments without NOx is likely due to wall loss effect and HONO offgasing, which produces NO in the chamber. While wall loss effect and HONO offgasing were present in the chamber, both processes were absent in the model simulations. For OH mixing ratio, the model output was consistent with the chamber output when NOx was present. Similarly, the model output of OH mixing ratio was similar to that of the chamber output for experiments without NOx when the initial hydrocarbon mixing $\geq$ 50 ppb. Overall, more model-measurement consistencies were observed when NOx was present in the initial conditions.

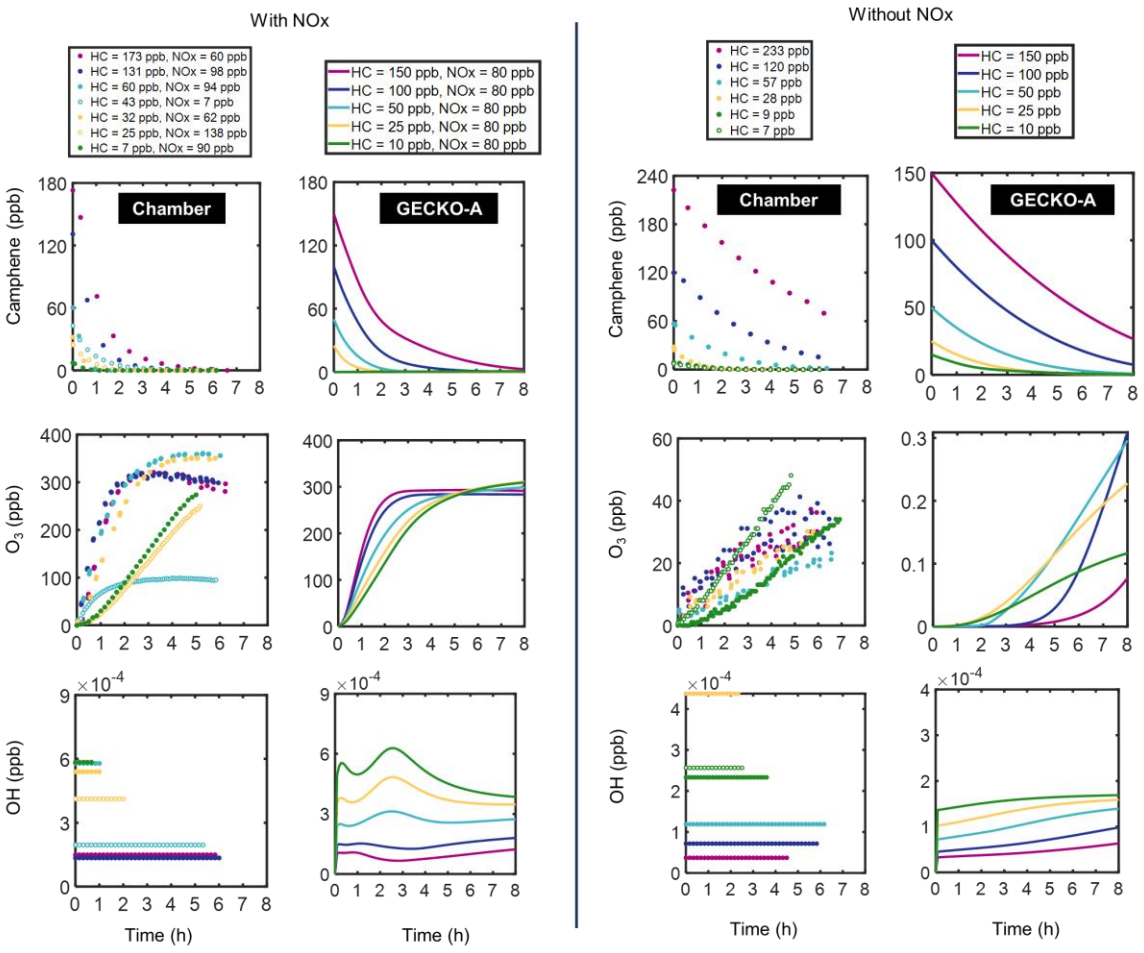

Figure 3. 2: model-chamber comparison of mixing ratios of camphene, O_3, and OH as function of time for camphene oxidation with NOx and without NOx.

3.3.3 Simulated carbon budget

The time evolution of the carbon budget during camphene photooxidation simulations with and without NOx are shown in Figures 3.2 and 3.3, respectively. For simulations with NOx, camphene was largely oxidized by OH at lower initial hydrocarbon mixing ratios (10 ppb, 25 ppb, and 50 ppb). However, at relatively higher initial hydrocarbon mixing ratios (100 ppb and 150 ppb), camphene was oxidized by OH and

partly by NO_3 (Fig. B1) due to decrease in OH level as the initial hydrocarbon mixing ratio increased (Fig. B3). During photooxidation simulation with NOx, the fraction of oxidation product in the particle phase increased from 0.25 (at 10 ppb camphene) to 0.4 (at 50 ppb camphene). The fraction of particle-phase organics remained at ~ 0.4 for simulations at 100 ppb and 150 ppb camphene, supporting the observed plateau in SOA yield for SOA mass between 200 and 550 $\mu g\ m^{-3}$.

For simulations without NOx, camphene oxidation was driven entirely by OH (Fig. B2). Therefore, the consumption of camphene slowed down as OH level decreased with increasing initial hydrocarbon mixing ratio (Fig. B4). As initial hydrocarbon mixing ratio increased, the fraction of particle-phase organics decreased, and the faction of gas-phase organics increased (Fig. 3.3) due to decreased in OH level, consistent with the decreasing SOA yield trend observed in the simulations without NOx.

Table 3.3: Calculated average mass-weighted O/C ratio at the end of camphene photooxidation simulations.

$[HC]_o$	Average O/C
with NOx	
10	1.25
25	1.19
50	1.10
100	0.82
150	0.68
without NOx	
10	0.50
25	0.49
50	0.46
100	0.43
150	0.42

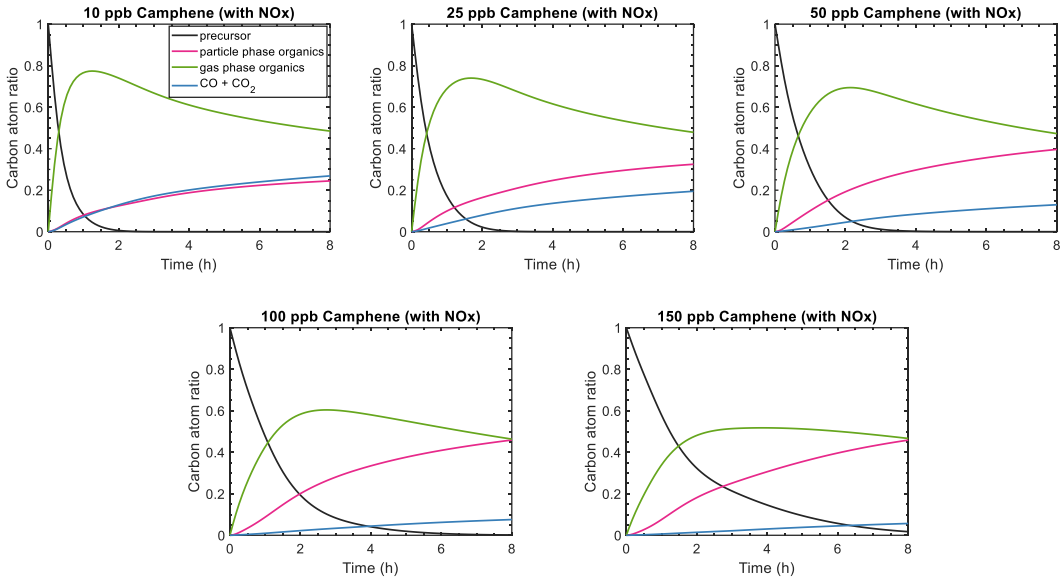

Figure 3.3: Carbon budget as a function of time for camphene photooxidation simulations with NOx.

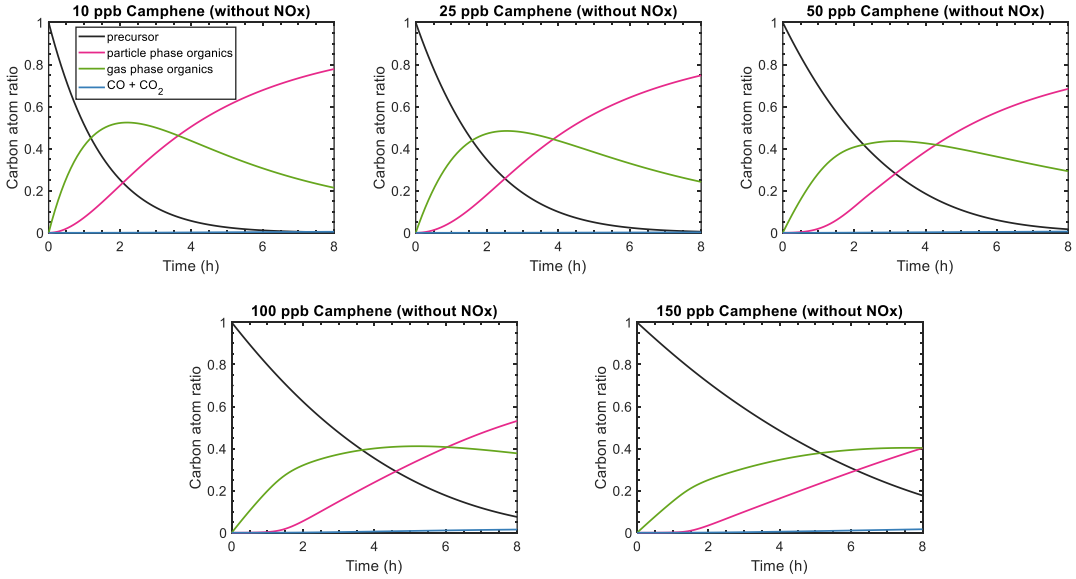

Figure 3.4: Carbon budget as a function of time for camphene photooxidation simulations without NOx.

3.3.4 Particle-phase product distribution

Figure 3.5 shows the final product distribution in the gas- and particle-phases for simulations with NOx. When NOx is present, the particle phase is dominated by C7 (with 3 to 5 functional groups) and C10 (with 2 to 5 functional groups) products. The C7 products contribute the most to the SOA mass, particularly for simulations with lower initial hydrocarbon mixing ratios (10-50 ppb), and the volatility of these products is lower than the volatility of the C10 products. As the initial hydrocarbon mixing ratio increases, the contribution of C7 products to the SOA mass decreases. For example, the top 5 particle-phase products from 10 ppb camphene simulation were dominated by C7 products (Fig. 3.7), while the top 5 particle-phase products from 150 ppb camphene simulation were dominated by C10 products (Fig. 3.8). Generally, the volatility of the particle-phase products increases (as indicated by the decrease in average O/C (Table 3.3)) as the initial hydrocarbon mixing ratio increases. For simulations with NOx, the top 5 particle-phase products predicted by the model indicate that the SOA formation was driven by RO_2+NO pathway, whereas the top 5 particle-phase products from simulations without NOx suggest that the SOA formation was driven by RO_2+HO_2 pathway. For simulations without NOx, the particle phase is dominated largely by C10 products (Figures 3.6, 3.9, 3.10). As the initial hydrocarbon mixing ratio increases, the volatility of the particle-phase C10 products increases. Figures 3.5 and 3.6 demonstrate how initial hydrocarbon concentration and NOx conditions influence the properties and mass of camphene particle-phase products.

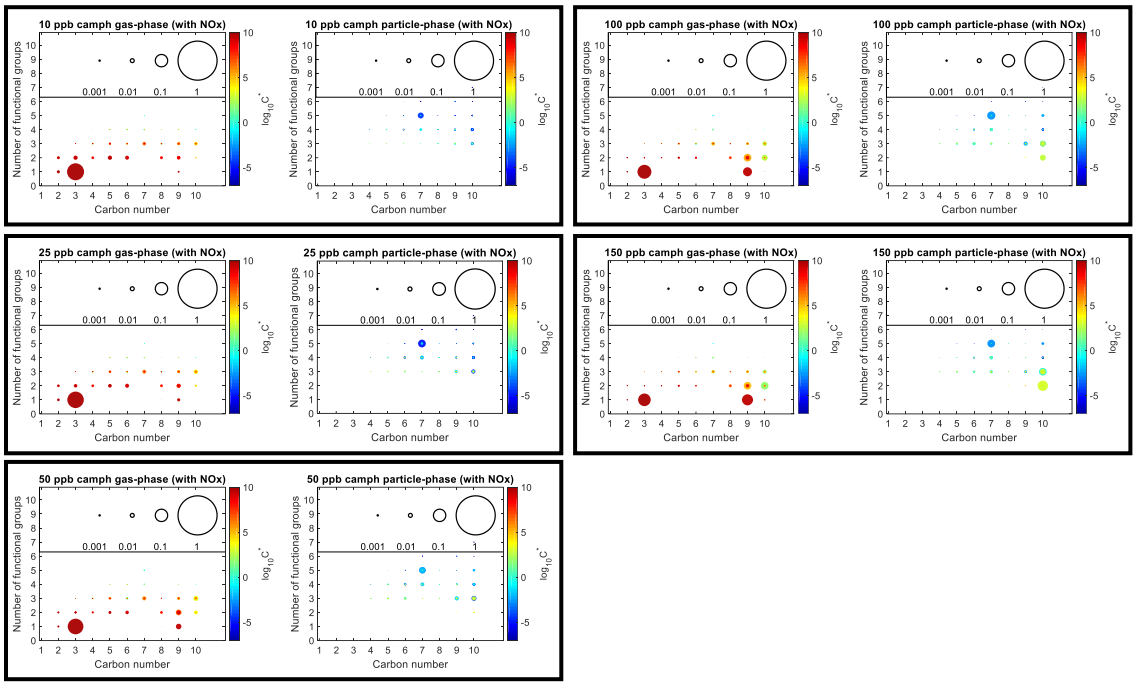

Figure 3.5: Number of functional groups associated with gas- and particle-phase species as a function of carbon number for simulations with NOx. Results are shown for camphene after 8 hours of photooxidation. The markers are sized by the ratio of their mixing ratio (in ppbC) to the initial mixing ratio of the precursor (in ppbC). The colors of the markers are scaled by volatility (represented by saturation concentration, C*).

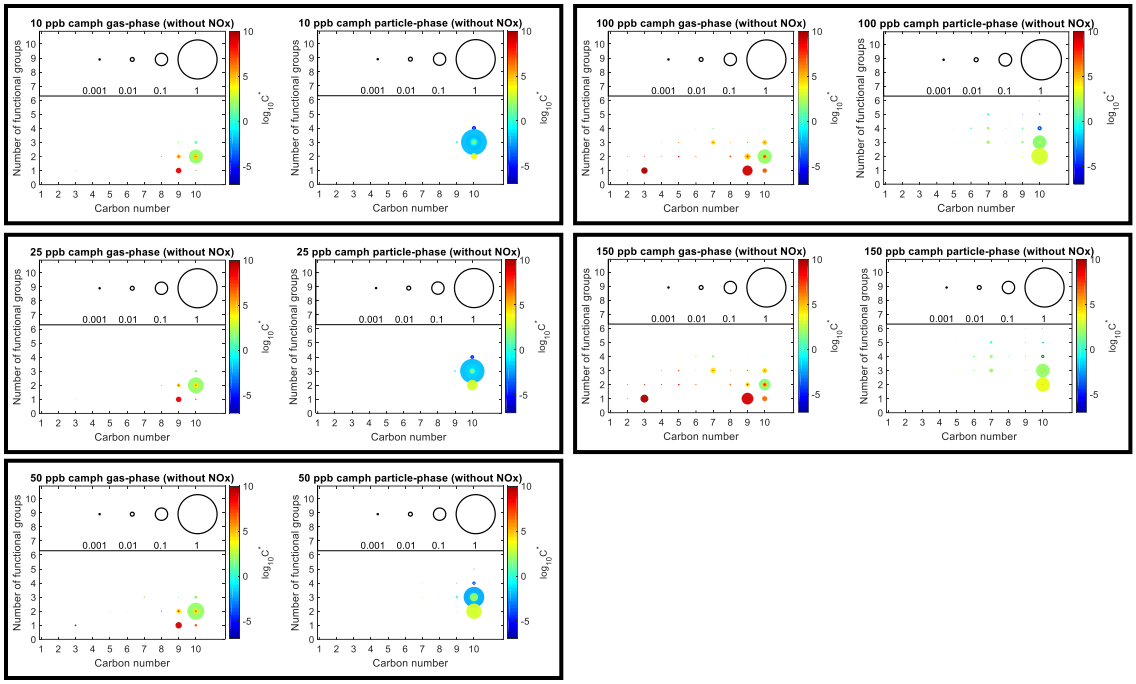

Figure 3.6: Number of functional groups associated with gas- and particle-phase species as a function of carbon number for simulations without NOx. Results are shown for camphene after 8 hours of photooxidation. The markers are sized by the ratio of their mixing ratio (in ppbC) to the initial mixing ratio of the precursor (in ppbC). The colors of the markers are scaled by volatility (represented by saturation concentration, C*).

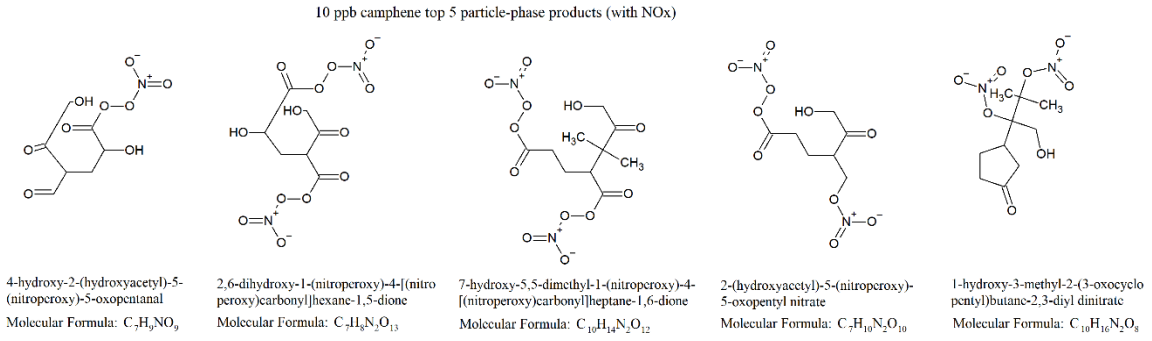

Figure 3.7: Top 5 particle-phase products from 10 ppb camphene photooxidation simulation with NOx.

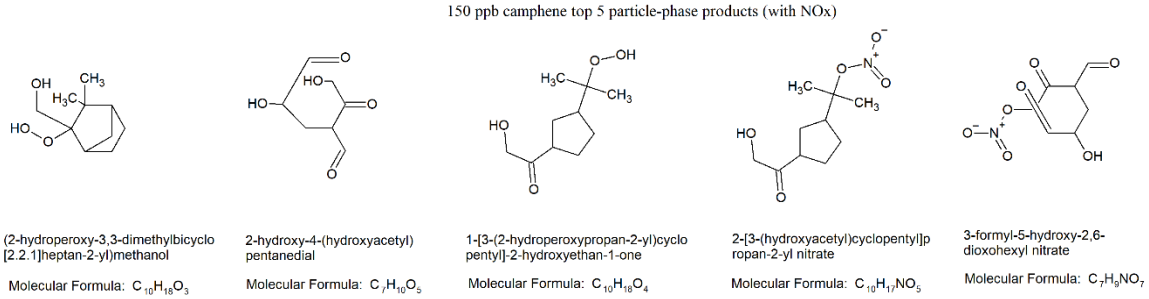

Figure 3.8: Top 5 particle-phase products from 150 ppb camphene photooxidation simulation with NOx.

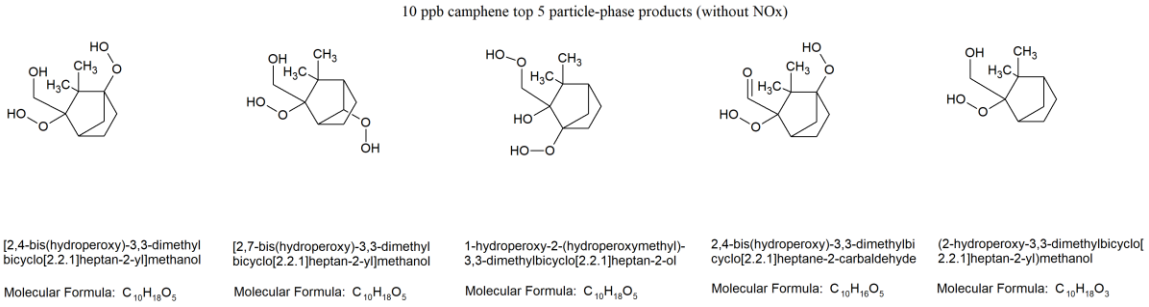

Figure 3.9: Top 5 particle-phase products from 10 ppb camphene photooxidation simulation without NOx.

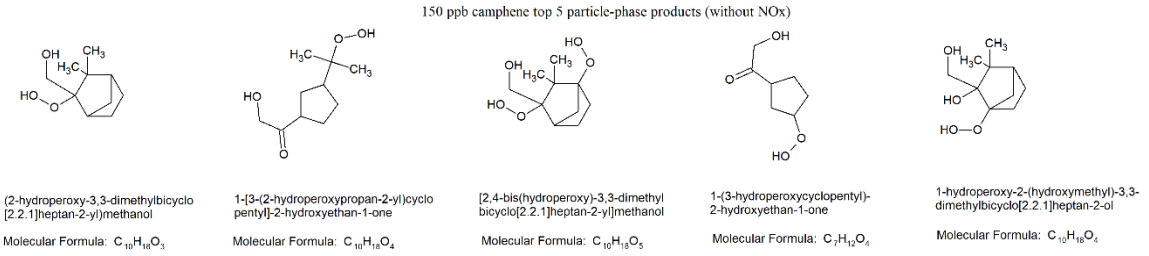

Figure 3.10: Top 5 particle-phase products from 150 ppb camphene photooxidation simulation without NOx.

3.4 Conclusions

GECKO-A simulations and chamber studies were performed for camphene under photooxidation conditions with and without NOx. The SOA yields simulated by model, with NOx present, ranged from 0.81-0.93 while the SOA yields measured from the chamber experiments with NOx present ranged from 0.33 to 0.65. While the SOA yields simulated by the model were higher than observed in the chamber, the SOA yield trends were similar between the SOA model simulations and the chamber studies when NOx was present. Generally, the mixing ratios of OH, ozone, and camphene decay generated by the model were consistent with the chamber data when NOx was present. For simulations with NOx, the particle phase is dominated by C7 and C10 products, whereas for simulations without NOx the particle phase is dominated largely by C10 products. As expected, the top 5 particle-phase products formed from the simulations with NOx demonstrated that the SOA formation was driven by RO_2+NO pathway, whereas the top 5 particle-phase products from the simulations without NOx demonstrated that the SOA formation was driven by RO_2+HO_2 pathway.

References

Afreh, I. K., Aumont, B., Camredon, M., and Barsanti, K. C.: Using GECKO-A to derive mechanistic understanding of SOA formation from the ubiquitous but understudied camphene, Atmos. Chem. Phys. Discuss., https://doi.org/10.5194/acp-2020-829, in review, 2020.

Akagi, S. K., Yokelson, R. J., Burling, I. R., Meinardi, S., Simpson, I., Blake, D. R., McMeeking, G. R., Sullivan, A., Lee, T., Kreidenweis, S., Urbanski, S., Reardon, J., Griffith, D. W. T., Johnson, T. J., and Weise, D. R.: Measurements of reactive trace gases and variable O_3 formation rates in some South Carolina biomass burning plumes, Atmos. Chem. Phys., 13(3), 1141–1165, https://doi.org/10.5194/acp-13-1141-2013, 2013.

Almatarneh, M. H., Elayan, I. A., Poirier, R. A., and Altarawneh, M.: The ozonolysis of cyclic monoterpenes: A computational review, Can. J. Chem., 96(3), 281–292, https://doi.org/10.1139/cjc-2017-0587, 2018.

Atkinson, R., and Arey, J.: Gas-phase tropospheric chemistry of biogenic volatile organic compounds: A review, Atmos. Environ., 37(2), 197–219, https://doi.org/10.1016/S1352-2310(03)00391-1, 2003.

Atkinson, R., Aschmann, S. M., and Arey, J.: Rate constants for the gas-phase reactions of OH and NO_3 radicals and O_3 with sabinene and camphene at 296±2 K, Atmos, Environ. Part A, General Topics, 24(10), 2647–2654, https://doi.org/10.1016/0960-1686(90)90144-C, 1990.

Aumont, B., Szopa, S., and Madronich, S.: Modelling the evolution of organic carbon during its gas-phase tropospheric oxidation: development of an explicit model based on a self generating approach, Atmos. Chem. Phys. Discuss., 5(1), 703–754, https://doi.org/10.5194/acpd-5-703-2005, 2005.

Camredon, M., Aumont, B., Lee-Taylor, J., and Madronich, S.: The SOA/VOC/NO_x system: An explicit model of secondary organic aerosol formation. Atmos. Chem. Phys., 7(21), 5599–5610, https://doi.org/10.5194/acp-7-5599-2007, 2007.

Gaona-Colmán, E., Blanco, M. B., Barnes, I., Wiesen, P., and Teruel, M. A.: OH- and O_3-initiated atmospheric degradation of camphene: Temperature dependent rate coefficients, product yields and mechanisms, RSC Adv., 7(5), 2733–2744, https://doi.org/10.1039/c6ra26656h, 2017.

Geron, C., Rasmussen, R., Arnts, R. R., and Guenther, A.: A review and synthesis of monoterpene speciation from forests in the United States, Atmos. Environ., 34(11), 1761–1781, https://doi.org/10.1016/S1352-2310(99)00364-7, 2000.

Gilman, J. B., Lerner, B. M., Kuster, W. C., Goldan, P. D., Warneke, C., Veres, P. R., Roberts, J. M., de Gouw, J. A., Burling, I. R., and Yokelson, R. J.: Biomass burning emissions and potential air quality impacts of volatile organic compounds and other trace gases from fuels common in the US, Atmos. Chem. Phys., 15(24), 13915–13938, https://doi.org/10.5194/acp-15-13915-2015, 2015.

Griffin, R. J., Cocker, D. R., Flagan, R. C., and Seinfeld, J. H.: Organic aerosol formation from the oxidation of biogenic hydrocarbons, J. Geophys. Res. Atmos., 104(D3), 3555–3567, https://doi.org/10.1029/1998JD100049, 1999.

Hakola, H., Arey, J., Aschmann, S. M., and Atkinson, R.: Product formation from the gas-phase reactions of OH radicals and O_3 with a series of monoterpenes, J. Atmos. Chem., 18(1), 75–102, https://doi.org/10.1007/BF00694375, 1994.

Hatch, L. E., Jen, C. N., Kreisberg, N. M., Selimovic, V., Yokelson, R. J., Stamatis, C., York, R. A., Foster, D., Stephens, S. L., Goldstein, A. H., and Barsanti, K. C.: Highly speciated measurements of terpenoids emitted from laboratory and mixed-conifer forest prescribed fires, Environ. Sci. Tech., 53(16), 9418–9428, https://doi.org/10.1021/acs.est.9b02612, 2019.

Hatch, L. E., Luo, W., Pankow, J. F., Yokelson, R. J., Stockwell, C. E., and Barsanti, K. C.: Identification and quantification of gaseous organic compounds emitted from biomass burning using two-dimensional gas chromatography-time-of-flight mass spectrometry, Atmos. Chem. Phys., 15(4), 1865–1899, https://doi.org/10.5194/acp-15-1865-2015, 2015.

Hayward, S., Muncey, R. J., James, A. E., Halsall, C. J., and Hewitt, C. N.: Monoterpene emissions from soil in a Sitka spruce forest, Atmos. Environ., 35(24), 4081–4087, https://doi.org/10.1016/S1352-2310(01)00213-8, 2001.

Jacobson, M. C., Hansson, H. C., Noone, K. J., and Charlson, R. J.: Organic atmospheric aerosols: Review and state of the science, Rev. Geophys., 38(2), 267–294, https://doi.org/10.1029/1998RG000045, 2000.

Jimenez, J. L., Canagaratna, M. R., Donahue, N. M., Prevot, A. S. H., Zhang, Q., Kroll, J. H., DeCarlo, P. F., Allan, J. D., Coe, H., Ng, N. L., Aiken, A. C., Docherty, K. S., Ulbrich, I. M., Grieshop, A. P., Robinson, A. L., Duplissy, J., Smith, J. D., Wilson, K. R., Lanz, V. A., … Worsnop, D. R. (2009). Evolution of organic aerosols in the atmosphere. *Science*, *326*(5959), 1525–1529. https://doi.org/10.1126/science.1180353

Kanakidou, M., Seinfeld, J. H., Pandis, S. N., Barnes, I., Dentener, F. J., Facchini, M. C., van Dingenen, R., Ervens, B., Nenes, A., Nielsen, C. J., Swietlicki, E., Putaud, J. P., Balkanski, Y., Fuzzi, S., Horth, J., Moortgat, G. K., Winterhalter, R., Myhre, C. E. L., Tsigaridis, K., Vignati, E., Stephanou, E. G., and Wilson, J.: Organic aerosol and global

climate modelling: A review, Atmos. Chem. Phys. Discuss., 4(5), 5855–6024, https://doi.org/10.5194/acpd-4-5855-2004, 2004.

Ludley, Katherine. E., Jickells, S. M., Chamberlain, P. M., Whitaker, J., and Robinson, C. H.: Distribution of monoterpenes between organic resources in upper soil horizons under monocultures of Picea abies, Picea sitchensis and Pinus Sylvestris, Soil Biol. Biochem., 41(6), 1050–1059, https://doi.org/10.1016/J.SOILBIO.2009.02.002, 2009.

Maleknia, S. D., Bell, T. L., and Adams, M. A.: PTR-MS analysis of reference and plant-emitted volatile organic compounds, Int. J. Mass Spectrom., 262(3), 203–210, https://doi.org/10.1016/j.ijms.2006.11.010, 2007.

Ng, N. L., Chhabra, P. S., Chan, A. W. H., Surratt, J. D., Kroll, J. H., Kwan, A. J., McCabe, D. C., Wennberg, P. O., Sorooshian, A., Murphy, S. M., Dalleska, N. F., Flagan, R. C., and Seinfeld, J. H.: Effect of NO_x level on secondary organic aerosol (SOA) formation from the photooxidation of terpenes, Atmos. Chem. Phys., 7(19), 5159–5174, https://doi.org/10.5194/acp-7-5159-2007, 2007.

Pankow, J. F.: An absorption model of the gas/aerosol partitioning involved in the formation of secondary organic aerosol, Atmos. Environ., 28(2), 189-193, https://doi.org/10.1016/1352-2310(94)90094-9, 1994.

Rinne, J., Tuovinen, J. P., Laurila, T., Hakola, H., Aurela, M., and Hypén, H.: Measurements of hydrocarbon fluxes by a gradient method above a northern boreal forest, Agr. Forest Meteorol., 102(1), 25–37, https://doi.org/10.1016/S0168-1923(00)00088-5, 2000.

Tani, A., Hayward, S., and Hewitt, C. N.: Measurement of monoterpenes and related compounds by proton transfer reaction-mass spectrometry (PTR-MS), Int. J. Mass Spectrom., 223–224, 561–578, https://doi.org/10.1016/S1387-3806(02)00880-1, 2003.

White, M. L., Russo, R. S., Zhou, Y., Mao, H., Varner, R. K., Ambrose, J., Veres, P., Wingenter, O. W., Haase, K., Stutz, J., Talbot, R., and Sive, B. C.: Volatile organic compounds in northern New England marine and continental environments during the ICARTT 2004 campaign, J. Geophys. Res. Atmos., 113(8), 1–16, https://doi.org/10.1029/2007JD009161, 2008.

Yáñez-Serrano, A. M., Nölscher, A. C., Bourtsoukidis, E., Gomes Alves, E., Ganzeveld, L., Bonn, B., Wolff, S., Sa, M., Yamasoe, M., Williams, J., Andreae, M. O., and Kesselmeier, J.: Monoterpene chemical speciation in a tropical rainforest: Variation with season, height, and time of day at the Amazon Tall Tower Observatory (ATTO), Atmos. Chem. Phys., 18(5), 3403–3418, https://doi.org/10.5194/acp-18-3403-2018, 2018.

Appendix B

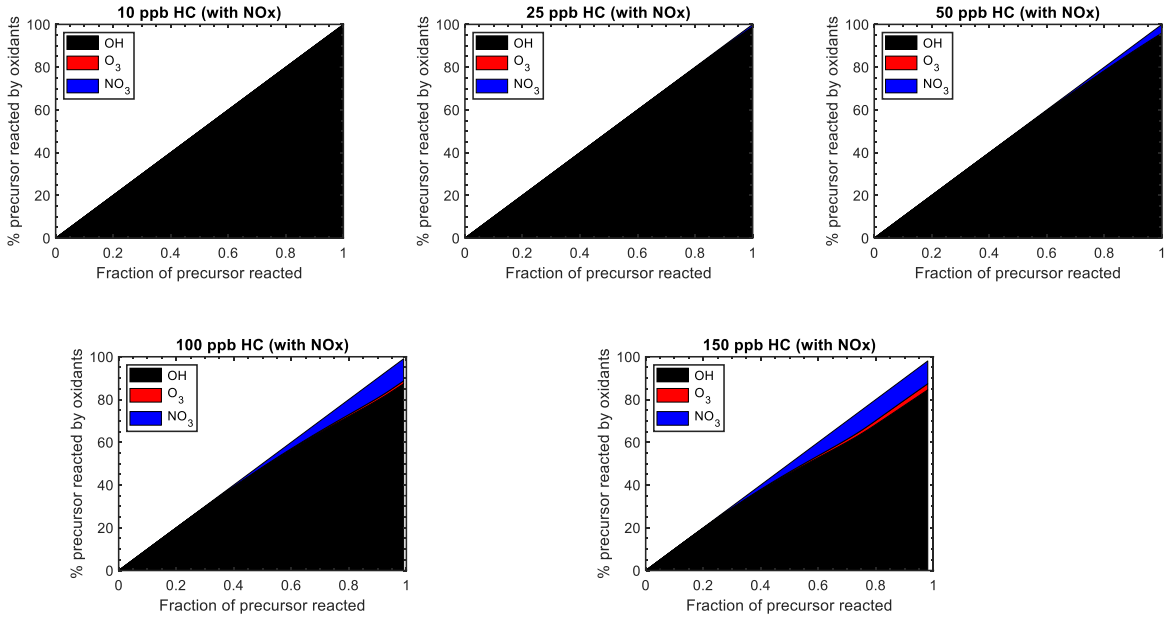

Figure B1: Percentage of precursor consumed by OH (black), O_3 (red), and NO_3 (blue) as a function of fraction of precursor reacted for camphene in the presence of initial NOx.

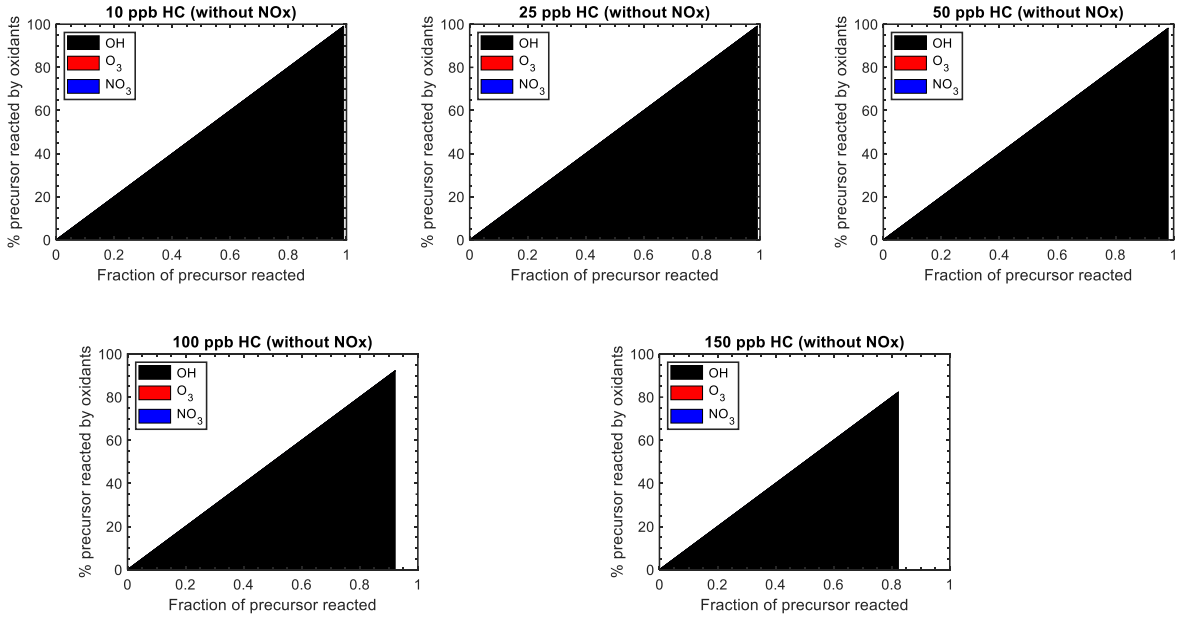

Figure B2: Percentage of precursor consumed by OH (black), O3 (red), and NO3 (blue) as a function of fraction of precursor reacted for camphene without NOx.

Chapter 4: Developing air quality model surrogates for monoterpenes using GECKO-A

4.1 Introduction

Monoterpenes emitted to the atmosphere can react with oxidants (OH, O_3, and NO_3) to form oxidation products that based on their volatility can partition to the particle-phase to form secondary organic aerosol (SOA) (Atkinson & Arey, 2003; Hakola et al., 1994; Ziemann, 2011). SOA composes a large fraction of particulate matter (PM) in the atmosphere, which adversely affects visibility and public health, and plays a role in radiative climate forcing and cloud formation (Jacobson et al., 2000; Kanakidou et al., 2004; Pöschl, 2005). Chamber studies using monoterpenes as precursors have demonstrated that the SOA formation potentials of monoterpenes are diverse and are largely influenced by their molecular structures, reactivity, and volatility of oxidation products (e.g., Griffin et al., 1999; Lee et al., 2006).

Monoterpene chemistry and SOA formation are not well represented in chemical mechanisms applied in air quality models, leading to uncertainties in predictions of SOA and PM when monoterpene emissions are significant (Pun et al., 2003). Monoterpenes are typically represented in air quality models using one to two lumped model surrogates to reduce computational cost (e.g., Carlton et al., 2010). Two lumped surrogates are not sufficient to represent the chemistry and SOA formation potential of such a structurally diverse class of compounds. Recently, Schwantes et al. (2020) updated monoterpene chemistry in the Model for Ozone and Related chemical Tracers (MOZART-T2) to improve ozone prediction by replacing the single monoterpene surrogate (MTERP) with four monoterpene surrogates: APIN for α-pinene, BPIN for β-pinene, LIMON for

limonene, and MYRC for myrcene. Individual monoterpenes were subsequently mapped to the four surrogates based on their molecular structure (Schwantes et al., 2020). While the terpene chemistry updates in MOZART-T2 greatly reduced ozone bias in CAM-chem (Community Atmospheric Model with full chemistry), better representation of SOA formation in models is required for accurate simulation of SOA.

Better representation of terpenes in models requires comprehensive understanding of SOA formation from individual monoterpenes based on laboratory, theoretical, and mechanistic studies. While chamber studies have been conducted for some monoterpenes including α-pinene and limonene (e.g., Lee et al., 2006; Presto & Donahue, 2006), a number of monoterpenes remain understudied. Where experimental data are limited, explicit models can provide mechanistic insights into SOA formation from understudied compounds. For example, Afreh et al. (2020) used a near-explicit model, GECKO-A, to study SOA formation from camphene, a ubiquitous but understudied monoterpene. They demonstrated that camphene can form approximately twice as much SOA as α-pinene. Further, Afreh et al. (2020) demonstrated the potential of representing camphene SOA as a 50/50 mixture of α-pinene and limonene in air quality models.

In this work, model surrogates were proposed for 13 monoterpenes based on GECKO-A simulations using two approaches. In the first approach, compounds were grouped using k-means clustering based on simulated SOA yields of 10 monoterpenes under controlled reactivity conditions. In the second approach, compounds were grouped using compound structure, reactivity, volatility distribution of particle-phase products, and SOA yield based on model simulations of 13 monoterpenes. The simulation conditions

were based on chamber photooxidation conditions in Lee et al. (2006). GECKO-A modeling results were compared with published SOA chamber data from Lee et al. (2006) and Griffin et al. (1999) to evaluate GECKO-A's ability to reproduce chamber observations.

4.2 Method

4.2.1 GECKO-A model description

SOA formation from 13 monoterpene precursors was modeled using GECKO-A. The GECKO-A modeling tool is described in detail by Aumont et al. (2005). GECKO-A was used to generate nearly explicit chemical mechanisms for each monoterpene using experimental data, structure-activity relationships (SARs), and a predefined protocol (Aumont et al., 2005, 2012; Camredon et al., 2007). Autoxidation was not considered in the mechanism generation. To reduce the size of the gas-phase chemical mechanisms, the following simplifications were applied during the mechanism generation: (1) the maximum generations of oxidation for each mechanism was set at six; (2) position isomers were lumped for species with production yield lower than 10^{-3} (Valorso et al., 2011); and (3) species with vapor pressure lower than 10^{-13} atm were considered to partition completely to the particle phase and therefore treated as end products (Valorso et al., 2011). Regarding the maximum generations, Aumont et al. (2012) showed that for hexadecane, the gas- and particle-phase composition and evolution did not change significantly beyond six generations. The generated mechanisms were then applied in a box model to simulate the evolution of gaseous organic compounds and SOA formation (Aumont et al., 2005, 2012; Camredon et al., 2007). The gas/particle partitioning in GECKO-A was calculated

assuming thermodynamic equilibrium between the gas and an ideal (activity coefficients = 1) condensed phase. The condensed phase was assumed homogeneous and inert (i.e., no condensed-phase reactions were considered).

4.2.2 Simulation conditions

Simulations were performed using 13 different monoterpene precursors typically measured from biogenic and pyrogenic sources: 3-carene, α-phellandrene, α-pinene, α-terpinene, β-myrcene, β-phellandrene, β-pinene, camphene, γ-terpinene, limonene, sabinene, terpinolene, and z-ocimene. To facilitate comparison between GECKO-A modeling results and published SOA chamber data, simulation conditions were based on chamber photooxidation conditions in Lee et al. (2006) and were as follows (Table 4.1): 120 ppb of hydrocarbon (HC), 100 ppb of NO, 20 ppb of NO_2, 10 ppb of HONO, and 1 μg m^{-3} of organic seed with molecular weight of 250 g mol^{-1}. In addition, temperature was fixed at 298 K, relative humidity was fixed at 50 %, and the solar zenith angle (required to compute the photolysis frequencies) was fixed at 50°.

To evaluate the ability of GECKO-A to reproduce chamber observations, modeled SOA mass concentrations and yields were compared with measured SOA mass concentrations and yields from Lee et al. (2006) and Griffin et al. (1999) for six of the 13 monoterpenes: 3-carene, α-terpinene, β-myrcene, β-pinene, limonene, and terpinolene. In addition, the simulated decay rates, gas-phase reactivity, and simulated oxidation products of the six monoterpenes were compared with measurements from Lee et al. (2006) to better understand the underlying reasons for both good measurement-model agreement and poor measurement-model agreement.

To optimize the number of groups needed to represent monoterpenes, k-means clustering algorithm was applied to simulated SOA yields of 10 monoterpenes under controlled reactivity conditions. The controlled reactivity simulations were run under relatively low NOx (10 ppb NO) and relatively high NOx (50 ppb NO) conditions. For both NOx conditions, the initial hydrocarbon mixing ratios were set at 5 levels (1, 5, 10, 20, and 50 ppb). In each simulation, 50 ppb of formaldehyde, 10 ppm of ethane, and 1 μg m^{-3} of organic seed with molecular weight of 250 g mol^{-1} were added (Table C1). Further, the 13 monoterpenes simulated under the chamber conditions were grouped based on structure, reactivity, volatility of particle-phase products, and SOA yields. These approaches resulted in 4-6 clusters for monoterpenes.

Table 4.1: **Initial conditions for GECKO-A chamber reactivity simulations.**

HC (ppb)	NO (ppb)	NO_2 (ppb)	HONO (ppb)	Organic seed (μg/m^3)	RH (%)	T (K)
120	100	20	10	1	50	298

4.3 Results

4.3.1 Comparison between model results and chamber data

4.3.1.1 SOA yield comparison

Figure 4.1 shows SOA yield as a function of SOA mass for the GECKO-A simulations (red markers) and the chamber experiments of Lee et al. (2006) and Griffin et al. (1999) (grey markers). The GECKO-A (this work) and chamber initial conditions and reacted hydrocarbon (ΔHC) mixing ratios, SOA mass, and SOA yields are summarized in Table C2. Generally, for each monoterpene, the SOA yields from Griffin et al. (1999) were

lower than from Lee et al. (2006) likely due to temperature and NOx differences in experimental conditions. Higher temperatures and higher NOx mixing ratios (lower VOC:NOx ratios) of the Griffin et al. (1999) experimental conditions are expected to result in relatively lower SOA yields since SOA yields of monoterpenes generally tend to be lower at higher temperatures and higher NO_x conditions (lower initial VOC:NO_x ratios) (Kim and Paulson, 2013; Pathak et al., 2007b). Starting with limonene photooxidation, as previously shown in Afreh et al. (2020), both measured and modeled SOA yields show a linear trend as a function of SOA mass (for SOA mass > 25 μg m^{-3}). The limonene SOA yields are the highest among the monoterpenes studied in both the chamber studies and as modelled using GECKO-A. For both limonene and β-myrcene, the predicted SOA yields are in qualitative agreement with the chamber SOA yields and are closer to the Lee et al. (2006) yields due to the similar initial conditions. For β-pinene, the measurements demonstrate a flattening of the yield curve, and the modelled yield was approximately the same as the observed yield from Lee et al. (2006) though the ΔHC was higher in the chamber experiments. For terpinolene, the SOA yields predicted by GECKO-A and reported by Lee et al. (2006) were significantly higher than reported by Griffin et al. (1999), as noted above for all monoterpenes. The scarcity of data points at the higher SOA mass loadings and yields make it difficult to assess the extent of measurement-model agreement. For α-terpinene, while there is a trend in the predicted and observed SOA yields, the predicted SOA yield was significantly higher than the Lee et al. (2006) yield, particularly given the similar initial conditions. Conversely, for 3-carene, the Lee et al. (2006) SOA yield was significantly higher than the predicted SOA yield.

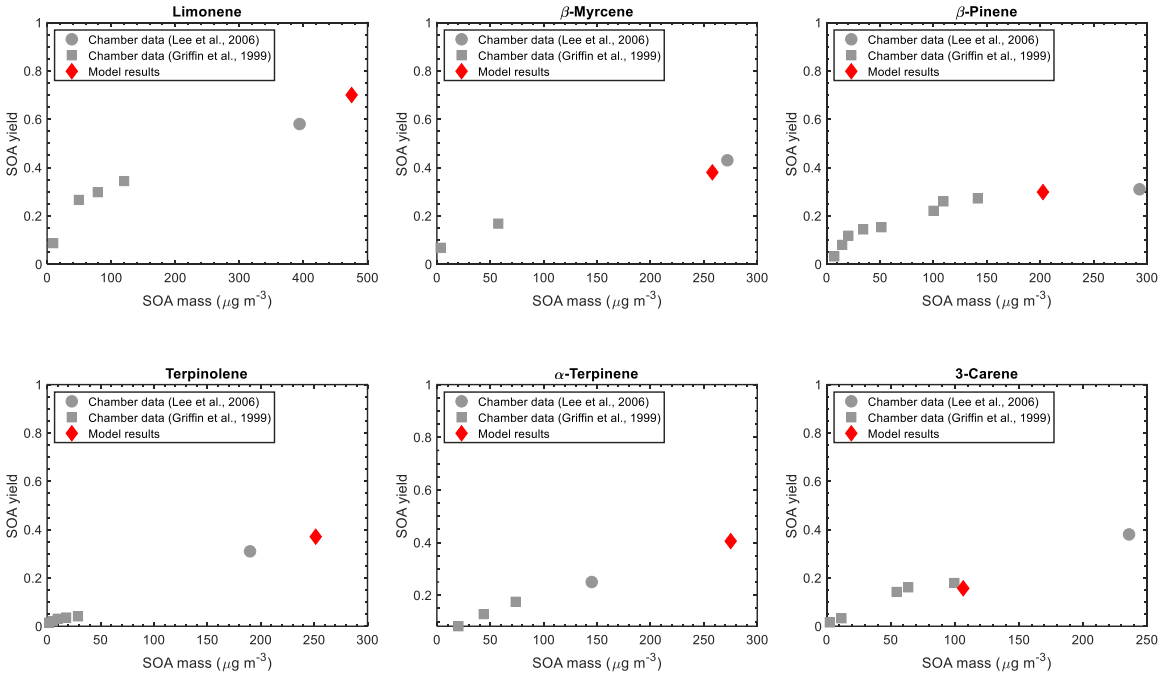

Figure 4.1: **Comparison of GECKO-A SOA yields with chamber SOA yields. GECKO-A SOA yields (diamonds), chamber SOA yields from Lee et al. (2006) are represented by circles, and Griffin et al SOA yields are represented by squares.**

4.3.1.2 Gas-phase reactivity comparison

To understand the factors influencing the similarities and differences between the model results and Lee et al. (2006) chamber data, the gas-phase predictions and observations were explored. For limonene, β-myrcene, and terpinolene, where the predicted SOA mass and yields were in good agreement with Lee et al. (2006), the time taken for the precursors to be completely consumed was slightly faster (~ 0.25 h to 0.5 h) in the simulations than observed in the Lee et al. (2006) experiments. For β-pinene, α-terpinene, and 3-carene, no precursor decay data were reported by Lee et al. (2006) to allow model-measurement comparison. For limonene, similar acetone yields were obtained from

both the simulation and the Lee et al. (2006) experiment (0.47 from the model and 0.4 from the experiment); while slightly higher yields of acetone were obtained in the model than observed in the experiment for β-myrcene (25.3 % from the model and 22 % from the experiment), β-pinene (10.9 % from the model and 7.9 % from the experiment), and terpinolene (28.4 % from the model and 20 % from the experiment).

For α-terpinene and 3-carene, the measurement-model SOA yields disagreements are likely due to differences in the gas-phase reactivity and subsequent oxidation product formation between the experiments and simulations. As shown in Figure C1, the fractional reactivity of precursor by O_3 and NO_3 reactions played a non-negligible role in the photooxidation simulations; with 94 % of α-terpinene consumed by O_3, and 16 % and 20 % of 3-carene consumed by O_3 and NO_3, respectively. While the percentages of O_3 and NO_3 reactions with the precursors were not explicitly reported for the photooxidation experiments to allow for direct measurement-model comparison, Lee et al. (2006) suggested that O_3 and NO_3 reactions played minimal roles in their experiments based on the observed major oxidation products, which were mostly influenced by OH chemistry. For α-terpinene, the higher predicted SOA yield (41 %) than reported (25 %) by Lee et al. (2006) could be as a result of the dominant reaction of α-terpinene by O_3 during the simulation (Fig. B1). The dominant reaction of α-terpinene by O_3 is influenced by α-terpinene having the lowest lifetime of 1 min for reaction with O_3 among the monoterpenes (Atkinson and Arey, 2003). This leads to rapid decay of α-terpinene, and formation of particle-phase oxidation products dominated by C7 to C10 products with 3 to 5 functional groups (Fig. 4.2). It is likely that a relatively high fraction of major products observed in

the α-terpinene experiment were not oxidized enough to partition to the particle-phase, thereby resulting in lower SOA mass. For example, the yield of α-terpinaldehyde (19 %), a major first-generation product observed by Lee et al. (2006), was approximately 3 orders of magnitude higher than simulated by the model (0.01 %), suggesting that α-terpinaldehyde could not be further oxidized during the experiment and therefore remained in the gas-phase. For 3-carene, the lower predicted SOA yield (16 %) than reported (38 %) by Lee et al. (2006) is likely due to the slow decay of 3-carene during the simulation, as well as the contribution of NO_3 chemistry to 3-carene reactivity (~ 20 %), which will lead to the formation of more organic nitrate products with relatively higher volatility. The slow reactivity of 3-carene likely resulted in high fraction of oxidation products (83 % of the carbon budget) that could not readily partitioned to the particle-phase, for example, caronaldehyde, a major C10 product remained in the gas phase with a simulated yield of 25 %. While caronaldehyde was observed experimentally by Lee et al. (2006), the gas-phase yield was not explicitly reported to allow for comparison. Similarly, Lee et al. (2006) did not report decay data or oxidant levels for 3-carene.

4.3.2 Comparison among GECKO-A simulation runs

During the photooxidation simulations, monoterpenes reacted with OH, O_3, and NO_3. The simulated fractional reactivity of monoterpenes with the atmospheric oxidations were largely influenced by their relative lifetimes with the oxidants. Rapid depletion of precursors was observed for compounds with significant reactivity with O_3 (> 25 %) due to the presence of 2 to 3 double bonds in their chemical structure, while slow depletion of precursors is observed for compounds with substantial NO_3 reactivity (> 10 %). Based on

observations by Lee et al. (2006), SOA yields are generally expected to be higher from monoterpenes with internal double bonds due to less fragmentation, resulting in loss of carbon, in the oxidation process. Exceptions to this general observation were α-terpinene and γ-terpinene, where low SOA yields were observed despite having two internal double bonds, as well as β-myrcene, an acyclic monoterpene that formed high SOA yield (Lee et al., 2006). In addition to structures, the extent of SOA formation from monoterpenes are known to be influenced by their reaction rate constants and the volatility of their oxidation products (Griffin et al., 1999; Ng et al., 2007; Zhang et al., 2015). In this section the molecular structures (Fig. C3), simulated fractional reactivity with oxidants (Fig. C1), carbon budgets (Fig. C2), and volatility distribution of final particle-phase products (Figures 4.2 and 4.3) were explored to elucidate the variability in the simulated monoterpene SOA yields. Under the photooxidation conditions, simulated SOA yields were higher for monocyclic monoterpenes with internal double bonds (e.g. limonene (0.70), β-phellandrene (0.50), α-phellandrene (0.44), α-terpinene (0.41), γ-terpinene (0.38), and terpinolene (0.37)). In contrast, simulated SOA yields (Fig. 4.4) were lower for bicyclic monoterpenes with an internal double-bonds or an external double bond (e.g., β-pinene (0.30), α-pinene (0.29), sabinene (0.16), and 3-carene (0.16)), except for camphene which had a high simulated SOA yield of 0.61, despite being a bicyclic monoterpene with one external double bond.

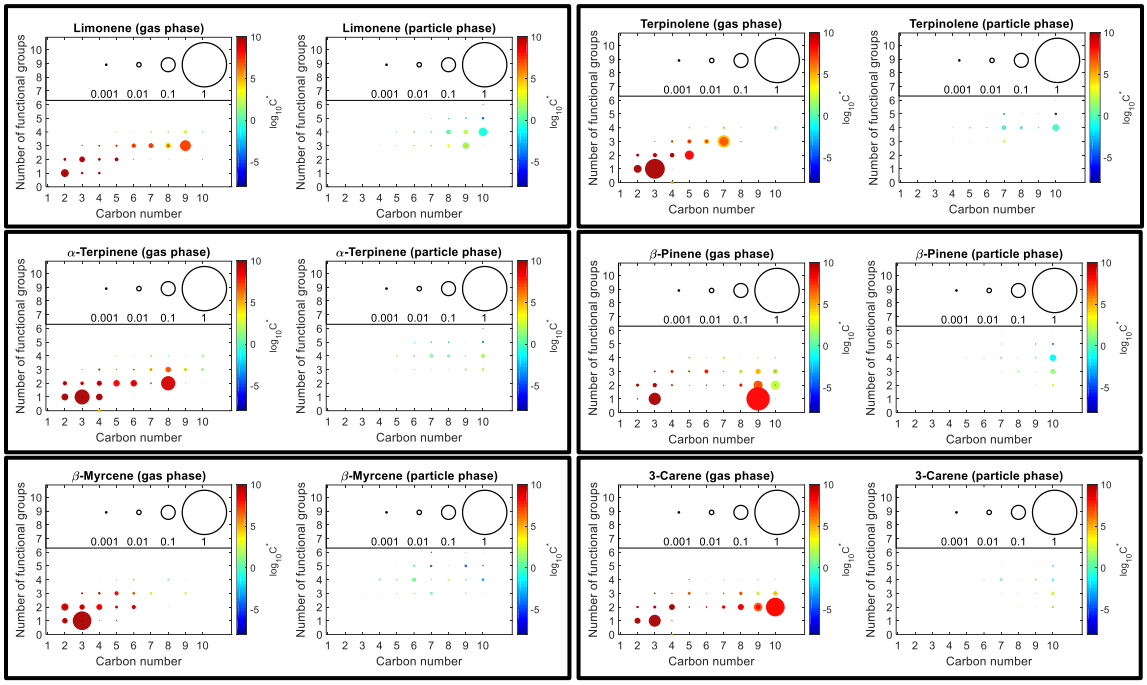

Figure 4.2: **Number of functional groups associated with gas- and particle-phase species as a function of carbon number for limonene, α-terpinene, β-myrcene, terpinolene, β-pinene, α-pinene, and 3-carene after 8 hours of photooxidation simulation.**

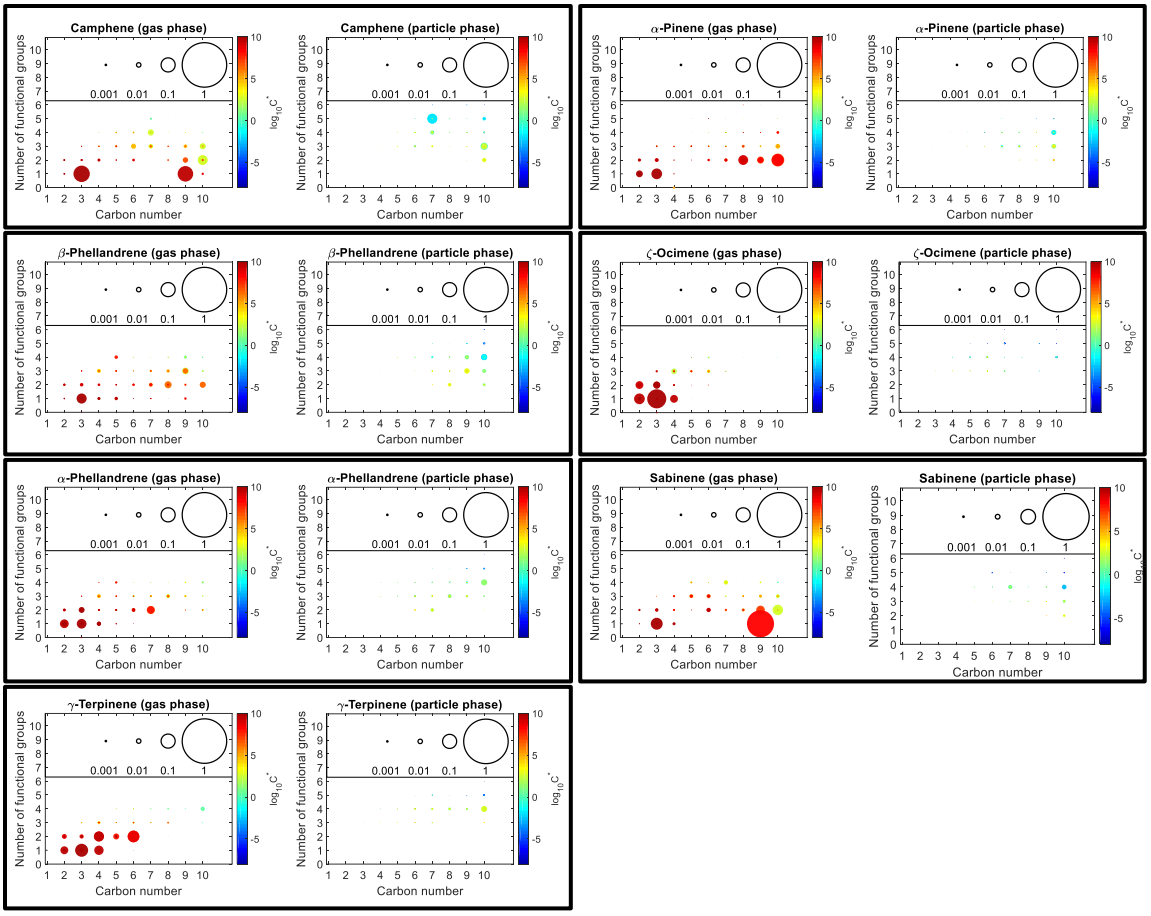

Figure 4.3: **Number of functional groups associated with gas- and particle-phase species as a function of carbon number for camphene, β-phellandrene, α-phellandrene, γ-terpinene, α-pinene, z-ocimene, and 3-carene after 8 hours of photooxidation simulation.**

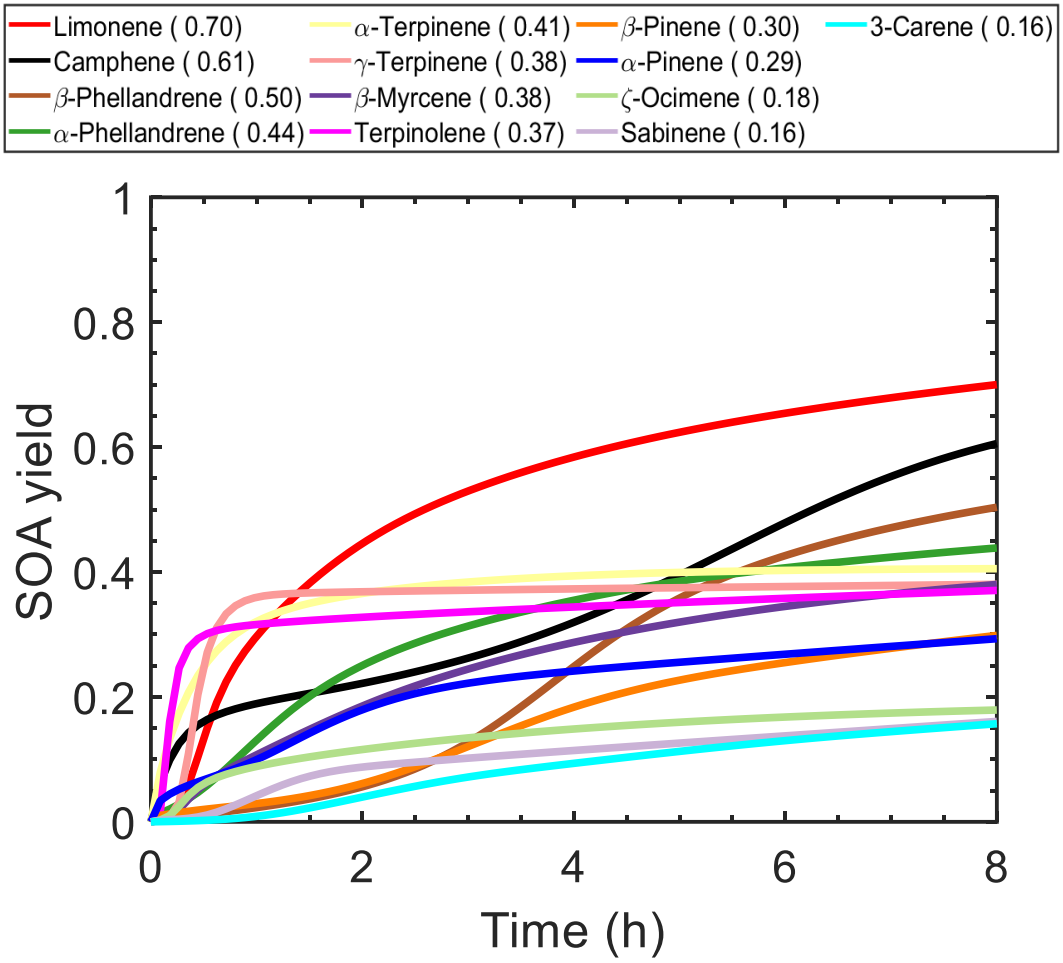

Figure 4.4: **Simulated SOA yield as a function of time for 13 monoterpenes. Inserted in the legend are the respective SOA yield values for the monoterpenes.**

4.3.2.1 Monocyclic monoterpenes

Limonene, which had the highest simulated SOA yield, was completely consumed in 1 hour of oxidation (Fig. C2), predominantly by OH (~ 72 %) and O_3 (~ 23 %) (Fig. C1). After 8 hours of oxidation, 50 % of the limonene carbon was in the gas phase, 34 % of the carbon in the particle phase, and the remaining 16 % of the carbon was CO+CO_2.

Limonene's high simulated SOA yield (0.70) is attributed to the large amounts of relatively C8 to C10 particle-phase products, with 3 to 5 functional groups (Fig. 4.2). β-Phellandrene, also monocyclic with one internal and one external double bond (Fig. C4), reacts more slowly that limonene (completely consumed after 5 hours). Both limonene and β-phellandrene continue to form SOA after the precursor is completely reacted. The overall yield of β-phellandrene is lower, 0.50, with 24% of the carbon in the particle phase; largely C9 and C10 products with 2 to 5 functional groups. While structurally similar (cyclic with two internal double bonds), α-phellandrene, α-terpinene, and γ-terpinene have different reaction rates and thus fractional reactivity. The monoterpene α-phellandrene reacts predominantly with O_3 (~ 73 %), followed by OH (~ 25 %), and NO_3 (~ 2 %); α-terpinene reacts largely with O_3 (~ 94 %), and less with OH (~ 3 %) and NO_3 (~ 3 %). γ-Terpinene, on the other hand, reacts predominantly with OH (~ 82 %), followed by O_3 (~ 11 %), and NO_3 (~ 7 %). The consumption of α-terpinene (after 5 min) was more rapid than that of α-phellandrene (after 1 hour) and of γ-terpinene (after 45 min). As with their SOA yields, the fraction of organics in the particle phase was slightly higher for α-phellandrene (22 %) than for α-terpinene (17 %) and for γ-terpinene (17 %). Terpinolene, like limonene, is monocyclic with one internal and one external double bond, and completely reacts after 15 min of oxidation, largely by OH (~ 57 %) and O_3 (~ 40 %). Terpinolene had an SOA yield of 0.37, and the particle phase was largely composed of C7 to C10 products with 4 to 5 functional groups.

4.3.2.2 Bicyclic monoterpenes

While structurally bicyclic, α-pinene has one internal double bond whereas β-pinene has one external double bond. Further, α-pinene reactivity with O_3 (~ 35 %) was substantially higher than that of β-pinene (15 %) and had faster depletion (completely consumed after 3 hours) than β-pinene (completely consumed after 5 hours) (Fig. C1). Despite the differences in their reactivity, α-pinene and β-pinene had approximately equal fractions of carbon in the particle-phase (14 %) (Fig. C2) as well as similar SOA yields (0.29 for α-pinene and 0.30 for β-pinene), with the particle phase dominated by C10 products with 2 to 5 functional groups. Sabinene, bicyclic with one external double bond, and 3-carene, bicyclic with one internal double bond, had the lowest simulated SOA yields (0.16 each). Sabinene was completely consumed after 1.5 hours, largely by OH (~ 70 %), O_3 (~ 20 %), and NO_3 (~ 10 %), while 3-carene was completely consumed after 3 hours, largely by OH (~ 65 %), O_3 (~ 15 %), and NO_3 (~ 20 %). Despite having similar carbon budget compositions (Fig. 4.2), sabinene and 3-carene formed diverse final product distributions. For example, the final gas-phase organics of sabinene were dominated by C9 products (Fig. 4.3), whereas the final gas-phase organics were dominated by C10 products (Fig 4a). Camphene, like β-pinene and sabinene, is structurally bicyclic with one external double bond. The simulated SOA yield for camphene (0.61) was approximately two times that of β-pinene (0.30) and approximately four times that of sabinene (0.16). Among the 13 monoterpenes, camphene's lifetime with O_3 was the highest (18 days), and hence reacted primarily with OH (~ 63 %) and NO_3 (~ 25 %). Also, camphene was the monoterpene with the slowest reactivity, with ~ 90 % of the precursor reacted after 8 hours

of oxidation. Nevertheless, its particle-phase carbon budget was relatively high (~ 26 %), resulting in an SOA yield that ranked second among the modeled monoterpenes. Afreh et al. (2020) attribute the significantly high SOA yield from camphene to the propensity of camphene to initially form very low volatility particle-phase products during oxidation. As shown in Fig. 4.3, the final particle-phase product distribution largely consists of C7 products with 3 to 6 functional groups and C10 products with 2 to 6 functional groups.

4.3.2.3 Acyclic monoterpenes

The monoterpenes β-myrcene and z-ocimene are both acyclic monoterpenes with three double bonds. They have similar reactivities with OH (~ 70 % for β-myrcene and ~ 73 % for z-ocimene), O_3 (~ 27 % for β-myrcene and ~ 25 % for z-ocimene), and NO_3 (~ 3 % for β-myrcene and ~ 2 % for z-ocimene) (Fig. B1), but diverse SOA yields (0.38 from β-myrcene and 0.18 from z-ocimene) due to diverse evolution of their oxidation products. As shown in Fig. 4.3, the fraction of carbon in the particle-phase is higher for β-myrcene (15 %) than for z-ocimene (7 %), while the fraction of $CO+CO_2$ is lower for β-myrcene (25 %) than for z-ocimene (30 %). This suggests that β-myrcene experienced greater functionalization during photooxidation, forming products that partitioned to the particle phase; whereas z-ocimene experienced more fragmentation, with products forming $CO+CO_2$.

4.3.3 Considering monoterpene representation in models

As demonstrated in the previous section, monoterpene chemistry is complex, and monoterpene SOA yields vary greatly, even among monoterpenes that have similar

molecular structures. Hence, it is important that the chemistry and diversity of SOA formation potentials of monoterpenes are adequately represented in chemical mechanisms applied in air quality models to improve SOA predictions. Discussed in this section are some approaches that were tested to develop simplified but improved representation of gas-phase monoterpene chemistry and subsequent SOA formation for air quality modeling. In one approach, GECKO-A "controlled reactivity" simulations were performed for 10 monoterpenes under two NOx conditions (10 ppb NO and 50 ppb NO) and varying initial hydrocarbon mixing ratios (Table B2 and B3). Cluster analysis (k-means) was applied to group monoterpenes based on SOA yield and optimize the number of monoterpenes that could represent all ten monoterpenes. Using this approach resulted in different groups for the low NOx and high NOx simulation sets (Table B2 and B3), which is not ideal. Therefore, a second approach was explored to propose new groups by categorizing monoterpenes based on their molecular structure, gas-phase reactivity, amount of LVOC and ELVOC products formed, and SOA yield.

The new approach was applied to the 13 monoterpenes simulated based on the Lee et al. (2006) chamber conditions. First, the molecular structures of the monoterpenes were categorized as monocyclic, acyclic, or bicyclic (Table 4.3). Second, the percentage of precursor reactivity with oxidants were categorized as: (1) OH dominant (if precursor reactivity with OH > 70 %); (2) O_3 dominant (if precursor reactivity with O_3 > 70 %); and (3) NO_3 substantial (if precursor reactivity with $NO_3 \geq 10$ %). Third, the SOA yields were categorized into three sets based on the difference between the highest simulated SOA yield (0.7) and the lowest simulated SOA yield (0.16); the three sets were: (1) low yield

(L_{Yield}) (if SOA yield ≤ 0.3), (2) medium yield (M_{Yield}) (if 0.3 < SOA yield ≤ 0.5), and (3) high yield (H_{Yield}) (if SOA yield > 0.5). Similarly, the predicted mass of LVOCs and ELVOCs for each monoterpene were summed and, based on the difference between the highest value (~ 90 μg m^{-3}) and the lowest value (~ 4 μg m^{-3}), categorized as: (1) low LVOC (L_{LVOC}) (if LVOC+EVOC ≤ 30 μg m^{-3}); (2) medium LVOC (M_{LVOC}) (if 30 μg m^{-3} < LVOC+EVOC ≤ 60 μg m^{-3}); and (3) high LVOC (H_{LVOC}) (if LVOC+EVOC > 60 μg m^{-3}). Based on this approach, four groups were proposed for monoterpenes (Tables 4.3 and 4.4). The time dependent SOA yields of compounds in each monoterpene group is shown in Fig. 4.5.

Group 1 consists of only limonene, a monocyclic monoterpene with dominant OH reactivity, high SOA yield, and high mass of LVOCs. Group 2 consists of six monoterpenes with medium SOA yields: β-phellandrene, α-phellandrene, α-terpinene, γ-terpinene, terpinolene, and β-myrcene. Besides β-myrcene which is acyclic, the remaining five monoterpenes in group 2 are monocyclic. Also, except for terpinolene which formed medium mass of LVOCs, the remaining Group 2 monoterpenes formed high mass of LVOCs. Group 3 consists of five monoterpenes which had low SOA yields: z-ocminene, β-pinene, α-pinene, sabinene, and 3-carene. Apart from z-ocimene which was acyclic with medium mass of LVOCs, the remaining Group 3 monoterpenes were bicyclic with substantial reactivity with NO_3 and formed low mass of LVOCs. Group 4 consists of only camphene, a bicyclic monoterpene with substantial NO_3 reactivity, high SOA yield, and low mass of LVOCs.

Steps to implement the proposed monoterpene groups in air quality models will include optimizing the groups and finding the best way to represent the categorized compounds in models. One way is to represent each group by one monoterpene surrogate. For group 2, the surrogate should best represent the diversity in the gas-phase reactivity and volatility of the individual monoterpenes. Another way is to represent each group by linear combinations of well-studied monoterpenes, for which SOA parameterizations are widely available. One example is the α-pinene/limonene mixture demonstrated for camphene in Chapter 2 (Fig. 2.12).

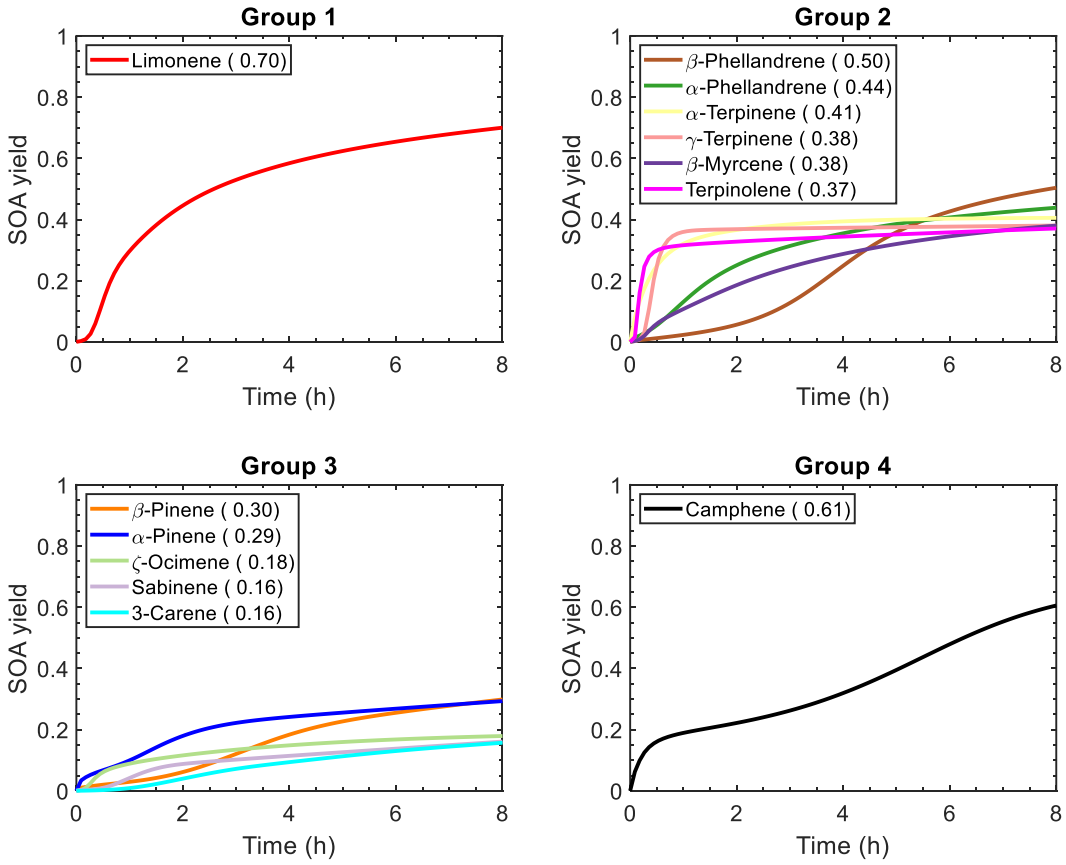

Figure 4.5: **Simulated SOA yield as a function of time for compounds in each monoterpene group. Inserted in the legend are the respective SOA yield values for the monoterpenes.**

Table 4.2: **Monoterpenes categorized into groups based on molecular structure, reactivity of precursor with oxidants, SOA yield, and mass of LVOCs using photooxidation simulation results.**

Structure	Monoterpene	OH dominant	O_3 dominant	NO_3 substantial	Group
Monocyclic	Limonene	H_{Yield} / H_{LVOC}			1
	β-Phellandrene			M_{Yield} / H_{LVOC}	2
	α-Phellandrene		M_{Yield} / H_{LVOC}		2
	α-Terpinene		M_{Yield} / H_{LVOC}		2
	γ-Terpinene	M_{Yield} / H_{LVOC}			2
	Terpinolene	M_{Yield} / M_{LVOC}			2
Acyclic	β-Myrcene	M_{Yield} / H_{LVOC}			2
	z-Ocimene	L_{Yield} / M_{LVOC}			3
Bicyclic	β-Pinene			L_{yield} / L_{LVOC}	3
	α-Pinene			L_{yield} / L_{LVOC}	3
	Sabinene			L_{yield} / L_{LVOC}	3
	3-Carene			L_{yield} / L_{LVOC}	3
	Camphene			H_{Yield} / L_{LVOC}	4

Table 4.3: **Summary of proposed monoterpene groups.**

Group 1	Group 2	Group 3	Group 4
Limonene	β-Phellandrene	z-Ocimene	Camphene
	α-Phellandrene	β-Pinene	
	α-Terpinene	α-Pinene	
	γ-Terpinene	Sabinene	
	Terpinolene	3-Carene	
	β-Myrcene		

4.4 Conclusions

Effects of molecular structures on gas-phase reactivity, gas- and particle-phase product formation, and SOA formation were studied. Under the photooxidation conditions, simulated SOA yields were higher for monocyclic monoterpenes with internal double bonds (e.g. limonene (0.70), β-phellandrene (0.50), α-phellandrene (0.44), α-terpinene (0.41), γ-terpinene (0.38), and terpinolene (0.37)) than for bicyclic monoterpenes with an internal double-bond or an external double bond (e.g., β-pinene (0.30), α-pinene (0.29), sabinene (0.16), and 3-carene (0.16)). An exception is camphene, a bicyclic monoterpene with one external double bond, which had significantly high simulated SOA yield of 0.61. To better represent monoterpene chemistry in chemical mechanisms and improved SOA parameterizations, four monoterpene groups were proposed based on molecular structure, gas-phase reactivity, mass of LVOC and ELVOC products formed, and SOA yield. Additional steps were suggested for the implementation of the monoterpene groups in models.

References

Afreh, I. K., Aumont, B., Camredon, M., & Barsanti, K. C. (2020). Using GECKO-A to derive mechanistic understanding of SOA formation from the ubiquitous but understudied camphene. Atmospheric Chemistry and Physics Discussion, September, 1–27. https://doi.org/10.5194/acp-2020-829

Atkinson, R., & Arey, J. (2003). Gas-phase tropospheric chemistry of biogenic volatile organic compounds: a review. Atmospheric Environment, 37(2), 197–219. https://doi.org/10.1016/S1352-2310(03)00391-1

Aumont, B., Szopa, S., & Madronich, S. (2005). Modelling the evolution of organic carbon during its gas-phase tropospheric oxidation: development of an explicit model based on a self generating approach. Atmospheric Chemistry and Physics Discussions, 5(1), 703–754. https://doi.org/10.5194/acpd-5-703-2005

Aumont, B., Valorso, R., Mouchel-Vallon, C., Camredon, M., Lee-Taylor, J., & Madronich, S. (2012). Modeling SOA formation from the oxidation of intermediate volatility n-alkanes. Atmospheric Chemistry and Physics, 12(16), 7577–7589. https://doi.org/10.5194/acp-12-7577-2012

Betty K. Pun, Shiang-Yuh Wu, Christian Seigneur, John H. Seinfeld, Robert J. Griffin, & Pandis, S. N. (2003). Uncertainties in Modeling Secondary Organic Aerosols: Three-Dimensional Modeling Studies in Nashville/Western Tennessee. 37(16), 3647–3661. https://doi.org/10.1021/ES0341541

Camredon, M., Aumont, B., Lee-Taylor, J., & Madronich, S. (2007). The SOA/VOC/NOx system: An explicit model of secondary organic aerosol formation. Atmospheric Chemistry and Physics, 7(21), 5599–5610. https://doi.org/10.5194/acp-7-5599-2007

Carlton, A. G., Bhave, P. v., Napelenok, S. L., Edney, E. O., Sarwar, G., Pinder, R. W., Pouliot, G. A., & Houyoux, M. (2010). Model Representation of Secondary Organic Aerosol in CMAQv4.7. Environmental Science & Technology, 44(22), 8553–8560. https://doi.org/10.1021/es100636q

Griffin, R. J., Cocker, D. R., Flagan, R. C., & Seinfeld, J. H. (1999). Organic aerosol formation from the oxidation of biogenic hydrocarbons. Journal of Geophysical Research Atmospheres, 104(D3), 3555–3567. https://doi.org/10.1029/1998JD100049

Hakola, H., Arey, J., Aschmann, S. M., & Atkinson, R. (1994). Product formation from the gas-phase reactions of OH radicals and O3 with a series of monoterpenes. Journal of Atmospheric Chemistry, 18(1), 75–102. https://doi.org/10.1007/BF00694375

Jacobson, M. C., Hansson, H. C., Noone, K. J., & Charlson, R. J. (2000). Organic atmospheric aerosols: Review and state of the science. Reviews of Geophysics, 38(2), 267–294. https://doi.org/10.1029/1998RG000045

Kanakidou, M., Seinfeld, J. H., Pandis, S. N., Barnes, I., Dentener, F. J., Facchini, M. C., van Dingenen, R., Ervens, B., Nenes, A., Nielsen, C. J., Swietlicki, E., Putaud, J. P., Balkanski, Y., Fuzzi, S., Horth, J., Moortgat, G. K., Winterhalter, R., Myhre, C. E. L., Tsigaridis, K., … Wilson, J. (2004). Organic aerosol and global climate modelling: a review. Atmospheric Chemistry and Physics Discussions, 4(5), 5855–6024. https://doi.org/10.5194/acpd-4-5855-2004

Lee, A., Goldstein, A. H., Kroll, J. H., Ng, N. L., Varutbangkul, V., Flagan, R. C., & Seinfeld, J. H. (2006). Gas-phase products and secondary aerosol yields from the photooxidation of 16 different terpenes. Journal of Geophysical Research Atmospheres, 111, D17305. https://doi.org/10.1029/2006JD007050

Nannoolal, Y., Rarey, J., & Ramjugernath, D. (2008). Estimation of pure component properties part 3. Estimation of the vapor pressure of non-electrolyte organic compounds via group contribution and group interactions. Fluid Phase Equilibria, 269(1–2), 117–133. https://doi.org/10.1016/j.fluid.2008.04.020

Ng, N. L., Chhabra, P. S., Chan, A. W. H., Surratt, J. D., Kroll, J. H., Kwan, A. J., McCabe, D. C., Wennberg, P. O., Sorooshian, A., Murphy, S. M., Dalleska, N. F., Flagan, R. C., & Seinfeld, J. H. (2007). Effect of NOx level on secondary organic aerosol (SOA) formation from the photooxidation of terpenes. Atmospheric Chemistry and Physics, 7(19), 5159–5174. https://doi.org/10.5194/acp-7-5159-2007

Pöschl, U. (2005). Atmospheric Aerosols: Composition, Transformation, Climate and Health Effects. Angewandte Chemie International Edition, 44(46), 7520–7540. https://doi.org/10.1002/anie.200501122

Presto, A. A., & Donahue, N. M. (2006). Investigation of α-pinene + ozone secondary organic aerosol formation at low total aerosol mass. Environmental Science and Technology, 40(11), 3536–3543. https://doi.org/10.1021/es052203z

Schwantes, R. H., Emmons, L. K., Orlando, J. J., Barth, M. C., Tyndall, G. S., Hall, S. R., Ullmann, K., St Clair, J. M., Blake, D. R., Wisthaler, A., & Paul Bui, T. v. (2020). Comprehensive isoprene and terpene gas-phase chemistry improves simulated surface ozone in the southeastern US. Atmos. Chem. Phys, 20, 3739–3776. https://doi.org/10.5194/acp-20-3739-2020

Valorso, R., Aumont, B., Camredon, M., Raventos-Duran, T., Mouchel-Vallon, C., Ng, N. L., Seinfeld, J. H., Lee-Taylor, J., & Madronich, S. (2011). Explicit modelling of SOA formation from α-pinene photooxidation: Sensitivity to vapour pressure estimation.

Atmospheric Chemistry and Physics, 11(14), 6895–6910. https://doi.org/10.5194/acp-11-6895-2011

Zhang, X., Mcvay, R. C., Huang, D. D., Dalleska, N. F., Aumont, B., Flagan, R. C., & Seinfeld, J. H. (2015). Formation and evolution of molecular products in α-pinene secondary organic aerosol. Proceedings of the National Academy of Sciences of the United States of America, 112(46), 14168–14173. https://doi.org/10.1073/pnas.1517742112

Ziemann, P. J. (2011). Effects of molecular structure on the chemistry of aerosol formation from the OH-radical-initiated oxidation of alkanes and alkenes. International Reviews in Physical Chemistry, 30(2), 161–195. https://doi.org/10.1080/0144235X.2010.550728

Appendix C

Table C1: Initial conditions for GECKO-A controlled reactivity simulations.

HC (ppb)	NO (ppb)	C_2H_6 (ppm)	CH_2O (ppb)	Organic seed ($\mu g\ m^{-3}$)
1, 5, 10, 20, 50	10, 50	10	50	1

Table C2: Initial conditions and SOA results from this work compared with photooxidation chamber data from Lee et al. (2006) and Griffin et al. (1999).

Precursor	*T* (K)	RH (%)	$[VOC]_0$/ $[NOx]_0$ (ppbC/ppb)	ΔHC (ppb)	ΔM_o ($\mu g\ m^{-3}$)	SOA yield
GECKO-A model results (this work)						
Limonene	298	50	10	120	475.2	0.70
α-Terpinene	298	50	10	120	275.1	0.41
β-Myrcene	298	50	10	120	258.0	0.38
Terpinolene	298	50	10	120	251.5	0.37
β-Pinene	298	50	10	120	202.6	0.30
3-Carene	298	50	10	120	106.6	0.16
Chamber data (Lee et al. (2006))						
Limonene	294	45	11.0	120	394	0.58
β-Myrcene	294	53	9.0	112	272	0.43
3-Carene	294	52	8.0	109	236	0.38
Terpinolene	294	50	11.0	110	190	0.31
β-Pinene	293	50	21.0	170	293	0.31
α-Terpinene	293	47	9	103	145	0.25
Chamber data (Griffin et al. (1999))						
Limonene	309.4-313.4	5	2-4.6	20.6-65.1	9.5-120.2	0.087-0.344
3-Carene	308.8-312.8	5	3.6-6.5	28.8-104.6	2.5-99.7	0.033-0.179
α-Terpinene	313.3-316	5	3.0-5.0	47-79.6	20.2-73.8	0.082-0.175
β-Myrcene	311.1-311.9	5	2.2-3.9	9.8-77.5	3.5-57.5	0.068-0.168
β-Pinene	308.8-316.2	5	2.4-7.1	32.3-96.5	7.2-141.6	0.080-0.272
Terpinolene	312.4-316	5	2.6-5.4	25-133.2	1.9-28.9	0.015-0.041

Table C3: Monoterpenes categorized into 6 groups based on the k-means clustering method for controlled reactivity simulations under relatively low NOx condition (10 ppb NO).

		Max SOA (μgm^{-3})				
NOx Level		NO = 10 ppb				
Precursor Initial Conc. (ppb)	**Group**	1	5	10	20	50
Limonene	**1**	2.16	14.78	35.49	86.70	269.71
γ-Terpinene	**2**	1.14	7.80	19.20	48.06	164.58
Terpinolene	**2**	0.63	4.71	13.75	42.61	154.93
β-Myrcene	**3**	0.96	6.51	16.68	44.17	147.25
α-Phellandrene	**3**	1.20	7.71	17.96	42.51	136.28
α-Terpinene	**3**	0.88	6.00	14.86	37.38	125.87
α-Pinene	**4**	0.83	5.46	12.83	31.17	107.70
z-Ocimene	**4**	0.60	3.90	9.77	25.37	96.97
Camphene	**5**	1.60	10.17	22.39	46.41	96.82
3-Carene	**6**	0.57	3.79	8.99	21.98	81.77

Table C4: Monoterpenes categorized into 6 groups based on the k-means clustering method for controlled reactivity simulations under relatively high NOx condition (50 ppb NO).

		Max SOA (μgm^{-3})				
NOx Level		NO = 50 ppb				
Precursor Initial Conc. (ppb)	**Group**	1	5	10	20	50
Limonene	**1**	1.24	9.11	22.31	55.78	201.38
Camphene	**2**	1.11	8.16	20.57	50.67	163.57
α-Phellandrene	**3**	0.77	5.20	12.88	32.43	109.58
γ-Terpinene	**4**	0.64	4.69	11.56	27.75	101.19
α-Pinene	**4**	0.59	4.14	10.63	28.22	96.34
α-Terpinene	**4**	0.60	4.03	9.90	25.18	95.44
β-Myrcene	**5**	0.46	2.83	6.98	19.70	97.46
Terpinolene	**5**	0.36	2.54	6.61	18.00	89.64
3-Carene	**6**	0.39	2.64	6.68	17.55	61.07
z-Ocimene	**6**	0.28	1.69	4.03	10.62	49.93

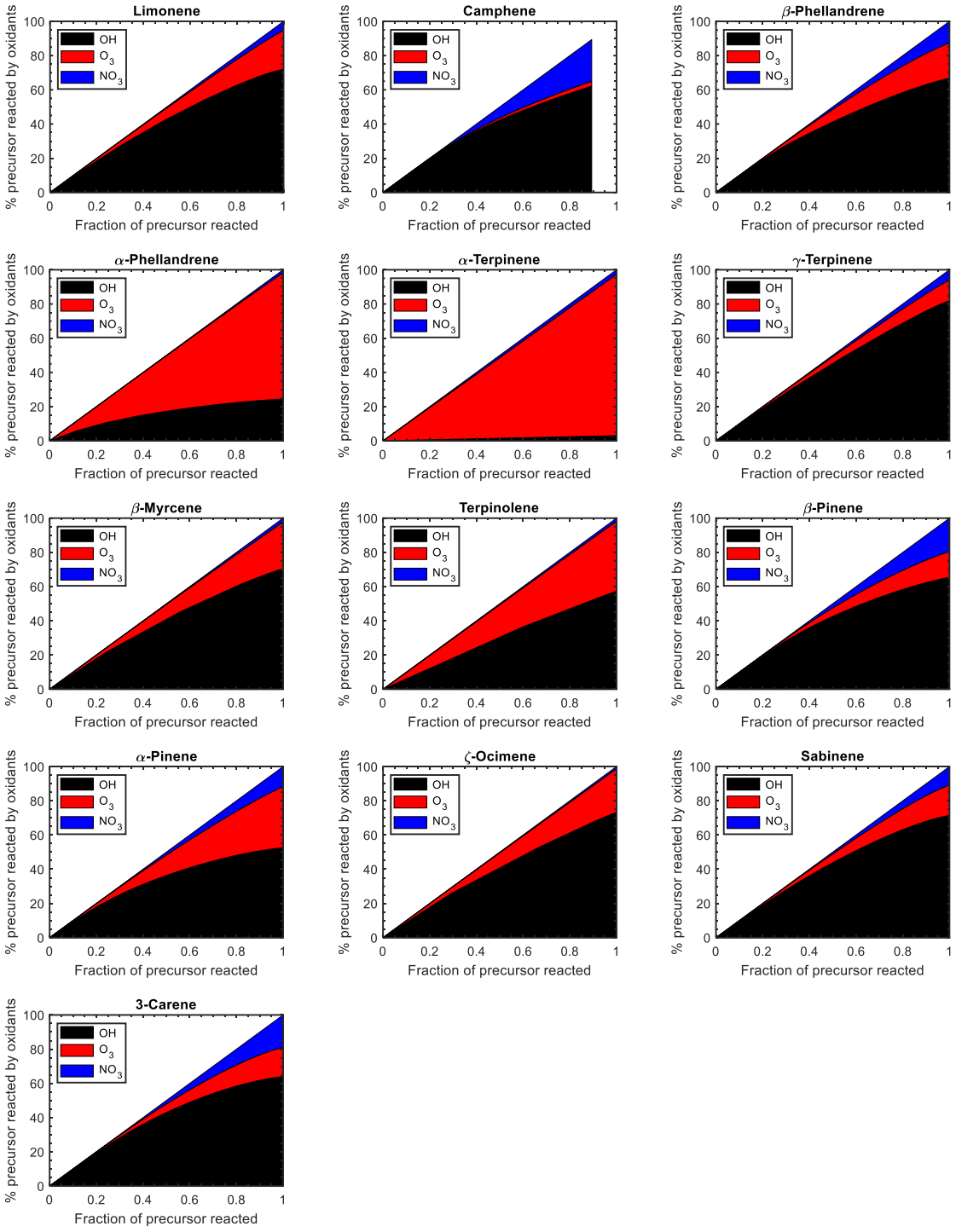

Figure C1: Percentage of precursor consumed by OH (black), O3 (red), and NO3 (blue) as a function of fraction of precursor reacted for limonene, camphene, β-phellandrene, α-phellandrene, α-terpinene, γ-terpinene, β-myrcene, terpinolene, β-pinene, α-pinene, z-ocimene, sabinene, and 3-carene.

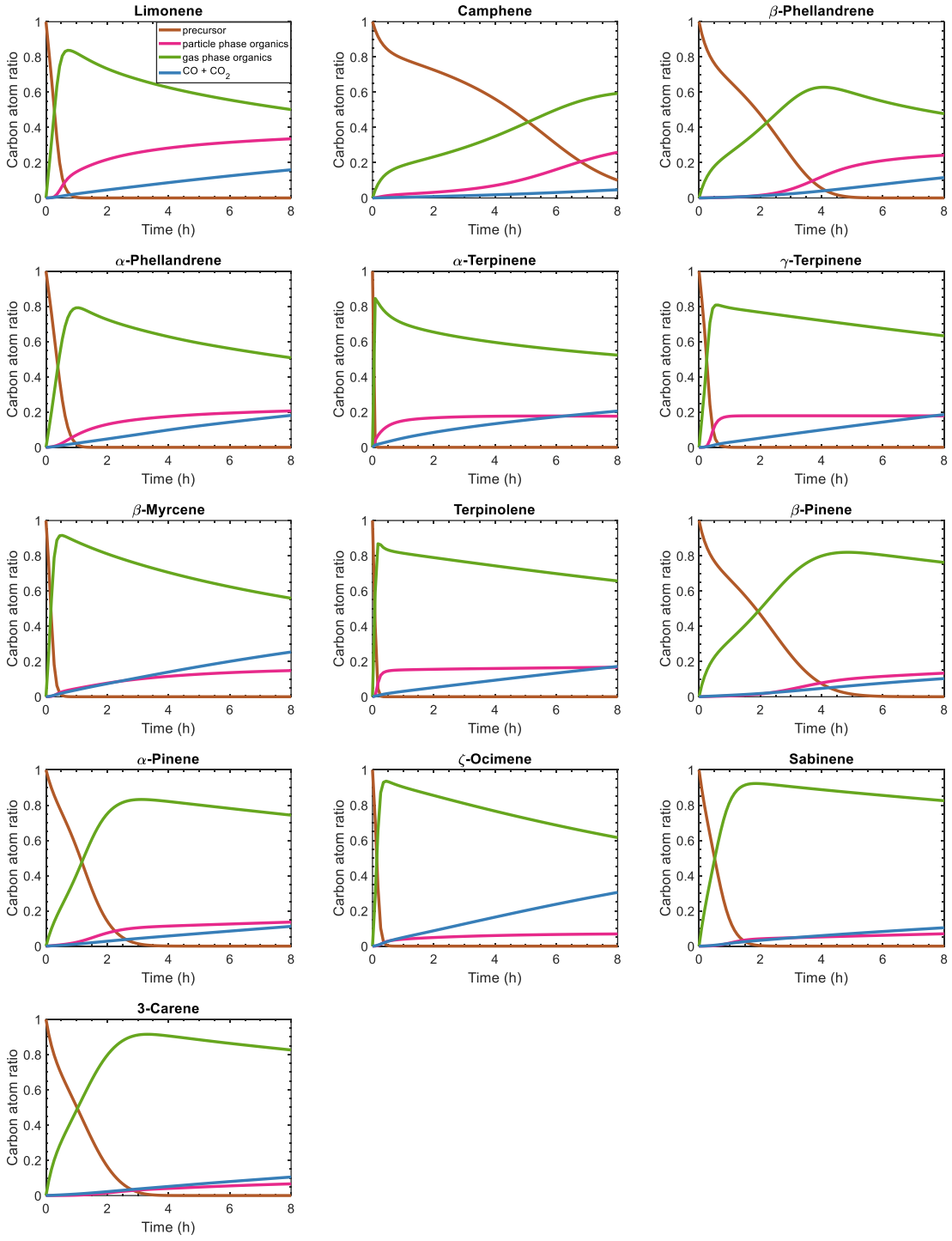

Figure C2: Carbon budget as a function of time during photooxidation simulation for limonene, camphene, β- phellandrene, α-phellandrene, α-terpinene, γ-terpinene, β-myrcene, terpinolene, β-pinene, α-pinene, z-ocimene, sabinene, and 3-carene.

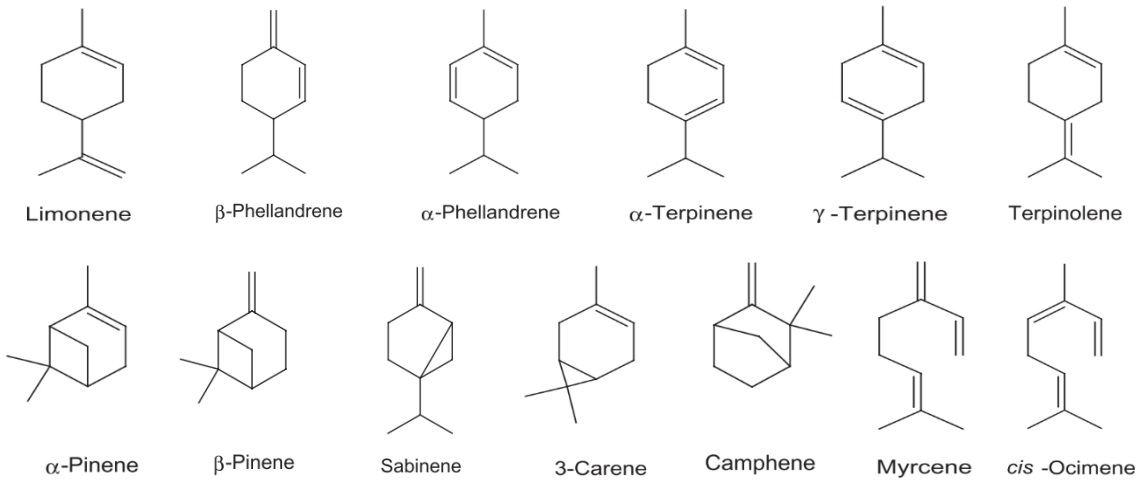

Figure C3: Structures of the monoterpenes studied (Atkinson and Arey, 2003).

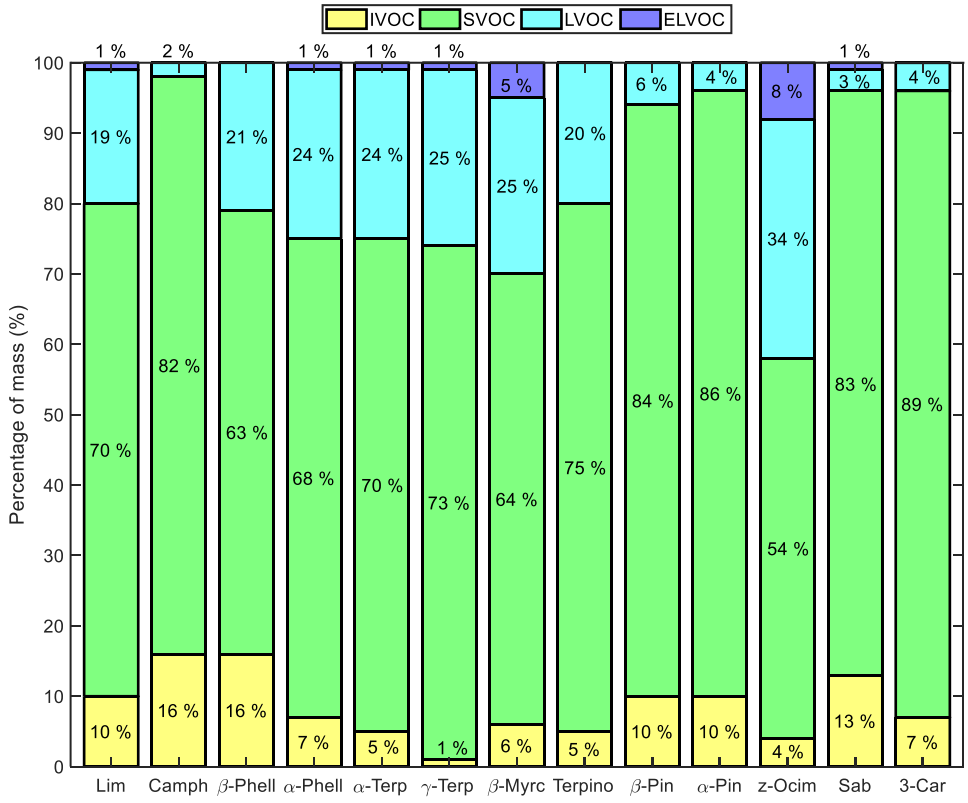

Figure C4: Mass percentage of four volatility categories in the particle phase at the end of the photooxidation simulation.

Chapter 5: Conclusions & Future Work

Overall, this dissertation has provided mechanistic understanding of SOA formation from monoterpenes, particularly those understudied in chamber, using the nearly explicit model, GECKO-A. The ability of GECKO-A to capture chamber observations were evaluated. For the first time, SOA from camphene was modeled and the results compared with camphene chamber data. Five monoterpene groups were proposed to improving representation of monoterpene chemistry in chemical mechanisms.

In this thesis, a detailed study on camphene was conducted using GECKO-A. Camphene SOA formation potential under controlled reactivity conditions was compared with that of α-pinene and limonene. Camphene was observed to form relatively lower volatility products than α-pinene and limonene during the initial oxidation period. SOA yield for camphene (46 %) was relatively high, in between α-pinene (25 %) and limonene (74 %), suggesting that SOA formation from camphene can be represented as a 50/50 mixture of α-pinene and limonene. Representing camphene as 50/50 mixture of α-pinene + limonene greatly increased predicted SOA mass by 43-50 % for black spruce and by 56-108 % for Douglas fir.

Further, the mechanistic study of SOA formation prompted a laboratory chamber study of camphene, and comparison between the model predictions and measurement data were performed. The model-measurement comparison showed that SOA yield trends were similar between the SOA model simulations and the chamber studies when NOx were present. Also, the mixing ratios of OH, ozone, and camphene decay generated by the model were consistent with the chamber data when NOx was present. In the absence of NOx, the

GECKO-A SOA results disagreed with the chamber SOA data due to limitations in GECKO-A under very low NOx conditions. For simulations with NOx, the particle phase is dominated by C7 and C10 products, whereas for simulations without NOx the particle phase is dominated largely by C10 products. Further, the top 5 particle-phase products formed from the simulations with NOx suggest that the SOA formation was driven by RO_2+NO pathway, whereas the top 5 particle-phase products from the simulations without NOx suggest that the SOA formation was driven by RO_2+HO_2 pathway.

Finally, SOA formation from 13 monoterpenes were explored under relevant chamber photooxidation conditions. Model-measurement comparison for six monoterpenes showed agreement, except for α-terpinene and 3-carene. Rapid precursor depletion was observed for monoterpenes with substantial reactivity with O3 (> 25 %), while slow precursor depletion was observed for monoterpenes with substantial NO_3 reactivity (> 13 %). It was demonstrated that monocyclic monoterpenes generally had relatively higher SOA yields than bicyclic monoterpenes, except for camphene, which had high simulated SOA yield despite being a bicyclic monoterpene. Five monoterpene groups were proposed to better represent monoterpene chemistry in chemical mechanisms and improved SOA parameterizations in models. The four monoterpene groups were derived based on molecular structure, gas-phase reactivity, mass of LVOC and ELVOC products formed, and SOA yield of individual monoterpene.

This dissertation provides an opportunity for more chamber studies on under-studied monoterpenes to help resolve model-measurement disagreements. Future updates are recommended for GECKO-A to improve simulations under zero NOx conditions.

Future studies should build on the proposed monoterpene groups by optimizing the groups and finding the best way of deriving model surrogates and SOA parameterization for each group. The approach used to propose the monoterpene groups can be applied to other classes of VOCs to help improve air quality predictions.